15185 NATIONAL LIBRARY
OTTAWA

CANADA

BIBLIOTHÈQUE NATIONALE
OTTAWA

NAME OF AUTHOR.....KAMAL ZAKI BOTROS

TITLE OF THESIS..SOME EFFECTS OF SYSTEMATIC REFLECTIONS ON ELECTRON MICROSCOPE IMAGES OF STACKING FAULTS

UNIVERSITY.....Alberta.....

DEGREE FOR WHICH THESIS WAS PRESENTED.....Ph.D.....

YEAR THIS DEGREE GRANTED.....1972.....

Permission is hereby granted to THE NATIONAL LIBRARY OF CANADA to microfilm this thesis and to lend or sell copies of the film.

The author reserves other publication rights, and neither the thesis nor extensive extracts from it may be printed or otherwise reproduced without the author's written permission.

(Signed).....K. Z. Botros.

PERMANENT ADDRESS:

...physics Dept...
...U. of A.....
.....Edmonton, Alberta

DATED..April 26th....1972

NL-91 (10-68)

THE UNIVERSITY OF ALBERTA

SOME EFFECTS OF SYSTEMATIC REFLECTIONS ON ELECTRON MICROSCOPE IMAGES OF STACKING FAULTS

by

© KAMAL ZAKI BOTROS

A THESIS

SUBMITTED TO THE FACULTY OF GRADUATE STUDIES AND RESEARCH

IN PARTIAL FULFILMENT OF THE REQUIREMENTS FOR THE DEGREE

OF DOCTOR OF PHILOSOPHY

IN

SOLID STATE PHYSICS

DEPARTMENT OF PHYSICS

EDMONTON, ALBERTA

SPRING, 1973

THE UNIVERSITY OF ALBERTA

FACULTY OF GRADUATE STUDIES AND RESEARCH

The undersigned certify that they have read, and recommend to the Faculty of Graduate Studies and Research, for acceptance, a thesis entitled SOME EFFECTS OF SYSTEMATIC REFLECTIONS ON ELECTRON MICROSCOPE IMAGES OF STACKING FAULTS submitted by Kamal Zaki Botros in partial fulfilment of the requirements for the degree of Doctor of Philosophy.

.....
Supervisor

.....

.....

.....

.....
External Examiner

Date April 17th, 1973

ABSTRACT

An investigation of the effects of systematic reflections on the nature of electron microscope images of crystals containing stacking faults has been carried out. At the exact Bragg condition of a low order reflection it was found that effects of systematic reflections can change markedly with crystal thickness and defect depth. Under these diffraction conditions good agreement was obtained between predictions of the two beam dynamical theory and experimental observations when thin or moderately thick crystals were considered. In thicker crystals, however, good agreement with experiment was only obtained by taking the effects of systematic reflections into account in the theory. That defect depth is also a factor in determining whether or not systematic reflections play an important role in image contrast was demonstrated by the fact that fringes near the edges of faults in thick crystals are two beam in character, while the contrast of fringes near the centre of the fault can only be predicted by taking systematic reflections into account.

It was also shown that the effect of low order systematic sets, which is to reduce contrast in thick crystals can be avoided by choosing a high order systematic set. This procedure can give rise to strong contrast in much thicker crystal than would otherwise be possible.

Effects of systematic reflections on image contrast were also studied over a range of crystal orientations. Optimum contrast in the bright field occurred near the Bragg orientation of a low order reflection. Tilting away from this orientation resulted in a rapid decrease in bright field image contrast. Stacking faults in the dark field images exhibited good contrast and were therefore easy to observe over the entire range of orientations considered.

The results of stacking fault contrast obtained under weak beam diffraction conditions showed that the dark field image of a stacking fault is highly sensitive to variations in crystal thickness. When crystal thickness was equal to n effective extinction distances very high contrast was observed. At crystal thicknesses of $(n+\frac{1}{2})$ effective extinction distances the stacking fault could barely be detected. At these crystal thicknesses there is a possibility that errors of interpretation could arise by attributing a phase angle $\alpha = 0$ to the fault.

The dependence of stacking fault contrast in thick crystals on accelerating voltage was explored by performing theoretical calculations which employed the dynamical theory. The results indicated that two beam contrast can persist in thicker crystals if the

accelerating voltage is raised in a certain range of electron energies. These results were obtained provided that the crystal orientation corresponded to the exact Bragg condition of a low order reflection. At very high accelerating voltages (~1000 kV) it was found that thickness fringe and stacking fault contrast in the bright field was significantly improved in thick crystals by tilting away from the symmetry position. These results suggest that the symmetry orientation at high accelerating voltages may not be the best crystal orientation for carrying out observations of stacking faults in thick crystals as suggested by rocking curve data.

Finally in order to gain some insight into the mechanisms which give rise to image contrast, the results obtained in the present work were analyzed in terms of Bloch wave interactions. In order to carry out such an analysis the multibeam expressions describing the inter- and intrabranch scattering of Bloch waves which occur in the faulted crystal were derived. It was found that it is possible to deduce the general behaviour of stacking fault contrast from a knowledge of the number and characteristics of the Bloch waves excited at the top surface of the crystal.

ACKNOWLEDGMENTS

I wish to express my sincere gratitude to Dr. S.S. Sheinin, my research supervisor, for his guidance and constant encouragement throughout the progress of this work. In addition, I would like to thank Dr. P.S. Turner, Mr. C.D. Cann, Mr. J.W. Andrew and Mr. A.E.B. Monk for many helpful discussions.

For assistance in many technical aspects of the work I wish to thank Mr. J.C. Brunel.

For typing the manuscript and figure captions I wish to express my sincere appreciation to Mrs. M. Yiu.

For her patience and encouragement during the course of this work I wish to express my sincere thanks to my wife.

Finally, I wish to thank the University of Alberta and the National Research Council of Canada for financial support throughout the course of this project.

TABLE OF CONTENTS

Page

Page

Page

LIST OF TABLES

LIST OF FUGURES

LIST OF SYMBOLS

symbol	
$\delta\theta_g$	The deviation angle of the reflection g from satisfying its exact Bragg condition
$\Delta\theta_g$	A parameter which indicates the deviation of the lowest order reflection g in a systematic set from its Bragg condition. This parameter is expressed in fractions of Bragg angles, with a sign convention the same as commonly used in the literature for the deviation parameter S_g.
ξ_g^{Δ}	The two beam value of the extinction distance when the reflection g has a deviation parameter equal to $\Delta\theta_g$.
$\bar{\xi}_g^{\Delta}$	The multibeam value of the extinction distance when the lowest order reflection g in a systematic set has a deviation parameter equal to $\Delta\theta_g$.
ϕ_h^i	The contribution of Bloch wave $b^i(\vec{k}^i,\vec{r})$ to the amplitude of the h^{th} diffracted beam.
ϕ_h^{ij}	The contribution of interbranch scattering from Bloch wave b^j into Bloch wave b^i to the amplitude of the h^{th} diffracted beam. If i = j then ϕ_h^{ii} indicates an intrabranch contribution.
t_1	The depth of a stacking fault in a crystal.
t	Crystal thickness.

CHAPTER 1

INTRODUCTION

The classic work of Heidenreich [1] has shown that the intensity of high energy electrons transmitted through thin sections of crystalline matter depends upon both the thickness and orientation of the specimen. These early experiments laid the physical basis for the powerful technique of transmission electron miscroscopy which enables electron images of crystals containing lattice imperfections to be obtained.

In the early developments of transmission electron microscopy, (see for example the work of Hirsch, HOwie and Whelan [2]) image contrast was interpreted in terms of the kinematical theory of electron diffraction. This theory gave electron microscopists a qualitative description of image properties. It became evident, however, that the kinematical approach suffered from major difficulties when predictions of the theory were tested by experimental observations (see section 1:3.1(a), and references [3 to 8]). Due to the limited applicability of the kinematical approach electron microscopists turned to the dynamical theory of electron diffraction in an attempt to explain experimental observations.

The dynamical theory was proposed by Bethe [9] in 1928. In his theory Bethe gave a wave mechanical description for the motion of the high energy electrons in the periodic potential of the crystal. This treatment resulted in an infinite set of equations relating the amplitude coefficients of the Bloch waves excited in the crystal, and thus no general expression for image intensity could be deduced. Therefore, in order to obtain solutions to problems in electron diffraction, approximations had to be made. The simplest approximation to make is that there are only two important beams, the directly transmitted beam and one diffracted beam. This two-beam dynamical theory has been widely used in calculations of diffraction contrast, both in perfect and in lattice defect containing crystals. Although the theory has been successful in providing a qualitative understanding of diffraction contrast, its applicability is limited because in practice it is not possible to excite only two beams. The situation which best satisfies two beam diffraction conditions is obtained by orienting the crystal such that only one low order reflection, g, satisfies Bragg's law. However, even under these conditions the systematic reflections ..., -2g, -g, 2g, ... are always excited.

Previous work which examined diffraction phenomena in perfect crystals has indicated that for certain

diffraction conditions experimental results could only be explained by taking these systematic reflections into account. Prior to the work undertaken in this thesis some results had also been reported on the effects of systematic reflections on images of lattice defect such as stacking faults indicating that in this case as well, the two beam theory was limited in its applicability. However, no extensive investigation of the effects of systematic reflections on stacking fault contrast had been reported. It was with this objective in mind that the work presented in this thesis was undertaken.

As an introduction to the presentation of the results obtained on the effects of systematic reflections on stacking fault contrast, it was thought important to give an account of the previous work concerned with the interpretation of the nature of stacking fault images obtained in transmission electron microscopy. This chapter is therefore devoted to a literature survey of such studies (section 1:3), as well as describing in more detail the objectives of the present work (section 1:4).

1:1 STRUCTURAL ASPECTS OF STACKING FAULTS IN CLOSE PACKED STRUCTURES

Close packed structures are generated by stacking close packed layers on top of one another in the fashion illustrated in fig. 1. Given a layer A, close packing can be extended by stacking the next layer so that its atoms occupy B or C sites, where A, B and C refer to the three possible layer positions in a projection normal to the close packed layers (see fig. 1). It is important to note that close packing is generated provided that two layers of the same letter, such as AA, are not stacked in juxtaposition to one another.

The stacking sequence corresponding to an fcc crystal type is:

... A B C A B C ...

while in an hcp crystal the third alternate layer is always missing and the sequence becomes:

... A B A B A B ...

In fcc crystals the close-packed planes are of the {111} type, while in hcp lattices these are the {0001} planes. It is possible, without destroying the close packing of the crystal, to change from one packing sequence to another. Thus we may have breaks in the

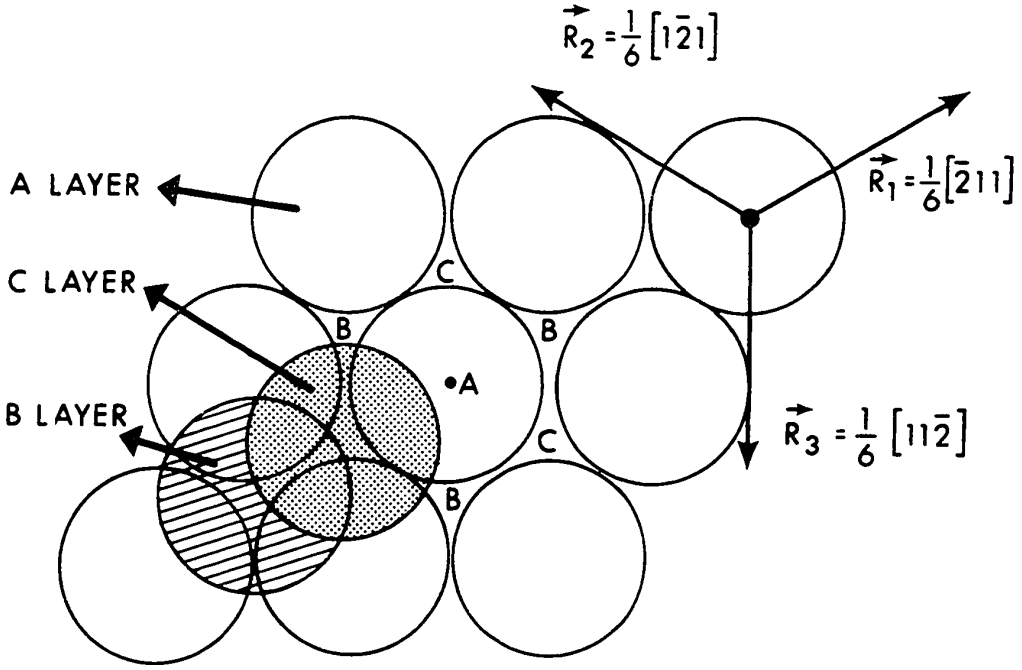

Fig. 1 Packing of atoms in close packed structures. Note that the displacement vectors

$$\vec{R}_1 \ , \quad \vec{R}_2 \ , \quad \text{and} \quad \vec{R}_3$$

are given in cubic notation. If hexagonal notation is used, then

$$\vec{R}_1 = \frac{1}{3}[01\bar{1}0]$$

$$\vec{R}_2 = \frac{1}{3}[\bar{1}010]$$

$$\vec{R}_3 = \frac{1}{3}[1\bar{1}00]$$

stacking order, as for example, in the cubic case,

... A B C A ↓ C A B C A ...

or in the hexagonal case,

... A B A B ↓ C A C A C ...

The arrows indicate where breaks occur in the correct stacking order, defining a stacking fault.

1:1.1 TYPES OF FAULTS IN CLOSE PACKED STRUCTURES

A classification of the types of stacking faults, in close packed structures, has been discussed by Frank [10], who classified them as being either intrinsic or extrinsic. In the intrinsic type, a fault is formed by removing one atomic layer from the normal stacking sequence. Thus for example, if we consider an fcc structure, an intrinsic fault can be formed by the removal of an A layer, giving:

... A B C A B C ↓ B C A B C ...

An extrinsic stacking fault on the other hand, is formed by the addition of a layer of atoms to the normal stacking sequence, giving:

... A B C A B C ↓ B A B C A B C ...

It is important to realize that the above types of faults can be produced by shearing operations in the {111} planes in the fcc case, and in the {0001} planes of the hcp structure. In order to clarify this point, suppose that the plane marked A in fig. 1 is a plane in a perfect fcc crystal, and that the next plane above it is a B plane. If the B plane and all the planes above it are displaced by a vector $\frac{1}{6}$ $[\bar{2}11]$ the B plane will move into a C position, and the planes above it undergo the transition: A → B, B → C, and C → A, relative to the position fixed in the original A plane. This shear displacement $\vec{R}_1$ in fig. 1 is represented by the arrows in the following reaction,

$$\begin{array}{cccccccccccc} \ldots & A & B & C & A & B & C & A & B & C & \ldots \\ & & & & & \downarrow & \downarrow & \downarrow & \downarrow & \downarrow & \\ & & & & & C & A & B & C & A & \end{array}$$

giving the intrinsic fault,

$$\begin{array}{cccccccccc} \ldots & A & B & C & A & \downarrow & A & B & C & A & \ldots \\ & & & & & C & & & & & \end{array}$$

An extrinsic fault can be produced, on the other hand, if the C plane below the fixed A plane and all successive lower planes are displaced by $(-\vec{R}_1)$ i.e., with a displacement equal to $\frac{1}{6}$ $[2\bar{1}\bar{1}]$.

1:2 THE TECHNIQUE OF TRANSMISSION ELECTRON MICROSCOPY

The technique of transmission electron microscopy (TEM) has been extensively used to study lattice defects in crystalline matter. Although the initial work of Heidenreich [1] in 1949 showed considerable promise, it was nearly 10 years later before any further developments of the technique took place. The developments which laid the basis for the extensive application of TEM in material sciences are:

(1) The use of the electropolishing techniques for preparing thin specimens, due to Bollmann [11].

(2) The improvements in resolution of the electron microscope and the availability of the double condenser system.

(3) The design of specimen stages which permit the specimen to be manipulated inside the microscope.

(4) The development of a theory of contrast in images of crystal defects. A detailed review of this theory is given in Chapter 2 with particular reference to stacking fault images. A literature survey of the relevant experiments which have been carried out using the technique of TEM, and the interpreteration of the results obtained by using the different theories of diffraction contrast will be given in the next section.

1:3 PREVIOUS WORK ON THE INTERPRETATION OF THE NATURE OF STACKING FAULT IMAGES

The first explanation of the nature of stacking fault images was based on the assumption that only two diffracted beams give rise to image contrast. Sections 1:3.1(a), (b), (c), and (d) will present an account of the two-beam interpretation of stacking fault contrast. In the later sections, 1:3.2 and 1:3.3, the results of previous investigations concerned with studying the effects of other reflections will be reviewed.

1:3.1 TWO BEAM INTERPRETATION OF STACKING FAULT CONTRAST

Two different approaches [2,12] have been adopted in considering the nature of stacking fault contrast obtained when only two diffracted beams are considered. The first of these is the kinematical approach [2] where the assumptions made are:

(1) An electron can only be scattered once, and

(2) The depletion of the incident electron beam while progressing through the crystal can be ignored.

These assumptions resulted in the kinematical theory [2] being limited to very thin crystals when the crystal orientation is near to satisfying the Bragg condition of a low order reflection. However, for large deviations

from the Bragg condition, the kinematical approach will be better approximation in thicker crystals. On the other hand, in the two beam dynamical theory [12] the assumptions of the kinematical approach are not required and the above limitations are therefore removed.

1:3.1(a) Results of the Kinematical Approach

Hirsch, Howie, and Whelan [2] were the first to use the two beam kinematical approach in order to obtain the properties of stacking fault images. In their calculations they considered a fault which was sloping with respect to the surfaces of a thin crystal. They assumed that the effect of the fault was to cause an abrupt phase change $\alpha = 2\pi\vec{g}.\vec{R}$ of the two diffracted waves. $\vec{R}$ is the displacement vector of the fault defined in section 1:1.1, and $\vec{g}$ is the reciprocal lattice vector corresponding to the diffracted beam concerned. They found that the intensity of the diffracted beam along the bottom surface of the faulted crystal is given by,

$$I_g = \frac{1}{\pi^2 S_g^2} \{\sin^2(\pi t S_g - \alpha/2) + \sin^2 \alpha/2 + 2 \sin \frac{\alpha}{2} \sin(\pi t S_g - \alpha/2) \cos \pi S_g (t - 2t_1) \quad (1.1)$$

where S_g is a deviation parameter with magnitude equal

to the distance of the reciprocal lattice point g from the Ewald sphere in a direction perpendicular to the top surface of the crystal, t is the crystal thickness, and t_1 is the depth of the fault in the crystal. The above equation describes the properties of the dark field image. The bright field image in the kinematical approach is obtained by assuming $I_o = (1 - I_g)$, where I_o is the intensity of the directly transmitted beam.

The kinematical approach of Hirsch et al [2], although containing over-simplified assumptions, was able to explain the fact that stacking fault images consisted of fringes (see equation 1.1). The periodicity of these intensity variations given by the kinematical theory can be seen from equation 1.1 to be equal to $\xi_g = S_g^{-1}$ where the parameter, ξ_g, is commonly known as the extinction distance.

1:3.1(b) Failure of the Kinematical Approach and Interpretation of Fault Contrast by Using the Two-Beam Dynamical Theory

Whelan and Hirsch [12] re-examined the results of the kinematical approach and pointed out that such an approach cannot explain the nature of image contrast when the deviation parameter S_g is sufficiently small. Under these conditions the reflection, g, will be close

to its exact Bragg condition, and equation 1.1 predicts fringes with periodicity tending to infinity. Since this was clearly an unacceptable result, Whelan and Hirsch [12] decided to analyze stacking fault image in terms of the two beam dynamical theory. The expression for the amplitude of the directly transmitted beam, ϕ_o, at the bottom surface of the faulted crystal which they obtained was,

$$\phi_o = \cos\left(\frac{\pi t}{\xi_g}\right) - i \cos\beta \sin\left(\frac{\pi t}{\xi_g}\right) + \frac{(e^{-i\alpha} - 1)\sin^2\beta}{2}\left[\cos\left(\frac{\pi t}{\xi_g}\right) - \cos\frac{\pi(2t_1 - t)}{\xi_g}\right] \quad (1.2)$$

The parameter β, in equation 1.2, is a deviation parameter with $\beta = \pi/2$ at the exact Bragg condition, and $\beta \to 0$ for very large deviations from the Bragg condition. In the two beam theory the extinction distance ξ_g depends on the deviation parameter through the relation $\xi_g(\beta) = \xi_g(\beta = \pi/2)/(1 + \cot^2\beta)^{\frac{1}{2}}$. It can thus be seen that the extinction distance tends to a finite value $\xi_g(\beta = \pi/2)$, at the exact Bragg condition, and decreases as crystal is tilted away from this orientation, thus avoiding the difficulties of the kinematical theory.

Whelan and Hirsch [12] have used equation 1.2 to describe the properties of the bright field stacking fault image. A survey of the fringe patterns obtained

under different conditions was given in their original paper [13]. The characteristics of these fringe patterns are summarized below:

(a) Fringe periodicity is $\xi_g/2$, i.e., fringes are doublets rather than singlets as predicted by the kinematical approach. Thus for a given value of the deviation parameter β, increasing crystal thickness by one extinction distance results in the generation of two new fringes in the stacking fault image.

(b) Fringes across the stacking fault have the same contrast, i.e., there is no change in fringe visibility across the fault.

(c) If crystal thickness is kept constant, tilting away from the Bragg condition results in a decrease in the visibility of stacking fault fringes. This is seen from equation 1.2 which shows that the value of $\sin^2\beta$ decreases as the crystal is tilted away from the Bragg condition, and as a consequence the last term in the expression for ϕ_o will have smaller contribution.

It is important to note that properties of dark field stacking fault image in the two beam theory were found to be generally similar to those discussed above for the bright field image, except that [13] bright and dark field images were predicted to be complementary

in nature.

1:3.1(c) Effects of Absorption on Stacking Fault Contrast

Although the agreement between the two beam theory of Whelan and Hirsch [12] with experimental observations was certainly better than that of the kinematical theory, good agreement was only obtained [13] when thin crystals were considered. The experimental observations of Hashimoto et.al.[14] indicated that fault contrast obtained in thick crystals was quite different from that given in section 1:3.1(b).

These differences were:

(a) Contrast in a stacking fault image depended on the depth of the fault in the crystal. For a thick crystal a marked decrease in the visibility of fringes near the centre of the fault was observed both in the bright and dark field.

(b) Bright and dark field images were found not to be complementary to one another. Bright field images on one hand exhibited fringes which were symmetrical about the centre of the fault, while dark field images on the other hand were asymmetrical. It might be noted that these properties of stacking fault images in thick crystals have been used to distinguish between top and bottom surfaces of the crystal.

Hashimoto et.al. [14] in an attempt to explain their experimental observations introduced the concept of absorption. Their arguments were that in a thick crystal, some of the high energy electrons are inelastically scattered. These electrons can give rise to 'absorption' effects since they may be scattered outside the objective aperture of the microscope and will therefore not contribute to the image.

Effects of absorption were included phenomenologically [14] in the two beam theory through the addition of an imaginary part to the crystal potential. When Hashimoto et.al. [14] used this approach good agreement was obtained between theory and experimental observations in thick crystals.

In a later paper Hashimoto et.al. [15] studied the mechanism responsible for producing fault contrast in thick crystals. This was done by examining scattering transitions between Bloch waves. These results will be discussed in more detail in section 2:6 of Chapter 2. This method of analysis was also used by Drum and Whelan [16] to study the contrast resulting from $\alpha = \pi$ stacking faults in AlN. The contrast of this type of fault was found [16,17] to be similar to that of an $\alpha = 2\pi/3$ fault when thin crystals were considered. In thick crystals

effects of absorption become important and no contrast was found [16,17] to result from π-faults. This was used [17,18] as a method to distinguish between the two kinds of stacking faults.

1:3.1(d) Other Work

A number of other workers have made significant contributions to the understanding of the nature of stacking fault contrast obtained by using the two-beam dynamical theory. Gevers [19] and Gevers, Art and Amelenickx [20] studied stacking fault image contrast through an examination of the mathematical expressions for image intensity in the two-beam theory. Using this approach these authors [20] have found that the central fringes in a stacking fault image which exhibit weak contrast could be singlets or doublets depending on the value of total crystal thickness. Although these authors have made many other contributions to the literature on stacking fault contrast, these are not reviewed here as they do not pertain directly to the present investigation.

Other studies of stacking fault contrast included the work of Booker [21], Booker and Hazzeledine [22] who studied the dependence of contrast on different parameters which appear in the two beam theory. The parameters they studied were:

(a) The value of α in the range $\pi/10$ to π.

(b) The deviation parameter $w = \cot \beta$ (see equation 1.2) in the range ± 0.4.

(c) The magnitude of anomalous absorption parameters in the range 0.035 to 0.1.

In calculating their intensity profiles both in the bright and dark field the only fixed parameter was the value of total crystal thickness which was taken to be six times the extinction distance. The main additional features of stacking fault contrast obtained from these theoretical calculations were:

(a) All bright field profiles exhibited fringes which are symmetrical with respect to the centre of the fault. On the other hand all dark field profiles were asymmetrical except for $\alpha = \pi$ at $w = 0$.

(b) When $w = 0$ and $\alpha = \pi$, stacking fringes exhibit very weak contrast (as found by Drum and Whelan [16]). On the other hand, for $w \neq 0$ strong fringes are generated.

(c) Effects of absorption were such that the image obtained at a given orientation is characterized by main fringes and subsidiary fringes. This complex fringe pattern was found [21,22] to be highly sensitive to changes in the value of α and w, and also the value of anomalous absorption parameters used.

Finally in this section it is important to mention the work of Head [23] and Humble [24,25]. These authors have described a method of producing simulated images of stacking faults which employs the two beam dynamical theory. The information is presented, not in the form of profiles, but as half-tone pictures using the computer line printer. Humble [25] used this method to study the contrast due to overlapping $2\pi/3$ faults. He found that although $\alpha = 2\pi$ for 3 overlapping stacking faults, there was still some contrast retained, possibly due to the strain field of a nearby dislocation. Similar interesting contrast features were found by Morton and Clarebrough [26] in studies involving different fault configurations and interactions.

1:3.2 PREVIOUS RESULTS INDICATING THE IMPORTANCE OF OTHER REFLECTIONS ON DIFFRACTION CONTRAST

Up to this point all the work mentioned has assumed the validity of the two beam approximation of the dynamical theory. There has been, however, considerable work on diffraction phenomena in perfect crystals which indicates that the two-beam theory has a limited degree of validity. For example the work of Sheinin [27] and Goringe et.al. [28] on the effects of systematic reflections on extinction distance have shown that marked deviations from the two beam extinction distance can occur due to the presence

of systematic reflections. Systematic reflections were also found to alter image intensity (Howie [29]) and image contrast in perfect crystals (Fukuhara [30], and Goodman and Lehmfuhl[31]) from their two beam values. Previous work reported in the literature [27 to 33] has shown that the effects of systematic reflections on images of perfect crystals are determined by the following parameters:

(a) type of material and image considered

(b) accelerating voltage

(c) the deviation of the lowest order reflection, g, in a systematic set from its exact Bragg condition.

Previous work which considered effects of systematic reflections on the nature of stacking fault contrast is considered in the next section.

1:3.3 STUDIES OF THE EFFECTS OF SYSTEMATIC REFLECTIONS ON STACKING FAULT CONTRAST

Prior to the work presented in this thesis only few investigations have studied some aspects of stacking fault contrast due to the presence of systematic reflections. One such investigation was that of Humphreys, Howie, and Booker [34]. These authors have used the two and multibeam dynamical theories to

calculate fault profiles in both bright and dark field images of stacking faults. The orientation they considered corresponded to setting the crystal at the exact Bragg condition of a low order reflection. When these calculations were performed for the (220) systematic set in silicon, they found that there were no differences between the two and multibeam profiles. However, when the (111) set of systematic reflections in gold was considered, large differences were found between the two and multibeam profiles. In this case the multibeam profiles indicated that stacking fault fringes should exhibit higher contrast than predicted by the two beam theory. Another difference was found for fringes near the centre of the fault. Multibeam fringes for these fault depths did not show a marked decrease in visibility as was the case for the two beam profiles. The conclusion of Humphreys et.al. [34] was therefore that effects of systematic reflections are quite weak in materials of low atomic number like silicon, while these effects can be quite pronounced in materials of high atomic number, like gold.

Gevers, Van Landuyt and Amelinckx [35] studied the effects of systematic reflections in a different manner. The orientation they considered also corresponded to setting the crystal at the exact Bragg

condition of a low order reflection. These authors [35] obtained the properties of higher order dark field images by considering the reflections -2g, 2g, ... etc. In their calculations the two strong reflections in a systematic set were considered to interact according to the dynamical theory. However the other reflections were considered to be 'weak' so that their dynamic interactions were neglected. The intensities of these diffracted beams along the bottom surface of the faulted crystal were obtained by using a kinematical approach similar to that described in section 1:3.1(a). In order to test their theory, high order dark field images of stacking faults in stainless steel were recorded. They found that the experimental results they obtained did not show some of the fine details predicted by their theory. Gevers et.al. [35] attributed the lack of good agreement as being due to poor image quality resulting from lens abberations in the electron microscope.

1:4 OBJECTIVES OF THE PRESENT WORK

The previous work described in section 1:3.3 has indicated that systematic reflections can have an effect on stacking fault contrast. However a detailed study of the nature of these effects and the conditions under which they occur has not been previously carried out.

The present work was therefore undertaken to explore for a variety of diffraction conditions, the manner in which stacking fault image contrast is influenced by the presence of systematic reflections.

The first question which arose in defining the approach to be adopted in this investigation was the following: What are the different parameters which can influence the role that systematics play on stacking fault contrast? Guided by the factors which are important in producing contrast when two beams only are important, the possible parameters in the multibeam situation were taken to be:

(i) The type of reflection in the material considered.

(ii) The phase angle of the fault $\alpha = 2\pi\vec{g}.\vec{R}$, and the crystal structure of the material.

(iii) The deviation of the lowest order reflection of a systematic set from its Bragg condition, and the accelerating voltage employed.

(iv) Depth of the fault in the crystal, and the value of crystal thickness.

(v) Whether the image considered is bright or dark field.

It was realized at the outset that a simultaneous study of all the above parameters would be prohibitive. Thus the investigation was divided into four separate

areas. The first three of these were concerned with exploring the nature of stacking fault contrast at low accelerating voltages under a wide variety of conditions, and the fourth was devoted to studying the effects on stacking fault contrast of raising electron energy. In the following few sections the objectives of each area of study are given in greater detail.

1:4.1 INVESTIGATIONS OF STACKING FAULT CONTRAST AT LOW ACCELERATING VOLTAGES WHEN A LOW ORDER REFLECTION SATISFIES THE EXACT BRAGG CONDITION

Strong beam images of lattice defects [36 to 41] are normally observed in the conventional low voltage microscopy by setting the crystal so that the lowest order reflection, g, of a systematic set is quite close to its exact Bragg condition. It has been commonly assumed (see section 1:3.1) that the fault image obtained under these strong beam diffraction conditions can be adequately described by the two beam approximation of the dynamical theory. The theoretical calculations of Humphreys et.al. [34] (see section 1:3.3) have indicated however that strong beam images of stacking faults are affected by the presence of systematic reflections in materials of high atomic number. The possibility that factors other than atomic number might play an important

role in determining the effects of systematic reflections, has not been previously explored. These factors can be:

(i) Defect depth and crystal thickness.

(ii) The row of systematic reflections excited.

(iii) Whether the image is bright or dark field.

In order to explore the effects of the above parameters, an experimental study was undertaken. In this investigation image contrast was studied over a range of crystal thicknesses and different systematic sets of reflections were considered. The results obtained are given in chapter 5.

In order to determine whether or not the observed images were affected by the presence of systematic reflections, the experimental results must be compared to the predictions of the two and multibeam dynamical theories. However in order to carry out such a comparison absorption must be included in the theory. This required an accurate knowledge of the appropriate absorption parameters in the material investigated. To this end an experimental method was developed to measure the values of the absorption parameters (see sections 3:3.1, 3:3.2 of chapter 3).

1:4.2 INVESTIGATION OF THE EFFECTS OF TILTING ON THE NATURE OF STACKING FAULT IMAGES

Previous work [42] has shown that the nature of thickness fringes in images of crystal wedges can change appreciably by tilting the crystal away from strong beam diffraction conditions. These results suggested the possibility that crystal orientation can also be an important factor in determining whether or not stacking fault images will be affected by the presence of systematic reflections. Since this question had not received much attention in the literature an investigation of the dependence of stacking fault contrast on the deviation parameter S_g was undertaken. The results are presented in chapter 6 of this thesis.

1:4.3 INVESTIGATION OF STACKING FAULT CONTRAST OBTAINED UNDER WEAK BEAM DIFFRACTION CONDITIONS

The recent work of Cockayne, Ray and Whelan [43] has shown that significant improvements of images of dislocations can be obtained from dark field micrographs recorded under weak beam diffraction conditions. Thus for example,for the case of partial dislocations, each partial appears as a sharp peak of excellent contrast superimposed on a low background intensity.

The nature of the stacking fault image to be obtained when the crystal is tilted to the high values

of the deviation parameter S_g, corresponding to weak beam diffraction conditions, has not been previously investigated. As a result a study of the different factors affecting stacking fault contrast under these weak beam conditions was undertaken (see chapter 7).

1:4.4 INVESTIGATION OF STACKING FAULT CONTRAST OBTAINED AT HIGH ACCELERATING VOLTAGES

There is considerable current interest in using high voltage electron microscopes to observe thicker specimens than would otherwise be possible. In the development of physical techniques to be used in obtaining maximum penetration, electron microscopists have explored the conditions which maximize electron transmission through perfect crystals [44 to 50]. Very limited work, however, has been reported on how stacking fault contrast would change as a result of raising the electron energy. This point and its implication regarding observations of stacking faults in thick crystals, is investigated in some detail in the present work. The results are presented in chapter 8.

1:4.5 ANALYSIS OF STACKING FAULT IMAGES IN TERMS OF THE SCATTERING MECHANISMS RESPONSIBLE FOR PRODUCING CONTRAST

As indicated in section 1:3.1(c), Hashimoto et.al. [15] were able to explain the nature of stacking fault contrast in thick crystals oriented under strong beam diffraction conditions by studying the interactions of the two Bloch waves appearing in the two beam theory. This method offers a basic understanding of image contrast since it explores the scattering mechanisms which are responsible for producing contrast. However, in order to analyze the results of the present investigation, the theory had to be extended to the multibeam case. This is done in chapter 4. This multibeam theory of Bloch wave transitions is then used in chapters 5 to 8 to analyze stacking fault contrast obtained under a wide variety of conditions.

CHAPTER 2

ASPECTS OF THE DYNAMICAL THEORY OF ELECTRON DIFFRACTION

2:1 REVIEW OF DYNAMICAL THEORY FOR PERFECT CRYSTALS

2:1.1 BASIC OUTLINE OF THE THEORY

The dynamical theory of electron diffraction, as first proposed by Bethe [9] and further developed by Mcgillavry [51] and Heidenreich [1], starts with Schrödinger equation which describes the motion of the high energy electron in the potential field of the crystal $V(\vec{r})$. This equation can be written as

$$\nabla^2\psi(\vec{r}) + \frac{8\pi^2 m_o e}{h^2}(E + V(\vec{r}))\psi(\vec{r}) = 0$$

where $\psi(\vec{r})$ is the wave function of the electron, $\vec{r}$ is a position vector, m_o and e are the rest mass and charge of the electron, E is the potential through which the electron is accelerated before entering the crystal, and h is Planck's constant.

Since the crystal potential is periodic in nature it can be expressed in the form of a Fourier series:

$$V(\vec{r}) = V_o + \sum_g{}' V_g \exp 2\pi i\vec{g}.\vec{r} \quad . \qquad (2.1)$$

V_o is the mean inner lattice potential, $\vec{g}$ is a reciprocal lattice vector, and V_g is the g^{th} Fourier coefficient of

the lattice potential. The prime in the summation indicates that the term g = 0 is excluded.

In the case of electron energies normally employed in transmission electron microscopy, $E >> V(\vec{r})$ and it is thus possible to solve Schrödinger equation by using a perturbation approach. The solutions outside the crystal, when $V(\vec{r}) = 0$, are plane waves of the form $\exp 2\pi i\vec{\chi}.\vec{r}$, where the magnitude of the wave vector $\vec{\chi}$ is given by

$$eE = h^2\chi^2/2m \quad .$$

The effect of the lattice potential is to give solutions which are combination of plane waves. Since the potential is periodic these solutions must be Bloch functions of the form

$$b(\vec{k}^i,\vec{r}) = \sum_g C_g(\vec{k}^i) \exp 2\pi i(\vec{k}^i + \vec{g}).\vec{r} \qquad (2.2)$$

where $\vec{k}^i$ represents the Bloch wave vector. Substituting equations (2.1) and (2.2) into Schrödinger equation gives,

$$\sum_g \left[-(\vec{k}^i+g)^2 C_g(\vec{k}^i) + \frac{2m_o e}{h^2}(E+V_o) C_g(\vec{k}^i) + \frac{2m_o e}{h^2} \sum{}' C_{g-h}(\vec{k}^i)V_h\right]e^{2\pi i(\vec{k}^i+\vec{g}).\vec{r}} = 0 \ ,$$

where the prime on the second summation indicates the exclusion of the term h = 0. Since the terms $2\pi i(\vec{k}^i+\vec{g}).\vec{r}$

are linearly independent, their coefficients must all be identically equal to zero. This condition results in a set of equations of the form

$$[K^2 - (\vec{k}^i + \vec{g})^2]C_g(\vec{k}^i) + \sum_h{}' C_{g-h}(\vec{k}^i)U_h = 0 \qquad (2.3)$$

where,

$$K^2 = \frac{2m_o e}{h^2}(E + V_o)$$

and,

$$U_g = \frac{2m_o e}{h^2} V_g \quad . \qquad (2.4)$$

$\vec{K}$ in equations 2.4 is a wave vector, associated with the mean lattice potential V_o.

The above set of equations 2.3, called by Bethe [9] the dispersion equation, gives the general relationship between the amplitude coefficients C_g, the Fourier coefficients U_g and the Bloch wave vectors $\vec{k}^i$.

The question which arises at this stage is what approach should be taken in solving the dispersion relation of equation 2.3. One approach which has been extensively used in the past [12, 52] is to assume that only two beams are important. Under these circumstances the dispersion relation 2.3 consists of only two equations for which analytical solutions exist. However, in the

present work we are primarily interested in studying the effects of systematic reflections. If n systematic reflections are considered then the dispersion relation 2.3 consists of n equations for which analytical solution cannot generally be found. Numerical solutions of these equations must therefore be adopted. There have been a number of formulations of the multi-beam dynamical theory which can be used to obtain such numerical solutions (see for example Sturkey [53], Fujimoto [54], Niehrs [55 to 57] and Fisher [58]). The formulation considered in the present work is that of Howie and Whelan [59] which reduces the problem to an Eigen-Value equation. This formulation is particularly useful since any number of beams can be included and since the form of the equation is most suitable for numerical solutions.

The manner in which the Eigen-Value equation is derived can be understood by considering Fig. 2. This figure shows the dispersion surface drawn for the two beam case, $\vec{K}$ being the electron wave vector after allowing for effects of refraction. The wave points of the possible Bloch waves inside the crystal are obtained from the condition that the tangential components of the possible Bloch wave vectors must be equal to that of the incident beam. Thus through a point A we draw a line

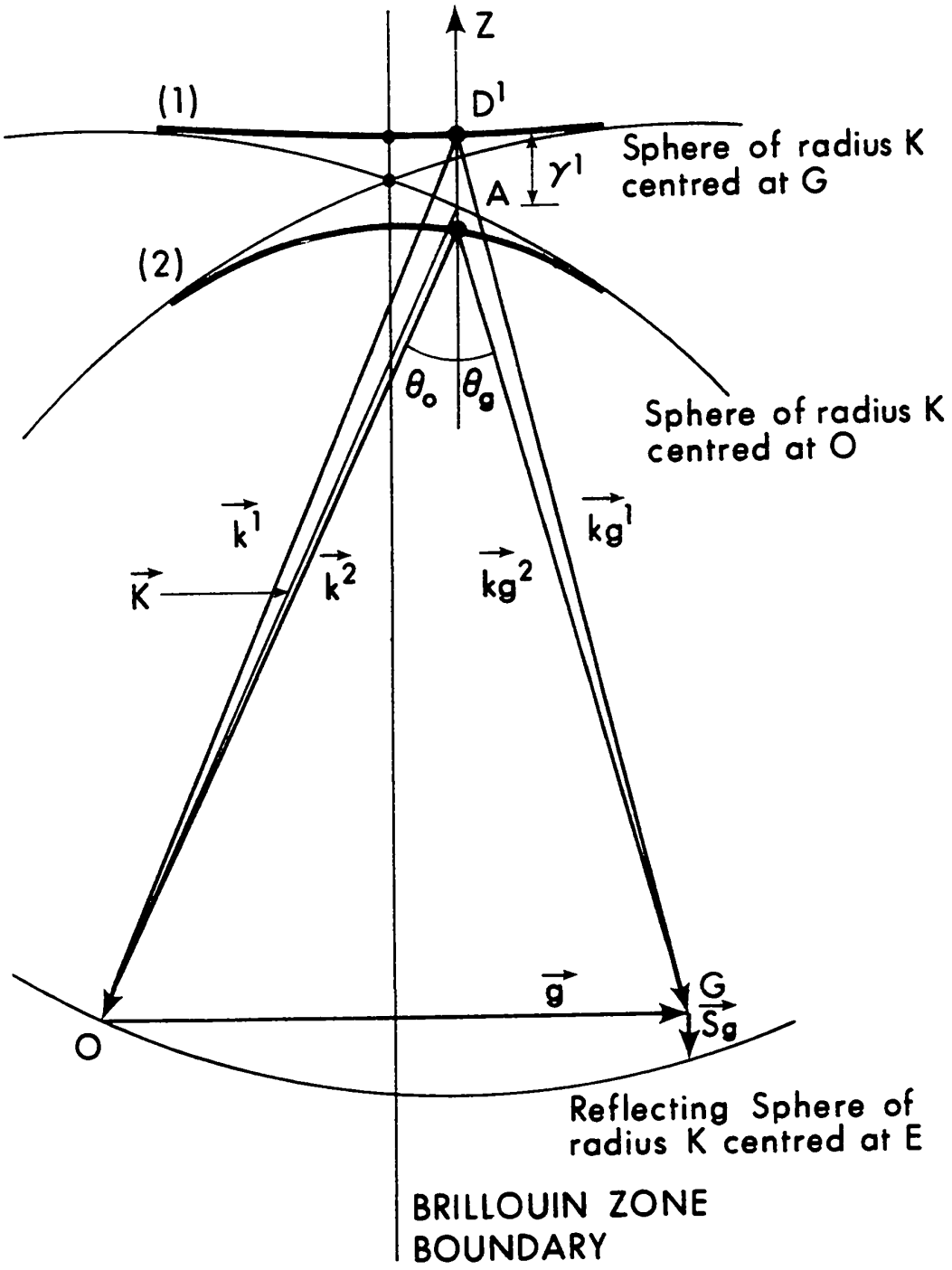

Fig. 2 The dispersion surface for high energy electrons in the two beam approximation. The two Bloch waves excited have wave vectors $\vec{k}^1$, and $\vec{k}^2$ respectively.

normal to the entrance surface of the crystal to intersect the branches of the dispersion surface. In the symmetrical Laue case shown in Fig. 2 this line will be parallel to the Brillouin zone boundary, but our arguments still hold to a very good approximation even if the Bragg reflecting planes are not exactly perpendicular to the crystal surface. Now let γ, as shown in Fig. 2, be the distance of a possible wave point from A, and let S_g be the distance of the reciprocal lattice point g from the Ewald sphere, measured in a direction normal to the reciprocal lattice vector $\vec{g}$ in the z-direction. From Fig. 2 we can see, for small γ and S_g, that

$$K^2 - k^2 \simeq K^2 - (K + \gamma \cos \theta_o)^2 \simeq -2K\gamma \cos \theta_o$$

$$K^2 - (k+g)^2 \simeq K^2 - (K + (\gamma - S_g)\cos \theta_g)^2 \simeq 2K(S_g - \gamma)\cos \theta_g \ . \tag{2.5}$$

Substituting these expressions into the dispersion equation 2.3, we obtain the eigen value equation,

$$\underline{A}\ \underline{C}^{\,i} = \gamma^i\ \underline{C}^i \ . \tag{2.6}$$

Here, $\underline{C}^i$ is a column vector whose elements C_g^i are the components of the Bloch wave eigen vector, $\underline{A}$ is a matrix with elements $A_{oo} = 0$, $A_{gg} = S_g$, $A_{gh} = U_{g-h}/2K$ where $g \neq h$ (we have assumed $\cos \theta_o \sim \cos \theta_g \sim 1$ in equation 2.5), and γ^i is the corresponding eigen value. If we

consider a crystal with a centre of symmetry, then the Fourier components U_g of the crystal lattice potential are real, positive quantities. Under these conditions $U_g = U_{-g}$ and the matrix $\underline{A}$ will be a real, symmetric matrix since, $A_{gh} = A_{hg} = U_{g-h}/2K$.

As indicated by equation 2.6, the problem now is reduced to an eigen value equation, and the inclusion of any desired number of reflections is possible. If n beams are considered the matrix $\underline{A}$ will be an $n \times n$ symmetric matrix, whose diagonal elements depend upon S_g the deviation parameter of each reflection considered, and whose non-diagonal elements depend upon the Fourier components of the crystal potential. Given such an input matrix, computer programs can be written to calculate n eigen values γ^i and the associated eigen vectors $[C_o^i \ldots C_h^i \ldots]$. By carrying out such matrix diagonalization procedures for a series of crystal orientations, it is possible to determine the shape of the different branches of the dispersion surface as well as the exact form of each Bloch wave associated with every point on it.

2:2 CALCULATION OF THE AMPLITUDES OF THE DIFFERENT DIFFRACTED BEAMS IN A PERFECT CRYSTAL

The total wave function $\psi(\vec{r})$, of the high energy electron inside the crystal, can be written as a linear

combination of all the Bloch waves $b^i(\vec{k}^i,\vec{r})$ excited as follows:

$$\psi(\vec{r}) = \sum_{i=1}^{N} \psi^i \, b^i(\vec{k}^i,\vec{r}) \qquad (2.7)$$

where the coefficient ψ^i, commonly known as excitation amplitudes, determine the extent to which the associated Bloch waves are excited inside the crystal. In order to calculate the diffracted wave amplitudes, the different terms in the summation of equation 2.7 can be sorted out into components in the directions of the directly transmitted and diffracted beams. The expression for a particular diffracted beam ϕ_h can be seen from equation 2.7 to be,

$$\phi_h = \sum_i \psi^i \, C_h^i \exp 2\pi i(\vec{k}^i + \vec{h}).\vec{r} \qquad (2.8)$$

Now if equation 2.8 is multiplied through by the phase factor $\exp -2\pi i\vec{K}.\vec{r}$, we get

$$\phi_h \, e^{-2\pi i\vec{K}.\vec{r}} = \sum_i \psi^i \, C_h^i \exp 2\pi i(\vec{\gamma}^i + \vec{h}).\vec{r}$$

but since the eigen values, $\vec{\gamma}^i$, are defined to be in the z-direction, (see Fig. 2), the above equation will reduce to

$$\phi_h \, e^{-2\pi i\vec{K}.\vec{r}} = \sum_i \psi^i \, C_h^i \exp 2\pi i(\gamma^i + h)z \quad . \qquad (2.9)$$

The phase term on the left hand side of equation 2.9 can in fact be dropped out since it will not affect the final intensity of that beam. Furthermore, if we assume propagation to be mainly in z-direction then the amplitude of the diffracted beam at a depth z in the crystal will be given by,

$$\phi_h(z) = \sum_i \psi^i \, C_h^i \exp 2\pi i(\gamma^i + h)z \quad . \tag{2.10}$$

Similar exeressions to equation 2.10 can be written for all the other diffracted beams. All these equations can now be reduced to one matrix equation of the form,

$$\underline{\phi}_g(z) = \underline{C} \{\exp 2 i\pi \gamma^i z\} \underline{\psi} \tag{2.11}$$

where $\underline{C}$ is a matrix whose elements are the eigen vectors of equation 2.6, $\underline{\psi}$ is a column vector whose elements are the excitation amplitudes of the Bloch waves on various branches of the dispersion surface, and the curly bracket indicates a diagonal matrix, with non-zero elements equal to $\exp 2\pi i\gamma^i z$. We proceed now to calculate the elements of the vector $\underline{\psi}$. Equation 2.11 can be written at the top surface of the crystal (z=0) as

$$\underline{\phi}_g(0) = \underline{C} \, \underline{\psi} \tag{2.12}$$

Since $\underline{A}$ is a real and symmetric matrix, the $\underline{C}$ matrix will be orthogonal with elements satisfying,

$$\sum_g C_g^i C_g^j = \delta_{i,j} \quad \text{and} \quad \sum_j C_g^j C_{g'}^j = \delta_{g,g'} \quad . \tag{2.13}$$

Thus by inverting equation 2.12, we obtain $\underline{\psi} = \underline{C}^{-1}\underline{\phi}_g(0) = \hat{\underline{C}}\ \underline{\phi}_g(0)$. Now by choosing the normalization conditions ($\phi_o(0) = 1$, $\phi_g(0) = 0$, $\phi_h(0) = 0$, ...) it immediately follows that

$$\psi^i = C_o^i \quad .$$

Substituting $\underline{\psi} = \underline{C}^{-1}\underline{\phi}_g(0)$ into equation 2.11, we get,

$$\underline{\phi}_g(z) = \underline{C}\{\exp\ 2\pi i\gamma^i z\}C^{-1}\ \underline{\phi}_g(0) \quad . \tag{2.14}$$

Equation 2.14 expresses the diffracted beam amplitudes at a depth z in a perfect crystal in terms of $\underline{\phi}_g(0)$ the corresponding values at the top surface. This equation can be written in terms of a scattering matrix, $\underline{P}(z)$, as

$$\underline{\phi}_g(z) = \underline{P}(z)\ \underline{\phi}_g(0)$$

where

$$\underline{P}(z) = \underline{C}\ \{\exp\ 2\pi i\gamma^i z\}\ \underline{C}^{-1} \quad . \tag{2.15}$$

$\underline{P}(z)$, the scattering matrix of the crystal, is a matrix which relates the amplitudes of the different diffracted

beams at any arbitrary depth z in the crystal to the values of those amplitudes at the top surface.

2:3 INCLUDING EFFECTS OF ABSORPTION IN THE DYNAMICAL THEORY

The theory described so far in the previous sections does not take into account the effects due to inelastically scattered electrons. Electrons which are inelastically scattered outside the objective aperture of the microscope do not contribute to the image and can therefore be considered absorbed. The effects of those absorbed electrons were taken into account in the dynamical theory phenomenologically by Hashimoto et.al. [14] through adding imaginary terms iV'_g to the Fourier components V_g of the crystal potential. Yoshioka [60] has given a quantum mechanical justification of this procedure. Later calculations by Yoshioka [61] and Whelan [62] indicated that the most significant contribution to $V'(r)$ usually come from thermal diffuse scattering processes. This new term $V'(\vec{r})$, can be expanded as a Fourier series in the same way as the real lattice potential $V(\vec{r})$, i.e.

$$V'(\vec{r}) = \sum_g V'_g \, e^{2\pi i \vec{g}.\vec{r}} \quad . \tag{2.16}$$

The ratio, V'_g/V_g, which is taken as a measure of the strength of absorption was shown by Hashimoto et.al. [15] and Humphreys and Hirsch [63] to be small for most materials. Thus it is usually adequate to treat the problem of calculating the associated Bloch wave absorption coefficients by using first order perturbation theory. The effect of the perturbation $iV'(r)$ is to change the energy of the Bloch wave by an amount, $e\Delta E$, given by

$$e\Delta E = -i \int b^{*i} V'(r)\, b^i \, d\tau \quad . \tag{2.17}$$

This energy change can be related to a change Δk_z^i in the z-component of the Bloch wave vector k^i by,

$$\Delta k_z^i = - \frac{me}{h^2 k_z^i} \Delta E \quad .$$

$$= - i\, q^i \quad . \tag{2.18}$$

The absorption coefficient q^i of Bloch wave b^i can therefore be obtained by evaluating the integral 2.17 to give

$$q^i = \frac{1}{2K} \sum_g \sum_{g'} C_g^i C_{g'}^i U'_{g-g'} \quad . \tag{2.19}$$

Including the effects of absorption in the theory involves simply replacing each eigen value γ^i by $(\gamma^i + iq^i)$, with q^i calculated from equation 2.19.

2:4 PHYSICAL ORIGINS OF ABSORPTION, AND THE EFFECTS OF INELASTIC SCATTERING ON TRANSMISSION ELECTRON IMAGES

There are three important physical processes which can give rise to inelastic scattering. These are plasmon scattering, electron-electron interaction and phonon or thermal diffuse scattering.

Thermal diffuse scattering involves very small energy losses, but scattering angles are moderately large. The contribution of this type of energy loss is of prime importance to electron absorption, since in general most electrons suffering this type of loss will not enter the objective aperture, and are therefore considered to be absorbed. The effects of thermal diffuse scattering are likely to be smaller when the crystal temperature is lowered. This, in fact, has been experimentally observed by Steeds and Valdre [64], and Howie and Valdre [65], who found that electron penetration can increase from two to three times by going from room to liquid helium temperatures.

Plasmon scattering, on the other hand, occurs when the high energy electrons excite collective plasma oscillations in the valence electron gas as a whole. The mean free paths for plasmon excitation lie typically [66] in the range 1000-5000 A° for 100 kV electrons, so that in many cases almost all electrons emerging from the

crystal have lost energy. The plasmon wave length is long compared with lattice spacing (i.e. the wave vector $q << g$) and it is not expected therefore that the Bragg reflection would occur during plasmon excitation. Only small angle scattering is therefore expected and most electrons suffering this kind of loss will therefore pass through the objective aperture.

The third type of energy loss namely electron-electron scattering involves short range interaction with the valence or core electrons of individual atoms. Most of the electrons suffering this type of energy loss also pass through the objective aperture of the microscope [60 to 62].

The effects on image contrast of the inelastically scattered electrons passing through the objective aperture are not taken into account by the procedure outlined in section 2:3. Howie [67], however, has studied the effects of those electrons on the resulting images. His conclusions were that small angle inelastic scattering gives rise to contrast effects very similar to that of elastically scattered electrons. These effects had been observed experimentally by Kamiya and Uyeda [68] who displaced the objective aperture in a manner such that only inelastically scattered electrons contributed to the image. Their results showed that images very

similar to those obtained with elastically scattered electrons resulted. The work of Yoshioka [60, 61], Whelan [62] and Humphreys and Whelan [69] has also shown that contrast preservation results from electron-electron scattering processes.

2:5 CALCULATION OF STACKING FAULT CONTRAST USING THE DYNAMICAL THEORY

2:5.1 CASE OF A STACKING FAULT PARALLEL TO BOTH CRYSTAL SURFACES

Matrix methods have been applied to crystals containing stacking faults by Howie and Whelan [59]. The situation is illustrated in Fig. 3 which shows a composite crystal made up of two slabs of thicknesses t_1 and t_2, of similar lattice orientation but with a relative displacement $\vec{R}$ due to the stacking fault. The waves transmitted through such faulted crystal are found by allowing the waves $\phi_o(t_1)$, $\phi_g(t_1)$ ... leaving slab 1 to be scattered again by slab 2. In terms of the scattering matrix notation, this means that we must multiply (in the correct order) the scattering matrices of the individual slabs of thicknesses t_1 and t_2, as

$$\underline{\phi}_g(t) = \underline{P}(t_2)\ \underline{\phi}_g(t_1)$$
$$= \underline{P}(t_2)\ \underline{P}(t_1)\ \underline{\phi}_g(0) \quad . \qquad (2.20)$$

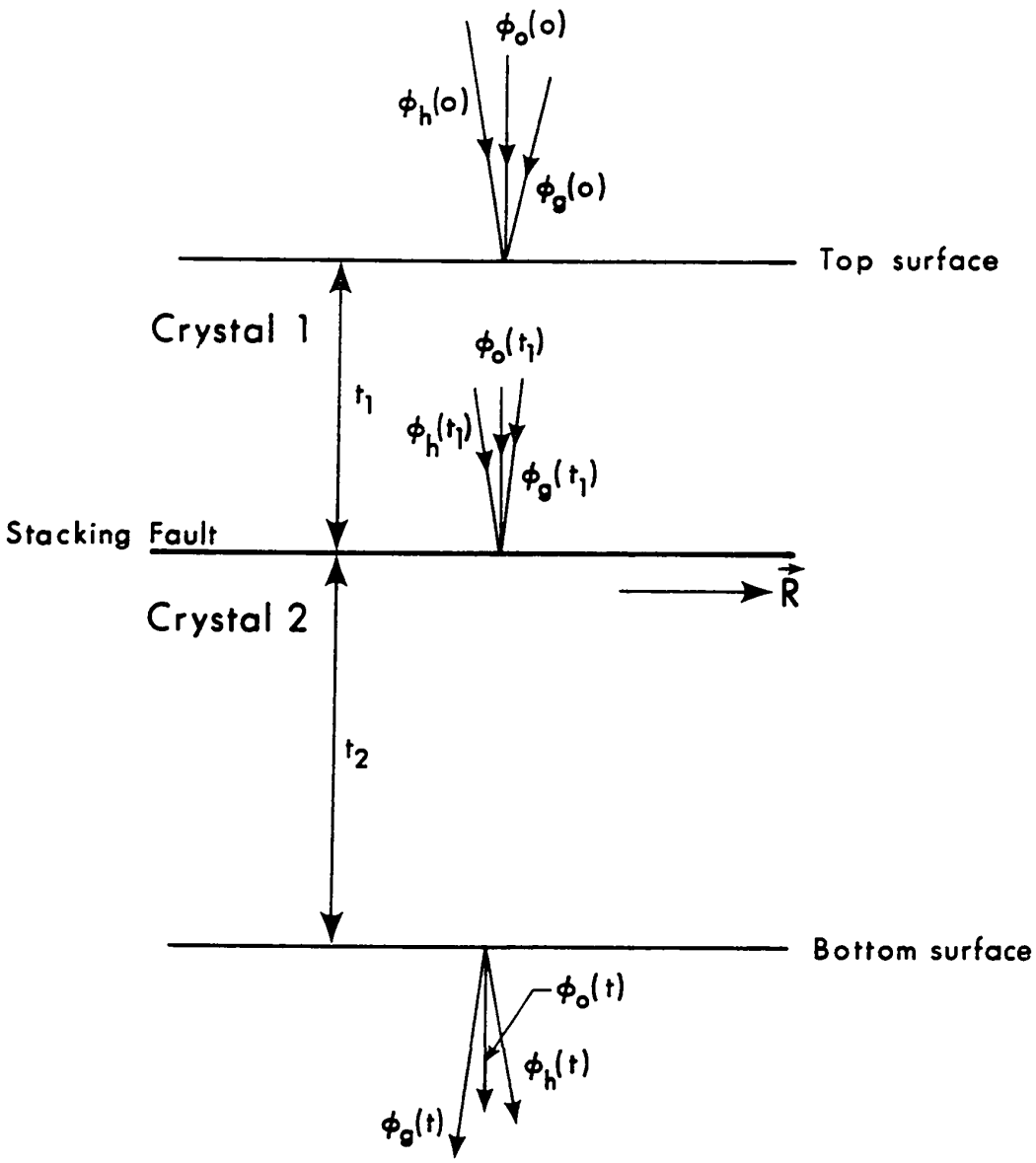

Fig. 3 A crystal containing a stacking fault at a depth t_1 parallel to both surfaces of the crystal. $\vec{R}$ is the displacement vector of the fault.

For the upper portion of the crystal, the amplitudes of the different diffracted waves incident on the fault are the same as for a perfect crystal of thickness t_1, where scattering matrix $\underline{P}(t_1)$ is given by $\underline{P}(t_1) = \underline{C}\{\exp 2\pi i\gamma^i t_1\}\underline{C}^{-1}$. The question which arises now is how to calculate $\underline{P}(t_2)$ of the lower slab. The effect of the displacement of the lower crystal is to cause terms containing C_g^i to be multiplied by a phase factor given by exp - $2\pi i\vec{g}.\vec{R}$. The reason for this can be seen from Schrodinger equation where the potential energy for the upper crystal can be written as,

$$V_1 = V_o + \sum_g{}' \, (V_g)_1 \, e^{2\pi i\vec{g}.\vec{r}} \quad ,$$

and for lower crystal as,

$$V_2 = V_o + \sum_g{}' \, (V_g)_2 \, \exp 2\pi i(\vec{g}+\vec{R}).\vec{r} \quad .$$

Thus

$$(V_g)_2 = (V_g)_1 \, e^{-2\pi i\vec{g}.\vec{R}} \quad .$$

This last equation is merely restating the fact that for any point $\vec{r}$ in the lower crystal, the potential is the same as that of the upper crystal for an atom at a position $(\vec{r}-\vec{R})$. The expression for a Bloch wave in the lower part of the crystal will accordingly be,

$$\sum_g C_g(k^i) e^{2\pi i(\vec{k}^i+\vec{g}).(\vec{r}-\vec{R})} = e^{-2\pi i\vec{k}.\vec{R}} \sum_g C_g(\vec{k}^i) e^{-2\pi i\vec{g}.\vec{R}} \times$$

$$e^{2\pi i(\vec{k}^i+\vec{g}).\vec{r}} \quad .$$

The phase term, $\exp - 2\pi i\vec{k}^i.\vec{R}$, can in fact be ignored, since it is independent of $\vec{g}$. Therefore, the displacement $\vec{R}$ will also cause phase changes in the off-diagonal elements of the matrix $\underline{A}$ of equation 2.6 and corresponding changes in the scattering matrix $\underline{P}$. The off-diagonal elements of $\underline{A}$ will behave the same as U_h and will therefore become $U_h\, e^{-2\pi i\vec{h}.\vec{R}}$. The effects of the displacement $\vec{R}$ of the lower crystal can conveniently be expressed by defining a matrix $\underline{Q}$ given as

$$\underline{Q} = \{\exp\ 2\pi i\vec{g}.\vec{R}\}$$

where the curly bracket indicates a diagonal matrix. The matrix $\underline{A}$ thus becomes $\underline{Q}^{-1}\underline{A}\underline{Q}$ in the lower part of the crystal and the matrix $\underline{P}$ becomes $\underline{Q}^{-1}\underline{P}\underline{Q}$, i.e.

$$\underline{P}(t_2) = \underline{Q}^{-1}\ \underline{C}\ \{\exp\ 2\pi i\gamma^i t_2\}\underline{C}^{-1}\ \underline{Q} \quad . \qquad (2.22)$$

The amplitudes of the diffracted beams at the bottom surfaces of the faulted crystal can now be written as,

$$\underline{\phi}_g(t) = \underline{Q}^{-1}\underline{C}\{\exp\ 2\pi i\gamma^i t_2\}\underline{C}^{-1}\,\underline{Q}\,\underline{C}\{\exp\ 2\pi i\gamma^i t_1\}\underline{C}^{-1}\underline{\phi}_g(0) \quad .$$

(2.23)

Effects of absorption can be included in the usual way in equation 2.23, by replacing the eigen values γ^i by $(\gamma^i + iq^i)$.

2:5.2 THE CASE OF A FAULT INCLINED TO BOTH CRYSTAL SURFACES

Image contrast from a crystal containing a stacking fault can only be observed when the fault is inclined to the surfaces of the crystal. Equation 2.23 shows that if the fault lies at a constant depth t_1, the intensity of the diffracted beams at the bottom surface will remain constant and consequently no contrast result. It is clear therefore that image contrast can only occur when t_1 varies, i.e. for the case of an inclined fault.

The calculation of image contrast from an inclined stacking fault requires detailed wave matching of the electron wave function at the fault plane, which obviously will involve the inclination angle of the fault to the crystal surfaces. The work of Whelan and Hirsch [12] has shown, however, that for angles up to 80°, image contrast can be described to a good approximation, by varying the fault depth t_1 in 2.23. This approximation assumes, as in Fig. 4b, that each point on the inclined fault can be considered to correspond to a

stacking fault at the same depth but lying parallel to both surfaces of the crystal. It is important at this stage to examine this approximation as presented by Whelan and Hirsch [12].

Consider a crystal containing an inclined stacking fault, and let $\vec{n}_F$ in Fig. 4a be in a direction normal to the fault plane and n be the normal to the crystal. In the upper part of the crystal the incident electron beam excites two Bloch waves corresponding to the wave points D^1 and D^2. These wave points are determined by the intersection of the normal $\vec{n}$ to the top surface of the crystal with the two branches of the dispersion surface. When a Bloch wave encounters the stacking fault correct wave matching, which ensures the continuity of the tangential components of Bloch wave vector across the fault plane (see Whelan and Hirsch [12]), requires the excitation of additional wave points D^i, D'^i. The additional wave points are determined from the intersection of the normal of the fault $\vec{n}_F$, with the two branches of the dispersion surface.

In order that image contrast for an inclined fault be described by equation 2.23, the values of the relevant Bloch wave parameters C_g^i and γ^i for wave points D^i and D'^i must be equal to a good approximation. This situation can only be achieved when the separation, Δy, of these wave points is quite small. The separation Δy,

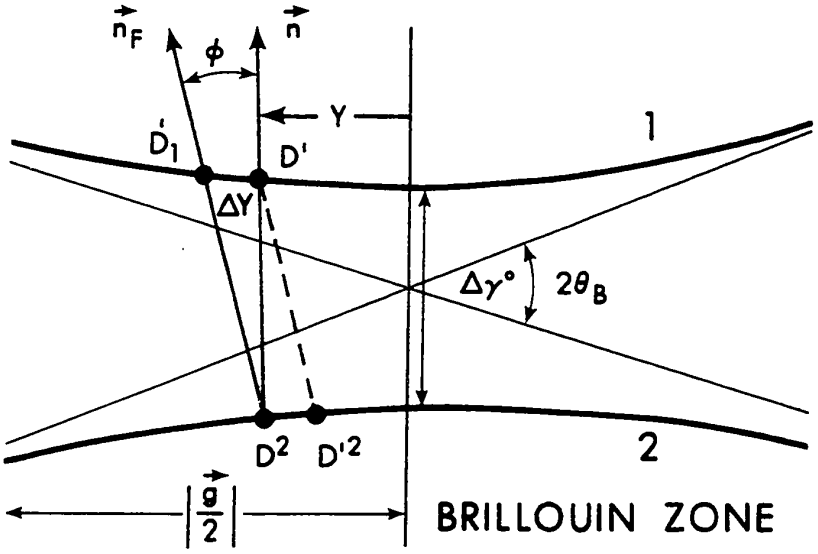

Fig. 4a Two beam dispersion surface for a crystal containing a stacking fault.

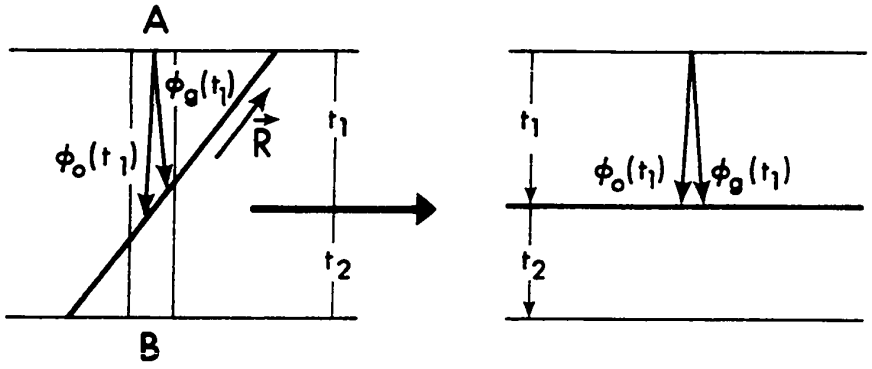

Fig. 4b The portion of the stacking fault in the narrow column AB (left) is equivalent in the column approximation to a stacking fault lying at the same depth but parallel to the surfaces of the crystal (right).

of D^1 and D'^1 can be seen from the geometry of Fig.4a to be

$$\Delta y = \Delta\gamma \tan \phi \qquad (2.24)$$

where, ϕ, is the angle of slope of the fault, and $\Delta\gamma$ is the wave vector difference D^1D^2. Equation 2.4 can be rewritten in the form

$$\Delta y = f(\Delta\theta)\ \Delta\gamma_o \tan \phi \qquad (2.25)$$

$\Delta\gamma_o$ in equation 2.25 is the value of $\Delta\gamma$ when the exact Bragg condition is satisfied, and $f(\Delta\theta)$ is the function which relates $\Delta\gamma$ and $\Delta\gamma_o$ (The exact form of this function is not required for the purposes of the present argument). From the geometry of Fig. 4a, $\Delta\gamma_o = |\vec{g}| \tan \theta_B$ where θ_B is the Bragg angle, and the separation Δy becomes,

$$\Delta y = f(\Delta\theta)\ |\vec{g}|\ \tan \theta_B \tan \phi\ . \qquad (2.26)$$

In practice the Bragg angles are quite small ($\theta_B \sim 10^{-2}$ radians) indicating that the value of Δy in equation 2.26 is very close to zero, as long as the angle ϕ is not too close to $\pi/2$. Therefore, if the fault is not too steeply inclined to crystal surfaces, the additional wave points D'^i can, to a very good approximation, be considered to coincide with the corresponding wave points

D^i. This approximation allows therefore the use of equation 2.23 in calculation of image contrast from a sloping fault.

The approximation involved in the above discussion is commonly referred to as the column approximation. Fig. 4b illustrates the nature of this approximation as applied to the case of the stacking fault. In order to obtain the diffracted beam amplitudes $\phi_o(t_1)$, $\phi_g(t_1)$,.. a narrow column of crystal AB is considered. The calculation is carried out by assuming that the stacking fault in the column AB is parallel to both the crystal surfaces, permitting the approach discussed in the previous paragraph to be used. The column approximation gives accurate results in electron diffraction, mainly because the Bragg angles are very small. Thus the fan included by direct and diffracted rays emanating from point A on the top surface (see Fig. 4b) is very slender, and such rays essentially sample a portion of the stacking fault which, to a good approximation, lies in a plane parallel to both surfaces of the crystal. It can be seen from Fig. 4b that the column approximation will obviously be better when the inclination of the fault in the crystal decreases.

In the previous paragraph, the column approximation as it applies to two beam calculations of stacking

fault contrast was discussed. The multibeam case however is somewhat different. In this case the curvature of higher order branches of the dispersion surface is considerably more than that of the upper most two branches considered preceedingly in this section. Accordingly the relative change in the values of C_g^i and γ^i between wave points D^i and D'^i will be expected to be higher for those branches, and consequently more serious errors might result by making the column approximation. The work of Howie and Basinski [70] has shown however, that the errors introduced by making the column approximation in the multibeam case are small.

2:6 STACKING FAULT CONTRAST IN TERMS OF BLOCH WAVE INTERACTIONS

Some physical insight into the mechanisms producing contrast can be obtained by considering the dispersion surface representation of the dynamical theory for a crystal containing a stacking fault. In this section, an account will be given of the method originally used by Hirsch et.al. [71] to describe fault contrast in the two beam theory in terms of Bloch wave interactions. The multibeam expressions which allow the extension of this analysis to the case when more than two Bloch waves are important have not been previously derived and are

presented in Chapter 4 of this thesis.

In order to examine stacking fault contrast in terms of Bloch wave interactions, Hirsch et.al. [71] considered the relationship between the excitation coefficients ψ^1 above and below the fault. They found that

$$\psi_1^1 = (C_o^{1^2} + C_g^{1^2}\ e^{i\alpha})\psi^1 + C_o^1 C_o^2 (1 - e^{i\alpha}) e^{2\pi i \Delta\gamma t_1}\ e^{-2\pi \Delta q t_1}\ \psi^2$$

and

$$\psi_1^2 = (C_o^{2^2} + C_g^{2^2}\ e^{i\alpha})\psi^2 + C_o^1 C_o^2 (1 - e^{i\alpha}) e^{-2\pi i \Delta\gamma t_1}\ e^{i\pi \Delta q t_1}\ \psi^1 \qquad (2.27)$$

where ψ_1^i represent the excitation amplitudes below the fault, $\Delta\gamma = \gamma^1 - \gamma^2$, $\Delta q = q^1 - q^2$, and t_1 is the depth of the fault in the crystal. The above equations show that the values of ψ_1^i (i=1,2) below the fault depend on the amplitude of the same Bloch wave above the fault, interpreted as intrabranch scattering, as well as the amplitude of the other Bloch wave above the fault, interpreted as interbranch scattering. In the original terminology of Hirsch et.al. [71] these two processes were referred to as interband and intraband scattering. However, since transitions occur between the Bloch waves associated with different branches of the dispersion surfaces, it is thought that a more accurate description

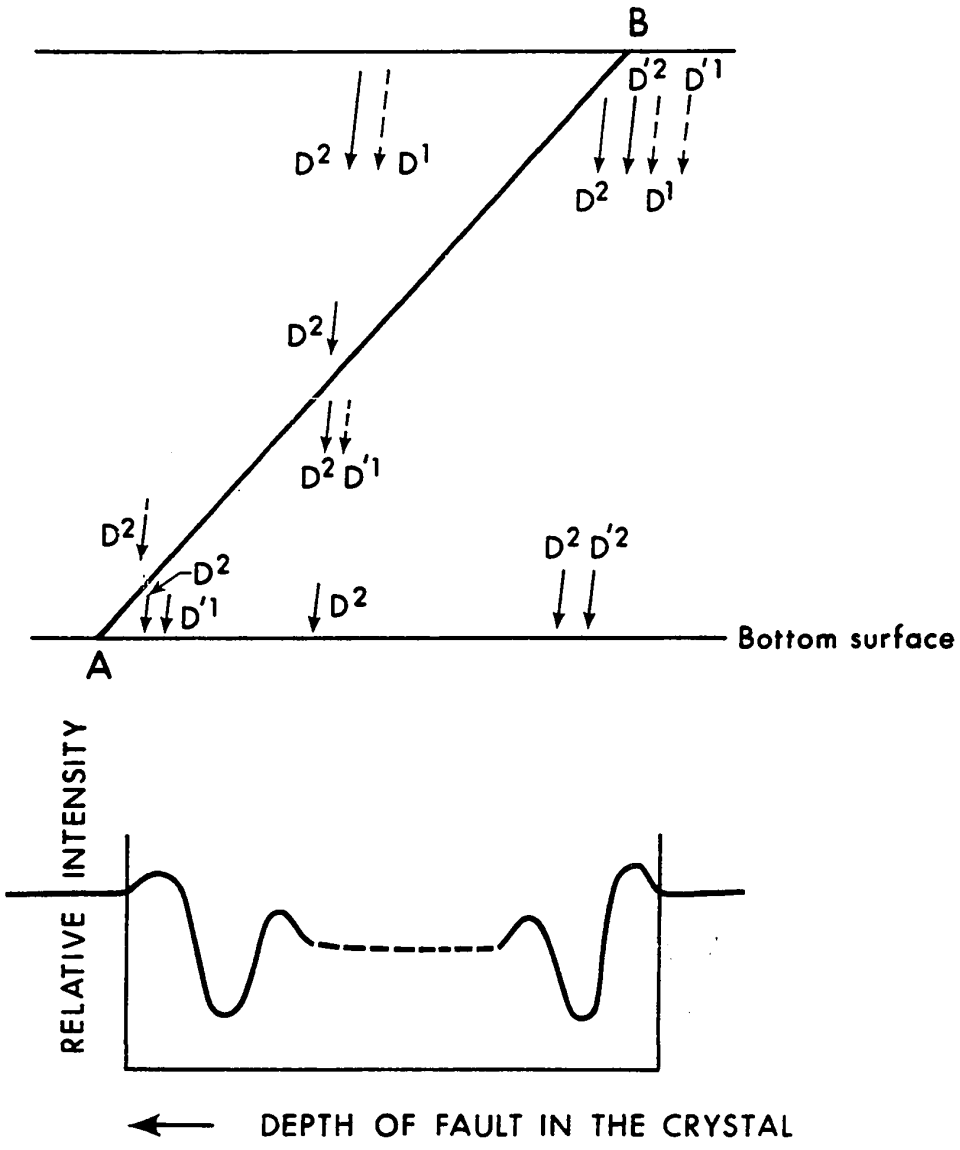

Fig. 5 Analysis of image contrast from a thick crystal containing a stacking fault in terms of Bloch wave interactions.

of the physical processes involved is given in terms of inter- and intrabranch scattering. The two intrabranch terms appearing in equation 2.27 are,in fact,represented in Fig. 5 by the wave points D^1 and D^2, while the wave points D'^1, D'^2 in Fig. 5 represent interbranch scattering. Stacking fault contrast in this picture arises due to the beating effects between the Bloch waves associated with the different wave points D^1, D'^1, D^2, and D'^2.

It is interesting to discuss in some detail how image contrast was interpreted by Hirsch et.al. [71] for a fault lying in a thick crystal, when the crystal was oriented such that a low order reflection satisfied the exact Bragg condition. Under these conditions the effects of anomalous absorption are most pronounced [15], and a wide difference exists between the absorption coefficients of the two Bloch waves considered (i.e. $q^1 >> q^2$). In region A of Fig. 5 both wave points D^1 and D^2 are excited. Since the Bloch wave associated with the wave point D^1 is heavily absorbed, then for thick regions of the crystal and near the bottom surface, effects due to D^1 can be neglected. This behaviour is indicated by the broken arrows of Fig. 5. In the lower wedge crystal at A interbranch scattering occurs from Bloch wave 2 to Bloch wave 1 and only the wave points D^2 and D'^1 are important. The interference between the Bloch waves

associated with these two wave points will give rise, as shown in Fig. 5, to fringes with periodicity $1/\Delta\gamma$ (i.e., fringes will have the periodicity of the extinction distance).

In thin parts of the upper wedge crystal, and near B both D^1 and D^2 reach the fault, and due to inter- and intrabranch scattering, the four wave points D^1, D'^1, D^2 and D'^2 will be excited below the fault in crystal 2. However, D^1 and D'^1 are characterized by a high value of absorption coefficients, q^1, and thus will be effectively removed by absorption before reaching the bottom surface of the crystal. Fringe contrast in this region therefore arises from the interaction between D^2 and D'^2 and fringe periodicity will be again equal to the extinction distance.

Near the middle of the fault only D^2 reaches the stacking fault. The only scattering which can occur will be an interbranch transition to branch 1 of the dispersion surface, thus exciting the additional wave point D'^1. However, since the latter is heavily absorbed only D^2 reaches the bottom surface giving rise to very weak image contrast.

2:7 CORRECTIONS TO THE DYNAMICAL THEORY

2:7.1 RELATIVISTIC EFFECTS

The dynamical theory so far discussed, neglects relativistic effects, which can amount to about 10% at

100 kV. Fijiwara [72, 73] has developed a relativistic dynamical theory by employing Dirac's equation. His results [73,74] have shown that a non-relativistic theory developed by using Schrodinger equation can be corrected for relativistic effects by:

(i) replacing the non-relativistic wave length by a relativistically corrected one.

(ii) multiplying the Fourier coefficients of the lattice potential by β, with $\beta = (1-v^2/c^2)^{\frac{1}{2}}$ where v and c are the speeds of the electrons and light respectively. This multiplication in fact corrects for the relativistic mass of the electron.

(iii) For the imaginary part of the lattice potential U_g' the correction involves multiplying U_g' by $v^{-1}\beta$ (see Howie [74]).

The validity of these simple substitutions, have in fact been confirmed experimentally by Hashimoto [75], Dupouy et.al. [76], and Goringe et.al. [28].

2:7.2 THERMAL VIBRATION OF ATOMS

Another type of correction which must be considered when employing the dynamical theory is due to the thermal vibration of the atoms. Thermal vibrations can result in an appreciable decrease in the Fourier

coefficients of the lattice potential U_g, since it tends to distort the periodic nature of the crystal potential. Including these effects in the dynamical theory is usually [77,78] accomplished by multiplying U_g by $\exp -D|\vec{g}|^2/4$, where D is the Debye Waller factor and $|\vec{g}|$ is the magnitude of the reciprocal lattice vector $\vec{g}$.

CHAPTER 3

DETAILS OF THE EXPERIMENTAL MEASUREMENTS AND PROFILE CALCULATIONS

The work presented in this thesis explores some of the effects that systematic reflections have on stacking fault images. This has been done by first studying experimentally the dependence of image contrast on crystal thickness and orientation, and then comparing these results to predictions of the dynamical theory. The present chapter is devoted to a discussion of the details of the experimental measurements carried out, as well as calculational details. This has been done by dividing this chapter into three major sections 3:1, 3:2, and 3:3.

Section 3:1 is devoted to a discussion of the experimental conditions under which stacking faults were observed in the electron microscope, and includes details such as the use of tilting stages (section 3:1.3) indexing of diffraction patterns (section 3:1.4), as well as the way in which experimental stacking fault profiles were obtained at different crystal thicknesses and orientation (sections 3:1.5, 3:1.6).

In section 3:2 some details concerning the calculation of theoretical profiles, which were not

explicitly described in Chapter 2 of the theory, are given. Sections 3:2.1, 3:2.2, and 3:2.4 discuss, respectively, the calculation of the deviation parameters S_g for the different reflections in a particular row of systematics, the calculation of Fourier coefficients of crystal potential, and the criterion used to limit the number of reflections to be taken into account in a particular calculation.

Finally, sections 3:3.1 and 3:3.2 of this chapter present the methods used to measure experimentally the values of the absorption parameters for the material concerned. These parameters are required in calculating theoretical stacking fault profiles which take into account effects of absorption, thus allowing a comparison to be made between predictions of the theory and experimental results.

3:1 EXPERIMENTAL DETAILS

3:1.1 TEST MATERIAL

The metal cobalt was chosen as a test material. Pure cobalt undergoes a phase transformation of the matrensitic type [79]. During cooling the high temperature fcc phase undergoes a transformation to the hcp structure at about 417°C. Previous work on cobalt [80 to 82] has shown that the degree of the transformation

was dependent on grain size and prior heat treatment. Thus it is possible, under certain conditions [82] to obtain at room temperature both phases of cobalt. Both the fcc and hcp phases have low stacking fault energies [83,84] with the result that stacking faults can be observed quite frequently in either phase at room temperature. The heat treatment used to stabilize more of the high temperature cubic phase at room temperature, was to anneal the specimen for about 3 hours at 800°C and then to cool it rapidly (~50°C/min) to room temperature.

In the present work 3 mm discs were cut from the annealed sheets using a spark cutting machine. These discs were first polished in a jet polishing arrangement to obtain a dimple shaped specimen, and were then made ready for observation by electrolytic polishing using pointed shaped stainless steel electrodes.

3:1.2 ELECTRON MICROSCOPE EXAMINATION

Experimental observations were carried out in a JEM-150 electron microscope using a tilting-rotating stage. The stage allowed a specimen to be tilted about two mutually perpendicular axes through a range of ±15° and ±5° respectively. The specimen could also be rotated through 360°. In order to facilitate tilting through a known angle, a high precision click-type

control was used which allowed angle changes to be made in increments of 0.005°.

3:1.3 DETERMINATION OF TILT AXIS DIRECTION AND TILT CALIBRATION

In actual observations of stacking fault contrast as function of angle of tilt, the specimen must be tilted about an axis perpendicular to the row of systematic reflections chosen. Thus the set of crystal planes involved must be oriented in the direction of the one of the tilting axes of the stage. Under these conditions a given change in the angle of tilt of the specimen results in an equal change in the value of $\delta\theta_g$ the deviation of a reflection, g, from the exact Bragg condition. However, in order to orient the specimen in this manner the direction of the axis of tilt, as seen on the viewing screen, had to be determined. This was done by using the fact that, as the specimen is tilted, the associated Kikutchi pattern must move in a direction perpendicular to the tilt axis. The direction of motion of the Kikutchi pattern was determined from a series of diffraction patterns of the specimen taken as it was being tilted. This method permitted the direction of the tilt axes as seen on the screen to be determined to an accuracy of ±3°.

The specimen tilt system was also checked for both long range errors, which might change the average increment of tilt from the designed value of 0.005°, and short range errors which might result from the random variation of this increment. In an actual check the specimen was oriented so that a row of systematic reflections was perpendicular to the tilt axis direction. The specimen was then tilted from an orientation in which the reflection, g, was in the exact Bragg condition to one in which the reflection, -g, satisfied the Bragg condition. The exact Bragg orientation was determined from the fact that a bright Kikutchi line must pass through the middle of the spot concerned. Tilting the specimen in this manner results in an orientation change equal to twice the Bragg angle of the g^{th} reflection. This angle was calculated from Bragg's law and then compared to the corresponding angle as read from tilt control. It was found that the angles given by tilt control were accurate to 1%.

The short range random variations in increment were checked by using a method suggested by Sheinin [85]. In general they were found to be within 10% of the increment size. However, these variations usually occurred in pairs in a manner such that the average increment was still approximately 0.005°.

The accuracy of rotation control was not checked except for smoothness since precise rotations of the specimens were not required.

3:1.4 IDENTIFICATION OF COBALT PHASE AND INDEXING OF DIFFRACTION SPOTS

In order to correctly interpret a particular stacking fault image, it is important to know the type of cobalt phase in which the fault is lying and also to correctly determine the orientation from the resulting diffraction pattern. The procedure adopted for an accurate determination of these two parameters was as follows:

(1) The camera constant λL was determined by using a standard gold specimen.

(2) Using a model for the reciprocal space of both fcc and hcp lattices, the spacings, ξ, of the different possible diffraction spots from the directly transmitted beam were calculated. For each reciprocal lattice section 3 non-collinear reflections (000), $(h_1k_1l_1)$, $(h_2k_2l_2)$ were chosen and the ratios of their distances ξ_1/ξ_2 , ξ_1/ξ_3 and ξ_2/ξ_3 were then calculated.

(3) Experimentally by using both tilt controls plus rotation if necessary, a symmetrical diffraction pattern from the area concerned was recorded.

From such micrographs the experimental values of ξ_1, ξ_2 and ξ_3 were measured and the ratios were calculated. These were then compared to the theoretical values. Using the procedure outlined above it was always possible to index the diffraction pattern and identify the crystal structure of the area concerned. It is interesting to mention that in some instances an easier method for determining crystal structure was used. This involved the detection of magnetic domains. Due to the anisotropy of the hcp structure of cobalt a direction of easy magnitization exists [86,87]. Thus if in a hexagaonal grain the direction of easy magnetization [0001] has a resolved component in a direction parallel to the bottom surface of the crystal, magnetic domains will be visible. The observation of these domains offered a quick method of determining whether or not the area considered was hcp.

3:1.5 PROCEDURES ADOPTED FOR OBSERVING STACKING FAULTS

After indexing the diffraction pattern, the particular row of systematics chosen was made to coincide with one of the tilting axes of the stage. The rotation control was usually used to achieve this situation. Next, the specimen was tilted about that axis, until the non-systematic reflections (i.e. reflections which

are not collinear with the row of reflections chosen) were as far as possible from satisfying their Bragg conditions. Caution was also taken to ensure that none of the second zone spots which occur due to the finite curvature of the Ewald sphere were close to satisfying their Bragg orientations. It is important to mention, however, that in some instances the above requirements needed to minimize the effects of non-systematic reflections could not be met experimentally. When this was the case no attempt was made to carry out observations of stacking faults.

The next step, after tilting non-systematic reflections to orientations where their effects were expected to be minimal, was to orient the specimen so that the desired value of S_g was obtained. The procedure adopted to do this was first to determine the number of clicks on the tilt control corresponding to one Bragg angle, and then to calculate the number of clicks necessary to tilt the crystal to the required value of $\delta\theta_g$. Thus for example when the desired orientation was between the reflection 2g and 3g, the crystal was tilted initially to the exact Bragg condition of the reflection 3g as judged by the Kikutchi line passing through the middle of the reflection. Then the tilt control was utilized to tilt through the number of clicks corresponding to one half of a Bragg angle.

Dark field observations of stacking fault images were carried out by tilting the illumination system of the microscope so that the diffracted beam concerned was parallel to the axis of the microscope. This procedure was adopted so that the image considered would be subjected to minimum spherical abberation.

3:1.6 DETERMINATION OF EXPERIMENTAL STACKING FAULT PROFILES AT DIFFERENT CRYSTAL THICKNESSES

Stacking fault contrast was studied as function of crystal thickness by comparing experimental profiles recorded at different crystal thicknesses. The question which arises is how to specify the value of crystal thickness for which a particular profile is recorded. One way this can be done is through the determination of the absolute value of crystal thickness, which involves a knowledge of the wedge angle as well as the distance perpendicular to the edge of the specimen to the point where the trace was recorded. This procedure is generally quite difficult since in most cases the wedge angle of the crystal cannot be accurately determined. An alternative method which was adopted in the present work was to specify the crystal thickness in terms of the extinction distance. This procedure involves obtaining stacking fault profiles at points where the intensity of the associated thickness fringes can be accurately defined. The positions

which were found most convenient correspond to crystal thicknesses of n and (n+½) extinction distances where n is an integer. At these values of crystal thickness, thickness fringes exhibit either intensity maxima or minima.

The manner in which actual profiles were recorded from a micrograph like that given in Fig. 6 was as follows: The micrograph was placed on the stage of a microdensitometer and was aligned so that the direction of thickness contours appearing at both sides of the stacking fault image, were as far as possible in the direction in which the trace was taken. The plate was advanced until the tracing direction coincided with a position of a maximum in directly transmitted intensity. Tracing the image in this way gave an experimental stacking fault profile corresponding to a fault in a crystal of thickness n extinction distances where n is known. The next trace was recorded by advancing the plate through a distance corresponding to half the extinction distance, and so on.

The important question which arises when carrying out theoretical calculations of stacking fault profiles, which are to be compared to the experimental traces, is what are the values of crystal thickness at which the calculations should be performed. In investigations

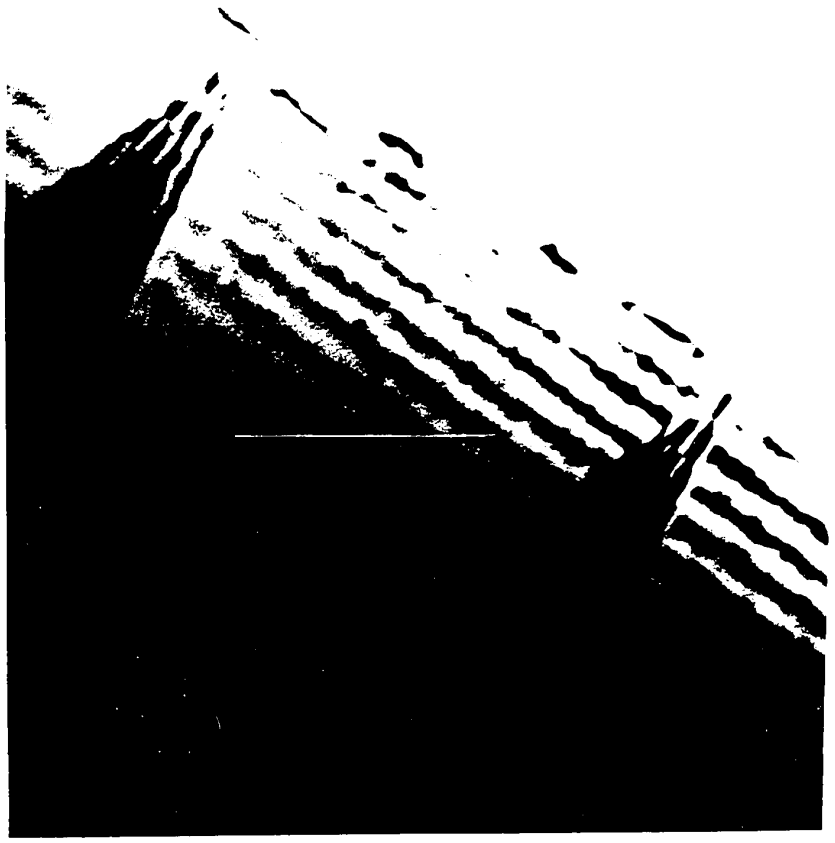

Fig. 6 Micrograph showing bright field image of stacking faults in wedge crystal of fcc cobalt. Experimental profiles such as those in Figs. 10, 14 were obtained by taking microdensitomer traces in a direction parallel to the extinction contours.

carried out in the past [29,34] the appropriate value of crystal thickness was obtained by defining the extinction distance, as in the two beam theory, by $1/\gamma^1-\gamma^2$, i.e. the reciprocal separation of the two uppermost branches of the dispersion surface. There are two reasons why this definition of extinction distance, can in fact, lead to serious errors in determining crystal thickness at which stacking fault calculations are to be carried out. The first reason is due to possible variations in the peak-to-peak spacing in actual multibeam extinction contour plots from the value $1/\gamma^1-\gamma^2$. These variations occur because of the presence of Bloch waves other than one and two (For more details on this point see section 5:1). The other reason is that, under certain circumstances eigen values other than γ^1, γ^2 can determine the extinction distance. Therefore the approach adopted in the present work was to determine values of crystal thickness in a manner quite analogous to the way in which experimental profiles were recorded. The method was to calculate a theoretical extinction contour profile for the same diffraction conditions under which the experimental images were recorded. From such intensity plots the crystal thicknesses corresponding to positions of intensity maxima and minima were then determined. Stacking fault profiles were then calculated using these values

of crystal thickness.

3:2 DETAILS OF PROFILE CALCULATIONS

The calculation of theoretical intensity profiles was carried out by using the scattering matrix approach of the dynamical theory as outlined in Chapter 2. In order to calculate diffracted beam intensities, the Bloch wave parameters C_g^i and γ^i must be known. These were obtained by solving the eigen value relation of equation 2.6. Therefore the starting point in a particular calculation involved setting up the input matrix $\underline{A}$. If n systematic reflections are to be included in a calculation, the $\underline{A}$ matrix will be an $n \times n$ matrix. The diagonal elements are the deviation parameters S_g of the different reflections in a systematic set (see section 2:1.1), and the off-diagonal elements are given by $A_{gh} = U_{g-h}/2K$. The manner in which these two parameters were calculated is considered next.

3:2.1 CALCULATION OF S_g FOR THE CASE OF SYSTEMATIC REFLECTIONS

The vector, $\vec{S}_g$, which represents the deviation of a particular reflection, g, from its Bragg condition can be calculated from the relation $S_g = |\vec{g}|\delta\theta_g$, where $\delta\theta_g$ is the deviation angle of the reflection g from

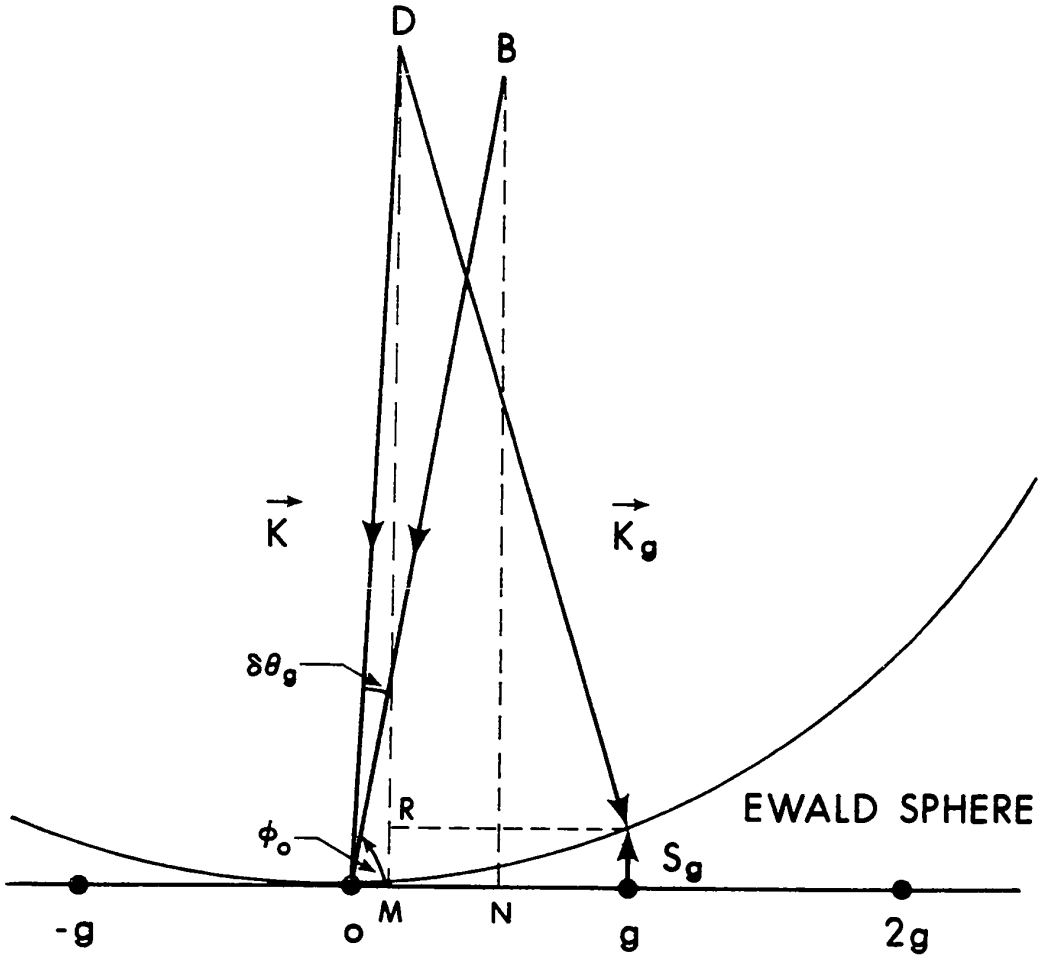

Fig. 7 The Ewald sphere construction showing the deviation parameter S_g for the reflection g in a systematic set. S_g = DM - DR, since

$$DM = (K^2 - K^2\cos^2\phi)^{\frac{1}{2}}$$

and

$$DR = (K_g^2 - \{g - K\cos\phi\}^2)^{\frac{1}{2}},$$

the value of S_g will be given by equation 3.2.

satisfying the exact Bragg angle. This relationship assumes that the Ewald sphere can be considered to be a plane in reciprocal space, and therefore neglects the finite curvature of that sphere. In the calculations presented in this thesis, this curvature was taken into account since for large deviations from the Bragg conditions the approximation $|g|\delta\theta_g$ can lead to serious errors. The manner in which this was done can be understood by considering Fig. 7. The vector $\overrightarrow{BO}$ in that figure represents the incident electron beam $\vec{K}$ when the lowest order reflection $\vec{g}$ of a systematic set satisfies the exact Bragg condition. Under these conditions $S_g = 0$ and the angle between the directions $\vec{K}$ and $\vec{g}$ is given by

$$\cos \phi_o = -\vec{K}.\vec{g}/|\vec{K}|\ |\vec{g}| \quad . \tag{3.1}$$

The vector $\overrightarrow{DO}$, on the other hand, represents the situation at a deviated orientation. The angle $\phi(\vec{K},\vec{g})$ at this new orientation is $\phi = (\phi_o + \delta\theta_g)$, and the deviation parameter can be calculated by using,

$$S_g = |\vec{K}|\{(1-\cos^2\phi)^{\frac{1}{2}} - (1-(|\vec{g}|/|\vec{K}| - \cos\phi)^2)^{\frac{1}{2}}\} \quad . \tag{3.2}$$

Equation 3.2 was used to calculate the deviation parameters of all the reflections considered in a systematic set. However, it can be seen that for small enough

deviations from the Bragg condition the use of equation 3.2 can lead to numerical errors, since it involves taking the differences between the square roots of two large and nearly equal quantities. Under these conditions it can be shown that if equation 3.2 is expanded in a series and if higher order terms are neglected S_g becomes very nearly equal to $|\vec{g}|\delta\theta_g$. This was the relation used to calculate S_g when a reflection was quite close to its Bragg condition.

3:2.2 CALCULATION OF THE FOURIER COEFFICIENTS OF THE LATTICE POTENTIAL

The potential that the high energy electron sees while travelling through a crystal is derived from the charge density at the atomic positions. Thus by expressing both the crystal potential $V(\vec{r})$ and the charge density $\rho(\vec{r})$ in a Fourier sum of the form given in equation 2.1, and then relating these two quantities through Poisson's equation, it is possible to show that the Fourier coefficient U_{g-h} of the crystal potential is written as

$$U_{g-h} = \frac{\beta}{\pi V_c} e^{-\frac{D}{4}|\vec{g}-\vec{h}|^2} F_{g-h} f_e[\frac{\sin\theta(g-h)}{\lambda}] \qquad (3.3)$$

where V_c is the volume of the unit cell, F_{g-h} is the

kinematical structure factor, and $f_e[\sin \theta_{(g-h)}/\lambda]$ is the atomic scattering factor for electrons [77]. Ibers [88], Vanshtein and Ibers [89], and Ibers and Vanshtein [90] have published values for these atomic scattering factors, for specific values of $(\sin \theta/\lambda)$, and for elements with atomic number in the range (1-18) and (20-104). However, in view of the importance of this quantity in electron diffraction analyses, Smith and Burge [91] expressed $f_e(\sin \theta/\lambda)$ for each element in terms of a single analytical expression of the form

$$f_e(x) = \sum_i A^i e^{-B^i x^2} \qquad (3.4)$$

where $x = (\sin \theta/\lambda)$. In their calculations which involved using Thomas-Fermi-Dirac atomic wave functions, Smith and Burge [91] have considered three terms in the above equation. Doyle and Turner [92] using an expression of the same form recalculated the electron scattering factors by employing relativistic Hartree-Fock atomic wave functions. In their calculations they found it necessary to include four terms in the summation of equation 3.4.

The calculation of U_g in the present work employed equation 3.3. Either Smith and Burge or Doyle and Turner parameters were used. It was found that image profiles obtained by using either set of parameters were almost

identical for all cases checked. The appropriate value of the Debye Waller factor D was also used in these calculations in order to include the effects due to thermal vibrations of atoms.

3:2.3 EIGEN VALUES AND EIGEN VECTORS

The next step after calculating the elements of the matrix $\underline{A}$ was to apply a standard diagonalization procedure in order to obtain its eigen values and eigen vectors of equation 2.6. There are four programs available for diagonalizing a real and symmetric matrix in the Computing Centre at the University of Alberta. These programs employed either the Jacobi [93] or Householder [94] methods of matrix diagonalization. A comparison was made of the speed and accuracy of those available routines. In the present work the subroutine Eigen [95] which employs the Jacobi [93] method was chosen since it was found most accurate. The diagonalized matrix contained the eigen values γ^i (i=1,2,..,n) arranged in order of decreasing Bloch wave vector, i.e.

$$|k_z^1| \geq |k_z^2| \geq |k_z^3| \quad \ldots\ldots \text{ etc.}$$

This Bloch wave numbering system is similar to the one proposed by Humphreys and Fisher [96] for electron diffraction which considers only systematic reflection to be excited.

3:2.4 NUMBER OF SYSTEMATIC REFLECTIONS INCLUDED IN THE CALCULATIONS

One question which arises when performing multi-beam calculations of intensity profiles is that of how many reflections should be included. In view of the fact that the computing time required for a particular calculation increases considerably with the number of reflections taken into account it was necessary to develop a criterion which selects only those beams which are relevant to the results obtained. In previous investigations this was done by selecting some image property and increasing the number of beams taken into account until the variation in the value of the quantity chosen became quite small. Metherell and Fisher [97], for example, chose the convergence in the values of Bloch wave parameters C_g^i, γ^i and q^i while Serneels and Gevers [98] chose the convergence in the value of the multibeam extinction distance. Since the present investigation was mainly concerned with image contrast, the detailed shapes of the theoretical profiles were taken to be the important factor. The procedure was to increase gradually the number of reflections included until a stage was reached where the addition of further reflections did not change in any significant way the details in the intensity plots. In most cases the number of systematic reflections which had to be considered was in the range 11 to 15.

3:3 MEASUREMENTS OF ABSORPTION PARAMETERS

Absorption is taken into account in the dynamical theory by assuming an imaginary part for the lattice potential. (See section 2:3 of Chapter 2). The relation between complex and real parts of the lattice potential is normally expressed as

$$N_g = V_g'/V_g \quad .$$

The effects of image contrast arising from the coefficient N_o, associated with the mean lattice potential is referred to as normal absorption. The higher order parameters, N_g, will in general result in Bloch waves having different values of absorption coefficients q^i (see equation 2.19 of Chapter 2). The effects of these Bloch waves on image constrast is commonly known as anomalous absorption. The anomalous absorption parameters, N_g, have been determined theoretically by Humphreys and Hirsch [63] who showed that, to a good approximation, the value of N_g varies linearly with g. The method used by most investigators for determining these parameters experimentally is based on the two beam approximation of the dynamical theory [99]. This method suffers from two major sources of error. The first of these is associated with the effects of systematic reflections, while the second is due to inelastically scattered electrons which pass

through the objective aperture. The fact that systematic reflections have an effect on the values of the absorption parameters measured by the two-beam method was first illustrated by the results of Uyeda et.al. [78]. These authors measured values of absorption parameters in MgO as a function of accelerating voltage and found a marked departure from the two beam theory for higher accelerating voltages. These results were explained by Goringe et.al. [28] who applied the two-beam method for measuring absorption parameters to multibeam intensity profiles obtained by taking the effects of systematic reflections into account. The effects of low angle inelastic scattering on measurements of absorption parameters have been investigated by several authors [75,99,100] who showed that the values of the anomalous absorption parameters, N_g, were a function of objective aperture size. Measurements of N_o on the other hand, were found to be independent of objective aperture size used.

The limitations of the two beam method indicate the desirability of developing an alternative technique for determining absorption parameters. In a recent paper Spring and Steeds [101] have proposed a method which employs the multibeam theory. Their method is based on observations of the fringe pattern obtained

when a specimen is bent. In order to avoid the effects of non-systematic reflections, a cylindrically bent speciment is required and the computer calculation requires a two-dimensional display of intensity expressed as a function of both crystal thickness and $\Delta\theta$, the deviation from the Bragg condition. The multibeam effects observed are more marked in heavy metals and the technique is therefore especially suitable for these materials.

In the present work a method was developed to measure absorption parameters in the material concerned which avoids the difficulties and limitations of the method suggested by Spring and Steeds [101], as well as the two-beam method. The method is based on a comparison of the intensity profile obtained at a given value of $\Delta\theta$ with the results obtained from computer calculations. Experimentally a small region of crystal of constant orientation is required, and computer calculations therefore require only the usual "one-dimensional" plots of intensity as a function of depth in the crystal.

It is important to mention that a check on the values of absorption parameters obtained by using the present method was also carried out by employing an alternative technique which uses stacking fault profiles. Details on both of these techniques are described in the next sections.

3:3.1 DETERMINING OF ABSORPTION PARAMETERS USING A PERFECT CRYSTAL WEDGE

This method [102] is based on the results reported by Sheinin [103], Sheinin and Cann [104], and Cann and Sheinin [105] which showed that for certain crystal orientations multibeam effects in perfect crystals become important. Under these conditions, thickness contours in the dark field image of a crystal wedge exhibited fringes which are complex in character. Fig.8 shows an example of these extinction contour profiles. In this figure the variation of diffracted beam intensity at the bottom surface of an fcc cobalt crystal is calculated assuming that the (111) set of systematic reflections only is excited at 150 kV. The deviation of the (111) reflection from its Bragg condition was taken to be $\Delta\theta_{111} = 1.75\ \theta_{111}$ ($\Delta\theta_g$, hereafter will be taken to indicate the deviation of the lowest order reflection in the systematic set concerned. This deviation parameter which is expressed in terms of fractions of the Bragg angles, has a sign convention the same as that of S_g.)

In order to illustrate the effects of absorption on the image profiles, calculations have been performed for the same diffraction conditions and for progressively higher values of anomalous absorption

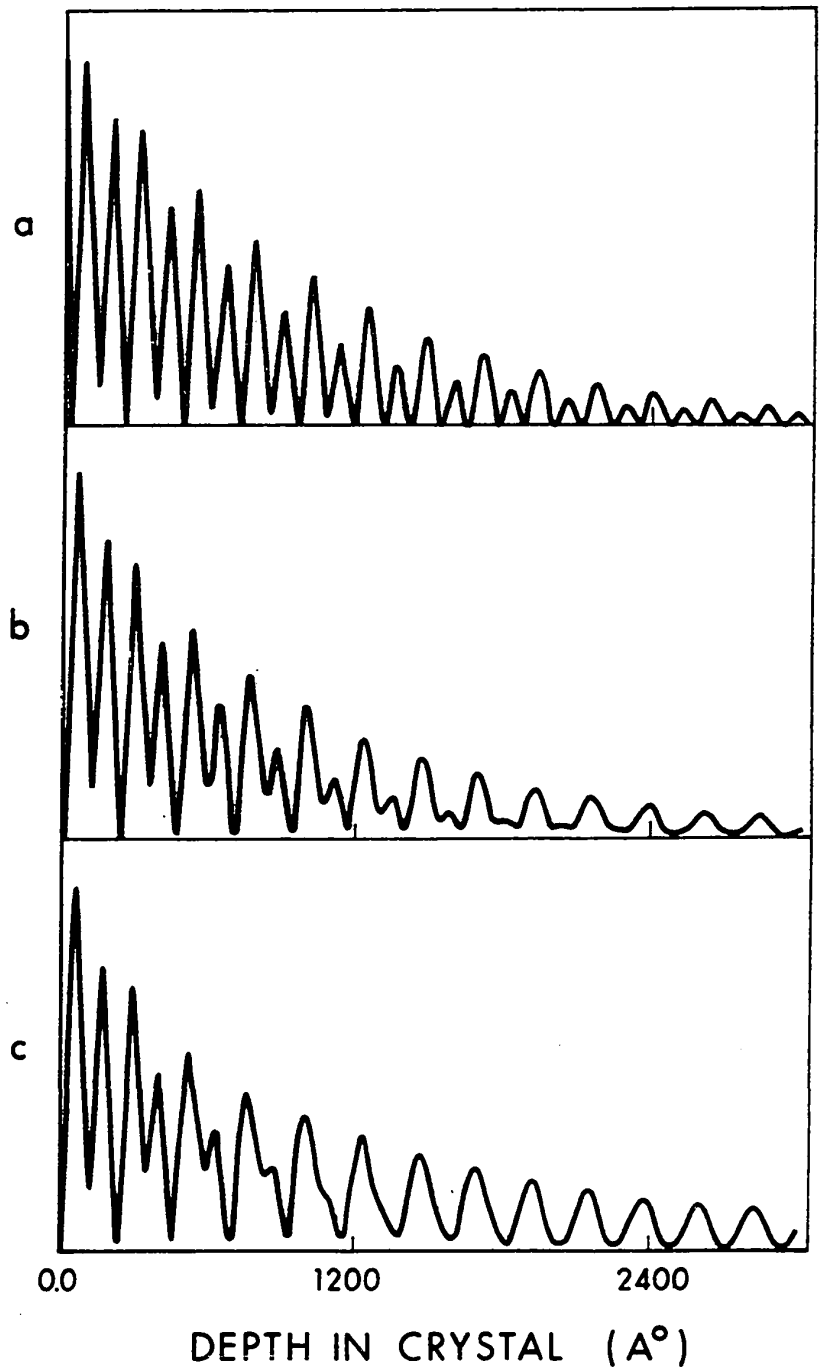

Fig.8 Dark field thickness fringe profiles for the (111) systematic row in fcc cobalt at a value of $\Delta\theta_{111} = 1.75\ \theta_{111}$ and at an accelerating voltage of 150 kV. N_o is kept constant at 0.03 and the anomalous absorption parameters were a) $N_g = 0$, $N_{2g} = 0..$, b) $N_g = .03$, $N_{2g} = .06...$ and c) $N_g = 0.06$, $N_{2g} = 0.12...$

parameters, N_g. The results of these calculations are shown in Fig. 8. If anomalous absorption is absent as in Fig. 8a, the profile obtained shows that thickness fringes exhibit a doublet structure which persists to any value of crystal thickness. Figs. 8 b,c illustrate what happens when the anomalous absorption parameters are increased. These profiles show that fringes in thinner parts of the crystal are complex in shape and are doublets while fringes obtained in thicker crystal are sinusoidal in character and are singlets. The number of fringes which are complex in shape can be seen to depend upon the set of anomalous absorption parameters used. Fig. 8b, for example, shows suppression of the doublet structure beyond a crystal of thickness about 2200 A°, while for Fig. 8c this suppression shifts to a value of about 1200 A°.

It is clear therefore that the values of the anomalous absorption parameters chosen have a marked effect on the character of the profile obtained. This fact provides a method for determining these parameters experimentally. The method consists of obtaining an experimental microdensitometer profile from a dark field micrograph recorded under the same diffraction conditions mentioned in obtaining Fig. 8. A set of anomalous absorption parameters can then be chosen by comparing the

experimental trace with the theoretical profiles such as those given in Fig. 8, and choosing the set which gives best fit between the theory and experiment.

It should be noted that the method mentioned does not permit a unique set of absorption parameters to be obtained. The reason for this was given by Metherell and Fisher [106] who investigated the effects of using different functional relationships between N_g and g. The relationships they used were

$$N_g \propto |\vec{g}| \quad , \quad N_g \propto \frac{1}{|\vec{g}|} \quad , \text{ and } \quad N_g = \text{constant.}$$

Their results showed that a profile of the same shape can be obtained by using each of the above relations if the value of the parameters were suitably adjusted. These results indicate, therefore, that a unique set of absorption parameters cannot be associated with a profile of given shape and also that experimental determination of absorption parameters requires a certain functional relationship between N_g and $|\vec{g}|$ to be assumed. In the present work the relation $N_g \propto |\vec{g}|$ has been assumed since it approximates closely to the theoretical results of Humphreys and Hirsch [63].

The value obtained by using the method described above was $N_{111} = 0.060 \pm 0.005$ with higher order Fourier coefficients obtained by assuming $N_g \propto |\vec{g}|$, This measured value was found to be in close agreement with the theoretical value of 0.060 given by Humphreys and Hirsch [63]. This theoretical value is, however, approximate since it was obtained by interpolation from Fig. 2a of their paper [63], noting the dependence of absorption parameters of different materials on their number.

Sheinin, Botros and Cann [102] have shown that once a set of anomalous absorption parameters have been deduced, the same method can be used to find a value for N_o. However, the value of this parameter is not required for purposes of the present work which is mainly concerned with stacking fault contrast. That N_o does not affect stacking fault contrast can be seen from Fig. 9, which shows the profiles obtained for an $\alpha = +2\pi/3$ fault in fcc cobalt crystal, when $\Delta\theta_{111} = 0.0$. The value of N_o in Figs. 9a, b, and c were 0.01, 0.03, and 0.06 respectively, and the values of N_g were kept constant in each case. It is clear by comparing Figs. 9a, b, and c that although the overall image intensity changes, stacking fault contrast remains identical and is therefore independent of normal absorption.

Finally it is important to mention that the diffraction conditions used in the present investigation

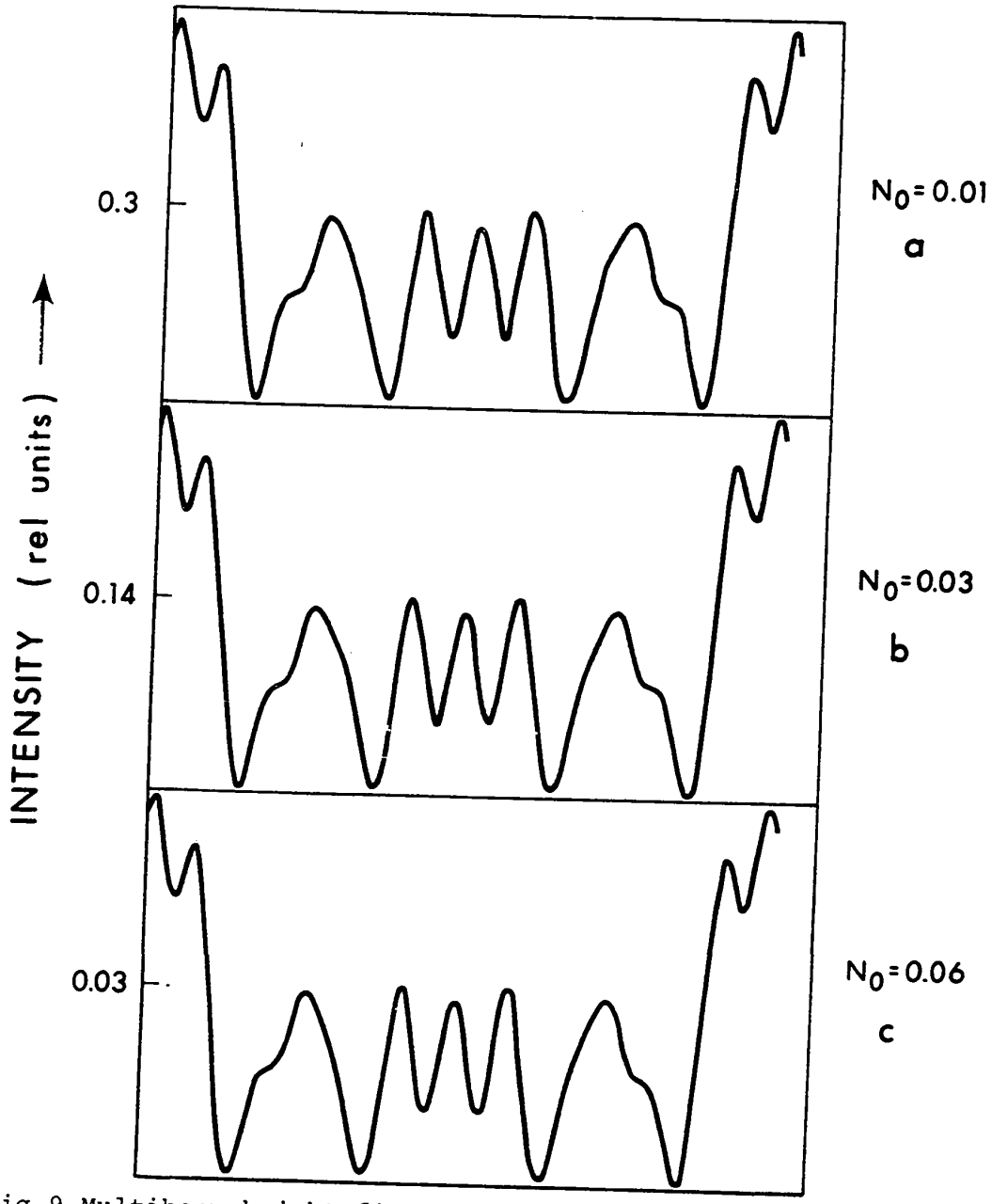

Fig.9 Multibeam bright field profiles for an $\alpha=2\pi/3$ stacking fault in a crystal of thickness equal to five extinction distances. The anomalous absorption parameter in each case was N_g= 0.06 while the normal absorption parameters were a) N_o= 0.01, b) N_o= 0.03 and c) N_o=0.06.

for fcc cobalt were different from those used by Sheinin et.al. [102] in molybdenum. It is therefore suggested that different crystal orientations must be investigated in the material concerned in order to determine the conditions which are most suitable for use in determining absorption parameters.

3:3.2 DETERMINATION OF ABSORPTION PARAMETERS FROM STACKING FAULT PROFILES

Since the present work is mainly concerned with studying stacking fault contrast, it was thought to be quite important to have an independent check on the values of absorption parameters obtained in section 3:3.1. To this end, a method which uses stacking fault profiles was utilized. Hashimoto et.al. [14,15] have shown that when a low order reflection satisfies the exact Bragg condition, the effects of anomalous absorption on stacking fault contrast are most pronounced. These effects result in stacking fault fringes which have a structure depending on the value of anomalous absorption parameters. A method can be used, therefore, which is based on a comparison of experimental stacking fault profiles obtained at different crystal thicknesses to theoretical profiles calculated under the same conditions. The correct values of absorption parameters

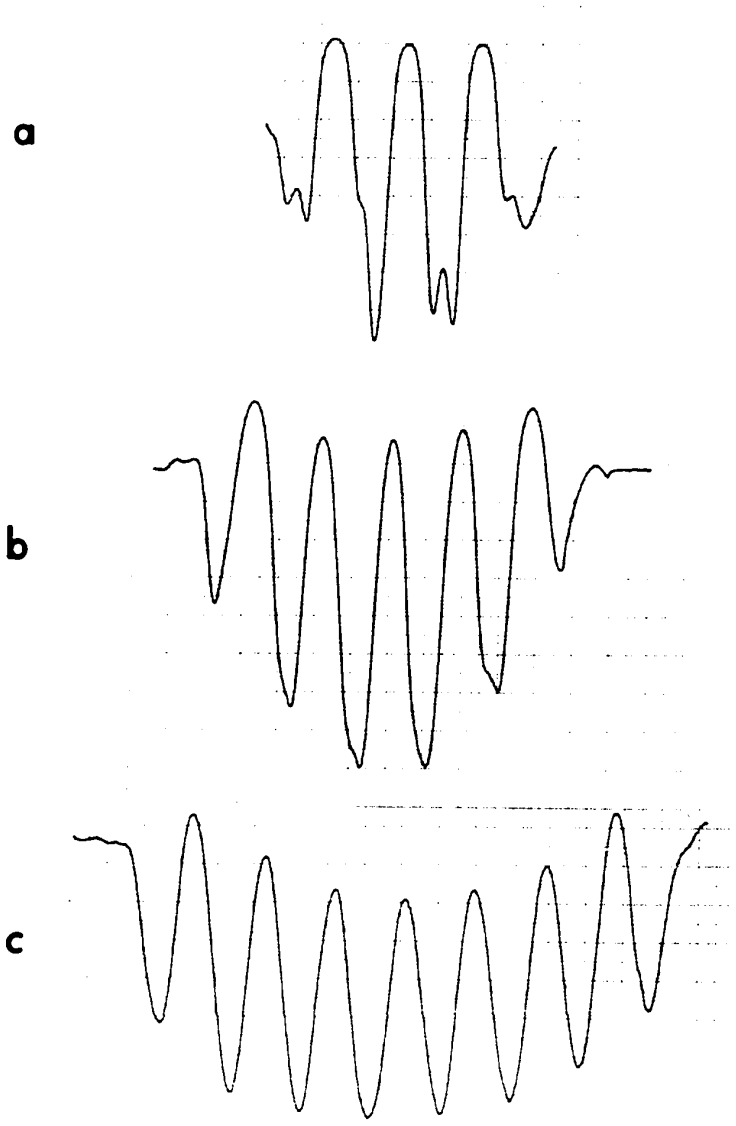

Fig. 10 Experimental bright field profiles for an $\alpha = 2\pi/3$ stacking fault in fcc cobalt. The (111) reflection was in the exact Bragg condition and the accelerating voltage was 150 kV. Crystal thicknesses are: a) 3.5; b) 5.5; and c) 7.5 extinction distances.

would again be those which give best fit between theory and experiment.

The actual experimental arrangement was to record bright field stacking fault images in fcc wedge cobalt crystals, when the (111) reflection was at the exact Bragg condition. Care was taken so that as far as possible only the (111) set of systematic reflections was excited. Experimental microdensitomer traces were then recorded from the resulting micrographs at values of crystal thicknesses corresponding to maxima and minima in directly transmitted intensity (i.e., at crystal thicknesses corresponding to n and $(n+\frac{1}{2})$ extinction distances). The experimental results are illustrated in Fig. 10 by the profiles obtained at values of crystal thicknesses of $3\frac{1}{2}$, $5\frac{1}{2}$, and $7\frac{1}{2}$ extinction distances respectively. It can be seen from Fig. 10 that a gradual disappearance of the structure of stacking fault fringes occurs as crystal thickness increases. This behaviour actually consists of a transition from the doublet structure obtained in relatively thin crystal (see Fig. 10a) to singlets in thicker crystals (Fig. 10c). The change in the structure of stacking fault fringes is sensitive to the values of the set of absorption parameters used. This can be seen from Fig. 11 where the theoretical multibeam profiles are presented for two different values

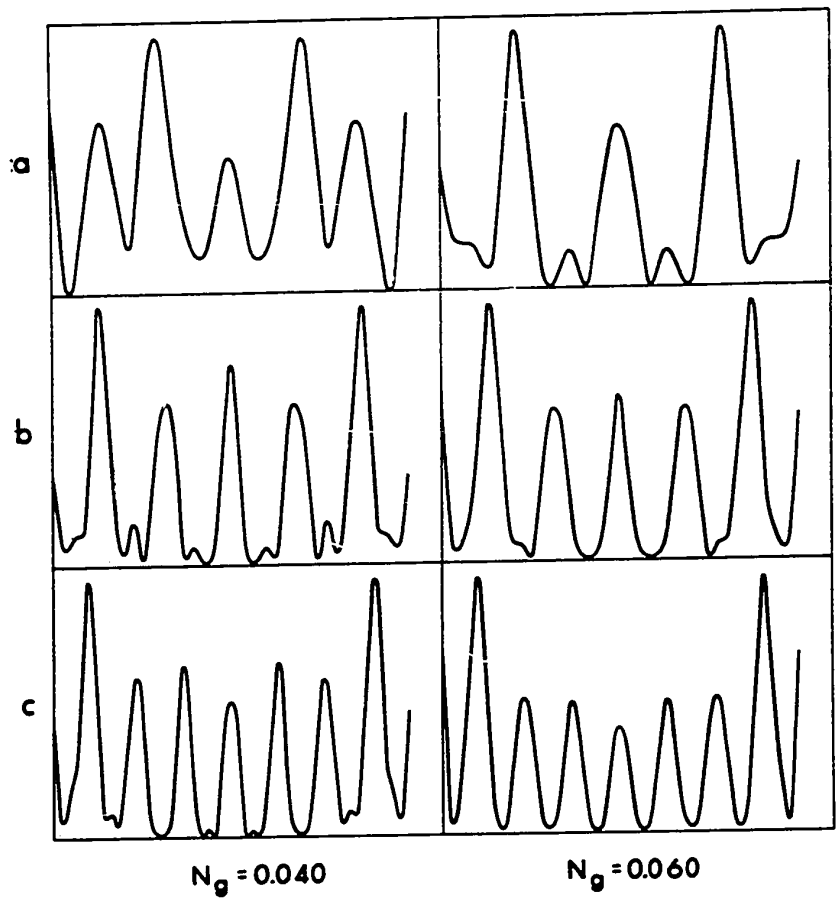

Fig. 11 Multibeam bright field profiles corresponding to the experimental profiles in Fig. 10. The sets of anomalous absorption parameters used are given namely $N_g = 0.04$ and $N_g = 0.06$.

of N_g, namely .04 and .06. The profiles on the left of Fig. 11 show that when N_g = .04 the doublet structure would persist to crystals of thickness 7½ extinction distances. On the other hand when N_g = .06 (profiles in the right hand side of Fig. 11) the doublet structure is not observed for crystals of thickness over 5½ extinction distances. Thus by comparison of experimental profiles such as those given in Fig. 10, with theoretical profiles,such as those of Fig. 11, it is possible to obtain a set of anomalous absorption parameters which gives good agreement between theory and experiment. The values obtained by the procedure outlined above were in very good agreement with the values $N_g = 0.06 \pm .005$ obtained by the method discussed in section 3:3.1.

The last point to note in this section is the relative insensitivity of the profiles to the values of absorption parameters used when crystal thicknesses were n extinction distances. This is illustrated in Fig. 12 by the multibeam profiles obtained for crystal thicknesses 4, 6, and 8 extinction distances at two values of N_g namely 0.04 and 0.06. As can be seen from Fig. 12, the structure in the stacking fault fringes at those crystal thicknesses changes only slightly as N_g increases. It is therefore clear that when the bright field image is used to determine absorption

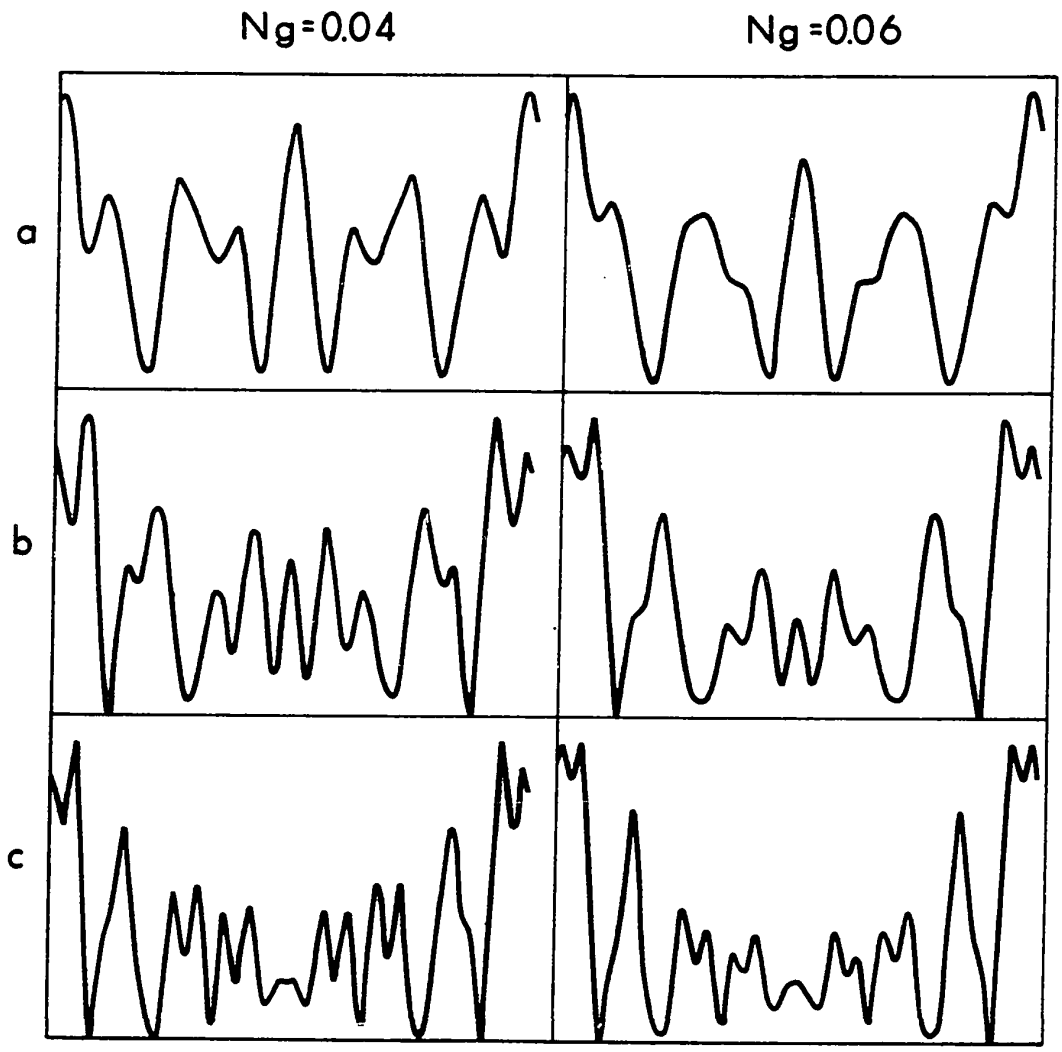

Fig. 12 Multibeam bright field profiles for an $\alpha = 2\pi/3$ fault in fcc cobalt. The (111) set of systematic reflections only are assumed excited at 150 kV, with $\Delta\theta_{111} = 0$. The values of anomalous absorption parameters used are given on the graphs, and the values of crystal thicknesses considered are a) 4.0, b) 6.0 and c) 8.0 extinction distances respectively.

parameters, attention should be focused on profiles corresponding to crystals (n+½) extinction distances thick since these profiles are the most sensitive to the value of anomalous absorption parameters used.

CHAPTER 4

ANALYSIS OF IMAGE CONTRAST IN TERMS OF BLOCH WAVE INTERACTIONS

4:1 INTRODUCTION

The motion of high energy electrons in a crystal is represented in the dynamical theory in terms of the propagation of Bloch waves. Consequently an understanding of the nature of image contrast in transmission electron microscopy is based on the study of the extent to which the different Bloch waves are excited and the extent to which they contribute to the amplitudes of the different diffracted beams.

The first part of this chapter (section 4:2) presents the way in which image contrast can be analyzed in perfect crystals in terms of the different Bloch wave interactions. In order to follow the different Bloch wave interactions down through a crystal containing a stacking fault, interbranch and intrabranch scattering of these Bloch waves at the fault has to be considered. The multibeam expressions which allow stacking fault contrast to be studied when more than two Bloch waves are important have not presented in the literature and are therefore derived in section (4:3) of this chapter.

4:2 ANALYSIS OF THICKNESS FRINGE CONTRAST FOR A PERFECT CRYSTAL

The starting point is equation 2.15 of Chapter 2. By carrying out the matrix multiplication of equation 2.15, it is possible to show that the expression for a particular diffracted beam is,

$$\phi_g(z) = \sum_i^N \phi_g^i \exp 2\pi i \gamma^i z$$

where

$$\phi_g^i = C_o^i C_g^i \exp -2\pi q^i z \quad . \qquad (4.1)$$

The summation in equation 4.1 is carried out over all the Bloch waves considered in a particular calculation. It can be seen that the contribution of the i^{th} Bloch wave to the diffracted beam intensity depends upon the value of $\phi_g^i = C_o^i C_g^i \exp -2\pi q^i z$. In the present work a Bloch wave will be referred to as being important or otherwise on the basis of its contribution to the diffracted beam intensity and will therefore be determined by the value of this quantity. It can also be seen from equation 4.1 that two important Bloch waves give rise to sinusoidal fringes of high contrast in a perfect crystal wedge. On the other hand one important Bloch wave gives rise to weak fringe contrast and more than

two Bloch waves with unequal values of γ^i will in general give rise to fringes which are non-sinusoidal in character.

The above discussion shows therefore that a study of thickness fringe contrast in perfect crystals, can be carried out by following the magnitudes of the ϕ_g^i's at different depths in the crystal.

4:3 MULTIBEAM THEORY OF INTERBRANCH AND INTRABRANCH SCATTERING FOR A STACKING FAULT

The diffracted beam amplitudes for a crystal containing a stacking fault at a depth t_1, can be written,as in equation 2.20 in terms of the total scattering matrix $\underline{P}(t)$ of the faulted crystal

$$\underline{\phi}_g(t) = \underline{P}(t)\ \underline{\phi}_g(0) \quad . \tag{4.2}$$

An alternate expression for the diffracted beam amplitudes, analogous to that of equation 2.11 of the perfect crystal,can be written as

$$\underline{\phi}_g(t) = \underline{O}^{-1}\underline{C}\ \exp\{2\pi i(\gamma^i + iq^i)t\}\underline{\Psi}_1 \tag{4.3}$$

where the column vector $\underline{\Psi}_1$ contains the new excitation amplitudes Ψ_1^i below the fault which are functions of depth of fault in the crystal. Now by linearly

transforming equation 4.3 an expression for $\underline{\Psi}_1$ can be written as,

$$\underline{\Psi}_1 = \{\exp 2\pi i(\gamma^i + iq^i)t\}^{-1}\ \underline{C}^{-1}\ \underline{Q}\ \underline{\phi}_g(t) \quad .$$

Substituting the value of $\underline{\phi}_g(t)$ from equation 4.2 we get:

$$\underline{\Psi}_1 = \{\exp 2\pi i(\gamma^i + iq^i)t\}^{-1}\ \underline{C}^{-1}\ \underline{Q}\ \underline{P}(t)\ \underline{\phi}_g(0)$$

but from equation 2.12 we have $\underline{\phi}_g(0) = \underline{C}\ \underline{\Psi}$. Substituting this into the above equation we get,

$$\underline{\Psi}_1 = \{\exp 2\pi i(\gamma^i + iq^i)t\}^{-1}\ \underline{C}^{-1}\ \underline{Q}\ \underline{P}(t)\ \underline{C}\ \underline{\Psi}$$

or simply $\underline{\Psi}_1 = \underline{B}\ \underline{\Psi}$. (4.4)

The elements of the matrix $\underline{B}$ are given in the case of a crystal containing a stacking fault as,

$$B^{ij} = \exp - 2\pi i(\gamma^i - \gamma^j)t_1 \exp 2\pi(q^i - q^j)t_1 \sum_g C_g^i C_g^j\ e^{2\pi i\vec{g}.\vec{R}}. \quad (4.5)$$

where the summation in equation 4.5 extends over all reciprocal lattice vectors $\vec{g}$.

It can be seen from equation 4.5 that the value of ψ_1^i below the fault depends upon the excitation amplitude of the same Bloch wave above the fault ψ^i, as

well as the amplitudes of all the other Bloch waves above the fault ψ^j. Thus the matrix elements B^{ij} represent interbranch scattering from Bloch wave b^j (or the j^{th} branch of the dispersion surface) to Bloch wave b^i (or the i^{th} branch of the dispersion surface). On the other hand, the matrix element B^{ii} will represent scattering of Bloch wave b^i into itself and is referred to as intrabranch scattering.

The contributions of the various interbranch and intrabranch scattering terms to the diffracted beam amplitudes can be obtained by substituting 4.4 into 4.3 giving,

$$\underline{\phi}_g(t) = \underline{Q}^{-1}\ \underline{C}\ \{\exp 2\pi i(\gamma^i + iq^i)t\}\underline{B}\ \underline{\psi}\ . \quad (4.6)$$

From equation 4.6 the expression for the amplitude of a particular diffracted beam $\phi_g(t)$ can be easily seen to be,

$$\phi_g(t) = \sum_i \sum_j \phi_g^{ij} \exp 2\pi i\gamma^i t$$

where

$$\phi_g^{ij} = C_g^i\ C_o^j\ B^{ij} \exp - 2\pi i\vec{g}.\vec{R} \exp - 2\pi q^i t\ . \quad (4.7)$$

The summation in equation 4.7 is from 1 to N, where N is the number of beams taken into account in a particular calculation.

An important point to note from equations 4.5 and 4.7 is that fringe contrast for a stacking fault inclined to the surfaces of a foil must mainly arise due to interbranch scattering. This can be seen from the fact that intrabranch contributions (terms like ϕ_g^{ii}) will contain the matrix elements B^{ii} which are in turn independent of t_1, the depth of the fault in the crystal. On the other hand, the interbranch contributions (terms like ϕ_g^{ij}) are dependent on t_1. It should also be noted that the interbranch and intrabranch contributions to the diffracted beam amplitudes (equation 4.7) are complex quantities, and can therefore best be studied by utilizing phase amplitude diagrams.

In the present work analysis of image contrast for the faulted crystal was facilitated by writing a computer program which calculates the magnitudes as well as the phase angles of the different Bloch wave contributions ϕ_g^i, and ϕ_g^{ij}. For any fault depth t_1, the calculations of ϕ_g^i's were carried out at the top surface of the crystal, and just above the fault. The contributions ϕ_g^{ij}'s, ϕ_g^{ii}'s from inter- and intrabranch scattering were then calculated just below the fault as well as at the bottom surface of the crystal.

CHAPTER 5

ON THE NATURE OF STACKING FAULT IMAGES AT LOW ACCELERATING VOLTAGE WHEN A LOW ORDER REFLECTION SATISFIES THE EXACT BRAGG CONDITION

5:1 INTRODUCTION

In the course of using theoretical multibeam extinction contour profiles for deducing values of crystal thickness at which stacking fault calculations were to be carried out (see sections 3:1.6, 3:3.2) it was found that the effective extinction distance depended on the value of crystal thickness. This can be seen from Fig. 13 which shows the bright field extinction contours obtained by assuming the (111) set of reflections to be excited. The accelerating voltage was taken to be 150 kV in the calculation and $\Delta\theta_{111} = 0$. The effective peak-to-peak separation (extinction distance) in thin parts of the crystal can be seen to be 250 A°, while in thick crystal the effective extinction distance decreases to a value of only 180 A°.

Botros and Sheinin [107] have analyzed these results in terms of the important Bloch waves which give rise to thickness fringe contrast. Their analysis indicated that in thin parts of the crystal, the multibeam extinction distance was close to $1/(\gamma^1-\gamma^2)$ showing

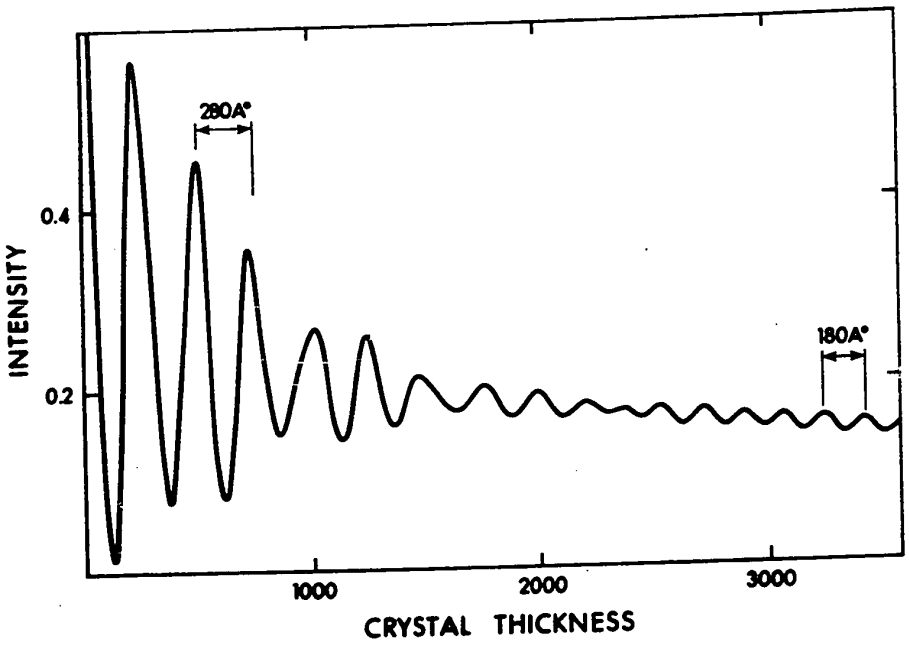

Fig. 13 The variation of directly transmitted intensity with crystal thickness for the (111) systematic row in fcc cobalt when the (111) reflection is assumed to be in the exact Bragg condition and at an accelerating voltage of 150 kV.

that in this thickness range, the character of thickness contours can be described, as in the two beam theory, in terms of Bloch waves 1 and 2. In thick crystal, however, the extinction distance was found to be close to $1/[\gamma^2 - \frac{1}{2}(\gamma^3+\gamma^4)]$ with $\gamma^3 \sim \gamma^4$, indicating that in this thickenss range, fringes arise from the interactions of Bloch waves 2, 3 and 4. The above results show therefore, that the effects of systematic reflections increase by increasing crystal thickness. The possibility arises that similar effects might occur in crystals containing stacking faults. In order to explore this possibility an investigation of the dependence of fault contrast on crystal thickness was undertaken. The experimental results (section 5:2) have been compared with computer calculations of image contrast based on the two and multibeam dynamical theories. Finally in order to gain some insight into the mechanisms producing image contrast, the results have been analyzed and discussed in terms of interbranch and intrabranch transitions of Bloch waves (sections 5:3 and 5:4).

5:2 RESULTS

Observations of stacking fault contrast both in the bright and dark field, as function of crystal thickness were carried out using wedge crystals of cobalt.

All observations were made at 150 kV after orienting the crystal so that, as nearly as possible, only the (111) set of systematic reflections was excited and setting the (111) reflection in the exact Bragg condition. Experimental stacking fault profiles were examined at values of crystal thickness in the approximate range of five to fifteen extinction distances. It was found that the variation in contrast of the central fringes of a stacking fault image with crystal thickness was quite different from that of edge fringes. Therefore the results of each are presented in separate sections. Sections 5:2.1(a), (b), and (c) describe the behaviour of the central fringe pattern as crystal thickness increases, while section 5:2.2 is devoted to presenting the results which describe the manner in which edge fringes in a stacking fault image depended on crystal thickness.

5:2.1 THE DEPENDENCE OF THE CENTRAL FRINGE CONTRAST IN A STACKING FAULT IMAGE ON CRYSTAL THICKNESS

The results obtained for the contrast of central fringes have been divided into two ranges of crystal thickness. These are referred to as moderately thick and thick respectively. A moderately thick crystal, for the case of the (111) set of systematic reflections in

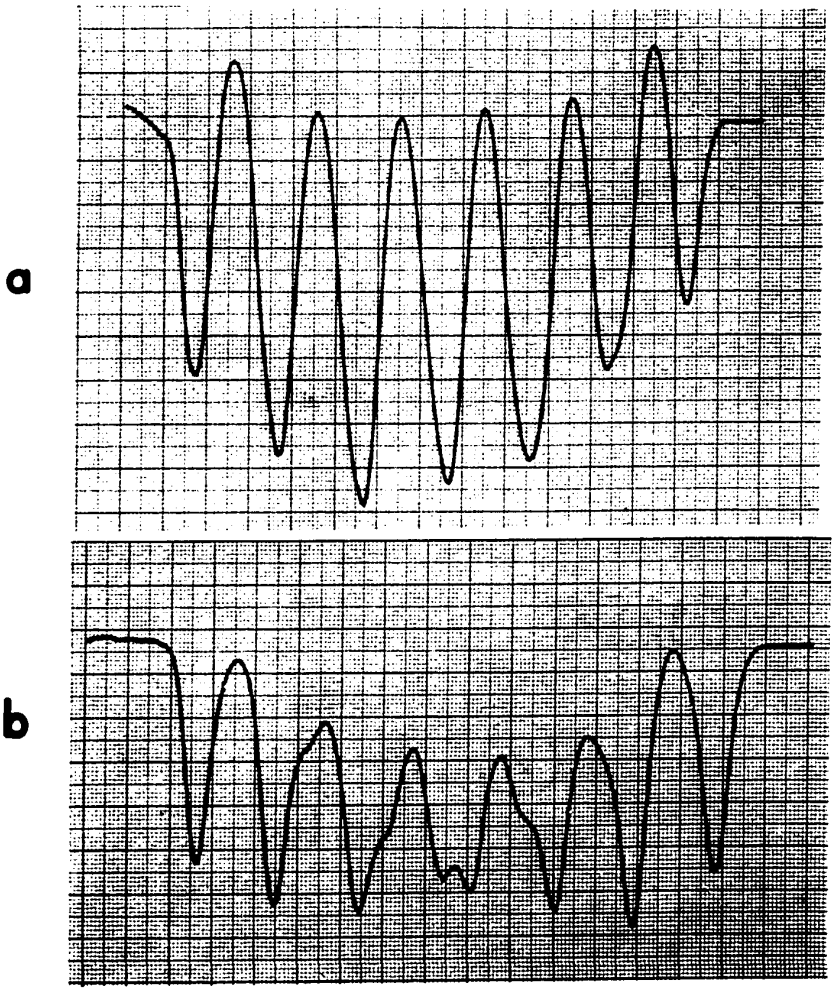

Fig. 14 Experimental bright field profiles for an $\alpha = -2\pi/3$ fault in crystals of the following thickness: a) 6.5 extinction distances, b) 7.0 extinction distances. The (111) set of systematic reflelctions only was excited at 150 kV, with $\Delta\theta_{111} = 0$.

fcc cobalt, was taken to be one with thicknesses in the range of five to nine extinction distances, while thick crystals were those with thicknesses greater than nine extinction distances. Bright field results are presented in sections 5:2.1(a), 5:2.1(b), while the manner in which dark field contrast depended on crystal thickness is discussed in section 5:2.1(c).

5:2.1(a) Fringe Contrast in Moderately Thick Crystals

The manner in which central fringe contrast changes with crystal thickness in moderately thick crystals is illustrated by the experimental profiles given in Fig. 14. These bright field profiles show the stacking fault fringes of an $\alpha = -2\pi/3$ fault at values of crystal thickness corresponding to 6.5 and 7.0 extinction distances. As can be seen from Fig. 14b, when the crystal is n extinction distances thick, the stacking fault fringes near the centre of the fault consist of doublets which exhibit relatively weak contrast. Fig. 14a on the other hand, shows that when crystal thickness is $(n+\frac{1}{2})$ extinction distances, the fringes near the centre of the fault are singlets and exhibit relatively high contrast.

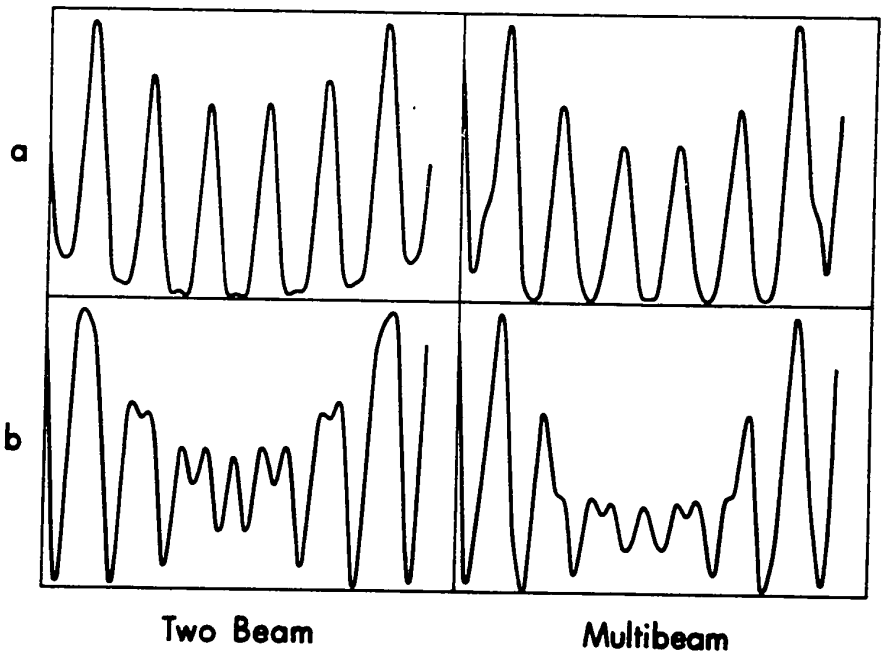

Fig. 15 Two and multibeam profiles for an $\alpha = -2\pi/3$ stacking fault in crystals of the following thickness a) 6.5 and b) 7.0 extinction distances. Profile calculations took into account the (111) set of systematic reflections in fcc cobalt with $\Delta\theta_{111} = 0$. The accelerating voltage was taken to be 150 kV.

The next point to consider is the comparison of these results with theoretical calculations based on the two and multibeam dynamical theories. Fig. 15 illustrates the theoretical results obtained for moderately thick crystals. The first feature of interest in comparing Figs. 14 and 15 is that good agreement is obtained between experiment and the two beam profiles. That this is so can be seen by comparing the detailed shapes of both experimental and theoretical profiles as well as noting that the marked difference in contrast obtained experimentally between stacking fault images in crystals of thickness n and (n+½) extinction distances is also predicted by the two beam theory. A second point of interest to note from the theoretical profiles given in Fig. 15, is that there are no significant differences in the results obtained from the two and multibeam calculations, thus indicating that in the range of crystal thickness so far considered, systematic reflections have no significant effect on the contrast of the central fringe pattern in a stacking fault image.

5:2.1(b) Fringe Contrast in Thick Crystals

The next question which arises is whether or not the results presented in section 5:2.1(a) for moderately thick crystals are also characteristic of thick crystals.

In order to investigate this question experimentally some difficulties were encountered. These difficulties resulted from the fact that images of thickness fringes became too faint in thick crystals to permit stacking fault profiles to be recorded at a particular value of crystal thickness. In an attempt to overcome this difficulty, long exposure micrographs were recorded. Although this procedure increased the visibility of the contours, there was still too much uncertainty in determining the positions of intensity maxima or minima of these thickness fringes to permit accurate determination of crystal thickness. This difficulty was finally overcome by determining from extinction contours in relatively thin parts of the crystal, the distance perpendicular to the contours required to give a certain crystal thickness increment. This distance would give the same thickness increment in thicker parts of the crystal provided a specimen with a uniform wedge was under observation. The uniformity of the wedge was easily judged from the overall shape of the stacking fault image (such as the one shown in Fig. 6) since the fault runs from the top to the bottom surface of the crystal. Using this method to determine changes in crystal thickness with distance from the edge of the specimen, microdensitomer traces were recorded at thickness increments of about 25 A°

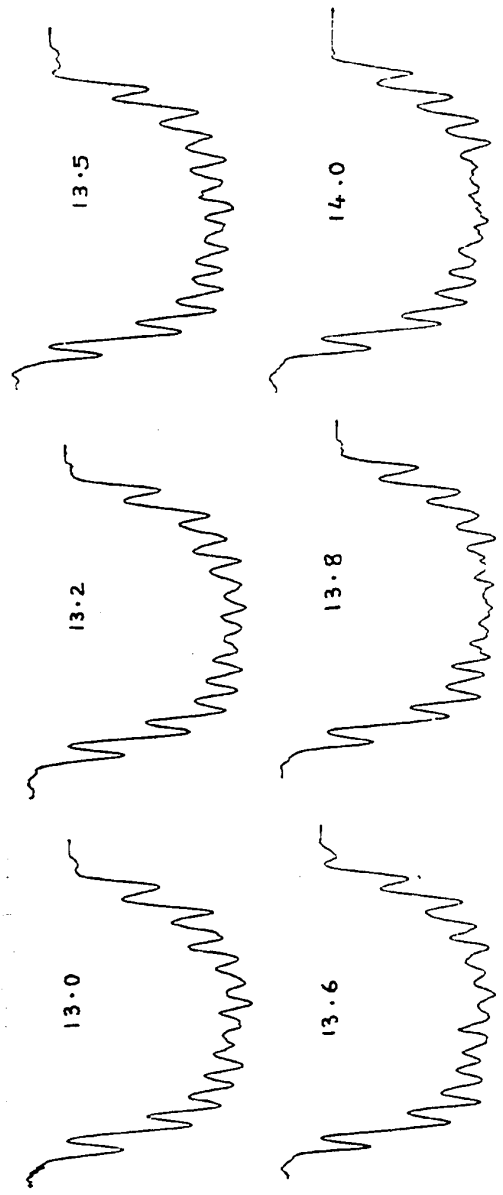

Fig. 16 Experimental bright field profiles for an $\alpha = -2\pi/3$ fault in fcc cobalt crystal of thickness in the range 13 to 14 extinction distances. The (111) reflection was in the exact Bragg condition and the accelerating voltage employed was 150 kV. The value of crystal thickness in each case is given with the profile.

(which corresponds approximately to 1/10 extinction distance in thinner parts of the crystal) in the approximate range of crystal thickness from 10.5 to 15.5 extinction distances. The experimental results illustrated in Fig. 16 for the crystal thickness range 13.0 to 14.0 extinction distances is typical of what was obtained in thick crystals. These profiles indicate that there is no pronounced thickness dependence of the contrast for fringes near to the centre of the fault and also that these fringes exhibit weak contrast. The interesting point to note here is that the difference in contrast of the stacking fault fringes in crystals of thicknesses equal to n and (n+½) extinction distances observed in moderately thick crystals (see section 5:2.1(a)) does not persist in thick crystals.

In an attempt to understand these results, calculations of stacking fault contrast were performed in the range of crystal thickness from 10.5 to 15.5 extinction distances. The results obtained are illustrated in Fig. 17b,c which shows the results obtained for a crystal of thickness 12.5 extinction distances for both the two- and multibeam cases respectively. Fig. 17a is the experimental profile obtained for the same value of crystal thickness. The two beam profile in Fig. 17b is in poor agreement with the experimental profile in that it shows that fringes near

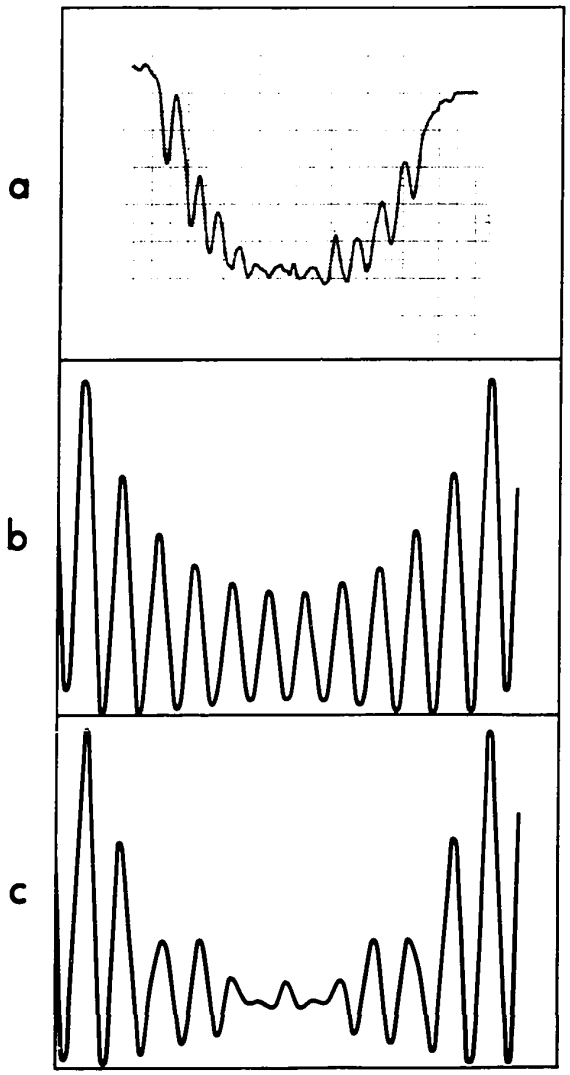

Fig. 17 Bright field profiles for an $\alpha = -2\pi/3$ stacking fault in a crystal of thickness 12.5 extinction distances. a) experimental profile, b) two beam profile and c) multi-beam profile taking the (111) set of systematic reflections into account.

the centre of the fault should be singlets of good contrast. The profile obtained by taking the effects of multiple reflections into account, given in Fig.17c, is in good agreement with experimental results and shows that the central pattern consists of fringes which exhibit poor contrast. It can therefore be seen that effects of systematic reflections become important in thick crystals and that the effect of these reflections is to reduce contrast.

5:2.1(c) Behaviour of Central Fringes in Dark Field Images

The way the contrast of central fringes in a dark field image depended on crystal thickness was found to be quite analogous to that described in sections 5:2.1(a), (b). However, for moderately thick crystals, singlets of high contrast were obtained at values of crystal thickness of n extinction distances rather than (n+½). Doublets of weak contrast occurred in the dark field when the values of crystal thicknesses were (n+½) rather than n extinction distances. In thick crystals the behaviour of the central fringes of the dark field image was the same as in the bright field, i.e., they exhibited poor contrast which was independent of crystal thickness.

5:2.2 THE DEPENDENCE OF THE CONTRAST OF FRINGES NEAR CRYSTAL SURFACES ON CRYSTAL THICKNESS

The variation in the contrast of the edge fringes of a stacking fault image with crystal thickness was quite different from that found for the central fringes in sections 5:2.1(a), (b), and (c). This is illustrated for a fault in a moderately thick crystal in Fig. 14 which shows that edge fringes are singlets regardless of whether the crystal thickness is n or (n+½) extinction distances. The results obtained in thick crystals indicated that the character of these fringes remained unchanged. This is evidenced by the experimental profiles given in Fig. 16 which show that for a thick crystal in the range of 13 to 14 extinction distances the edge fringes obtained were singlets of relatively high contrast.

A comparison of these experimental results with the theoretical profiles obtained from two and multi-beam theories shown in Fig. 17b, c indicates that in each case good agreement is obtained. It can therefore be concluded that the effects of systematic reflections on the contrast of edge fringes are small, regardless of crystal thickness. This of course is in contrast to the results obtained in sections 5:2.1(a), (b) and (c), which showed that effects of systematic reflections on central fringes increased with crystal thickness.

It is next of interest to consider the contrast exhibited by the two fringes which are immediately adjacent to the edges of the fault. The contrast of these fringes, as mentioned in section 1:3.1(b), is of particular interest from a practical point of view in determining the sense of slope of the fault in the crystal (see also the discussion given in section 5:4). It is important therefore in such determinations that the contrast exhibited by the outermost fringes can be easily and clearly recognized in both bright and dark field images. The ease with which these outermost fringes can be observed will depend on the ratio, $\delta I/I$, of the difference δI between maximum (or minimum) fringe intensity and background intensity, to that of background intensity I.

In moderately thick crystals this ratio, $\delta I/I$, was found to be dependent on whether the crystal thickness is n or $(n+\frac{1}{2})$ extinction distances. This is seen by examining the contrast of outermost fringes given in Fig. 18, which shows the bright and dark field profiles calculated for an $\alpha = 2\pi/3$ fault in fcc cobalt for crystals of thicknesses 6.0 and 6.5 extinction distances. When crystal thickness is n extinction distances, the contrast of the outermost fringes is most pronounced in the dark field profile of Fig. 18c. The reason for this

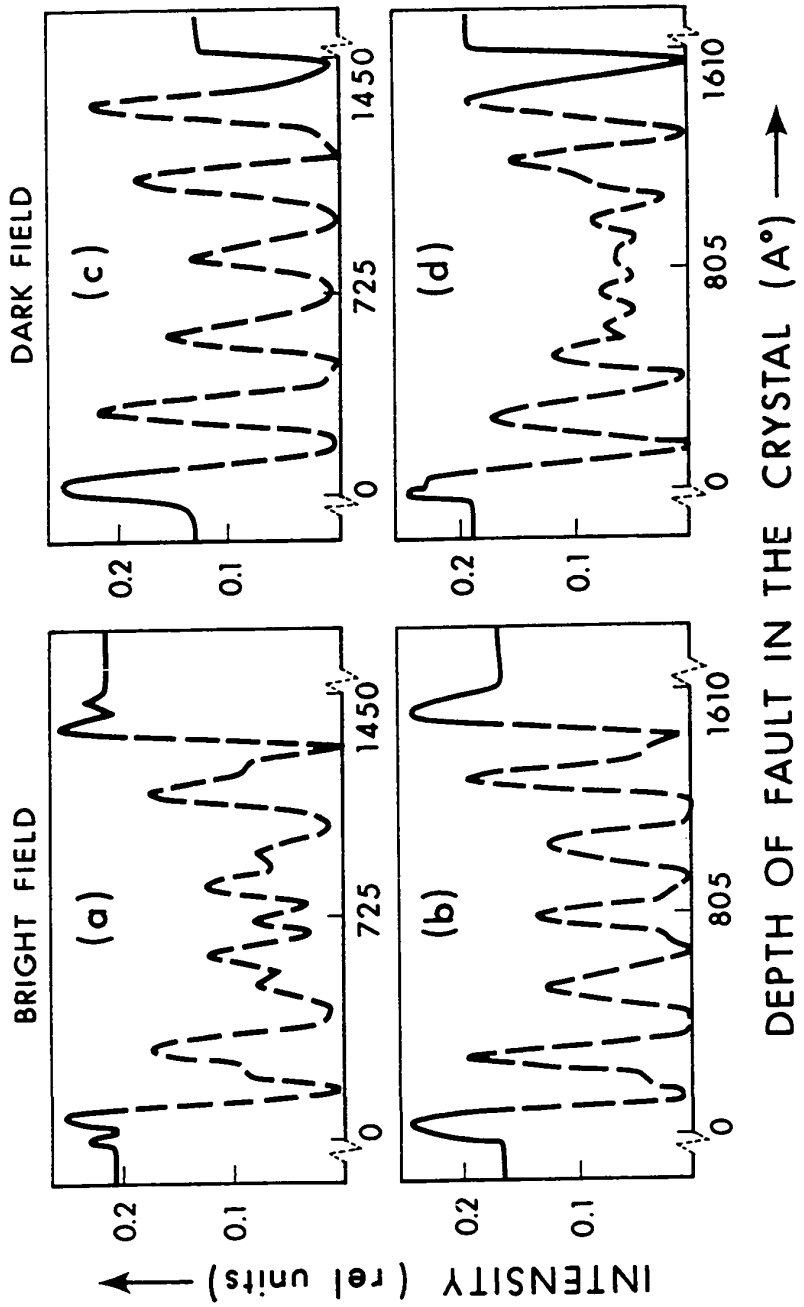

Fig. 18 Multibeam bright and dark field profiles for an $\alpha=2\pi/3$ fault in fcc cobalt. The (111) set of systematic reflections only was assumed excited at 150 kV with $\Delta\theta_{111}= 0$. Crystal thicknesses for a), c) are 6.0 extinction distances, and for b), d) are 6.5 extinction distances. The background intensity and the outermost fringes in each profile are shown by heavy lines.

is the low value of background intensity (at this crystal thickness a minimum occurs in diffracted beam intensity) and the high value of maximum fringe intensity. Consequently the ratio $\delta I/I$ for the outermost fringes is significantly greater in the dark field than the corresponding value obtained when bright field image is considered (compare Figs. 18a, c). The situation is reversed when crystals of thickness $(n+\frac{1}{2})$ extinction distances thick are considered. Fig. 18b shows that the ratio $\delta\bar{I}/I$ is highest in the bright field image and therefore the outermost fringes are most easily observed for these crystal thicknesses using bright field images. It is important to mention that in thick crystals, the above dependence of the contrast of outermost fringes on crystal thickness was not observed. This can be understood by considering the extinction contour profile given in Fig. 13 where it is clear that the variation in background intensity is significantly reduced in thick crystals. Consequently, in thick crystals the contrast of outermost fringes in images of stacking faults will be relatively independent of crystal thickness.

It can be concluded from the results presented above that in order to avoid possible errors in identifying the nature of outermost fringes in a stacking fault image one of the following methods can be employed:

(a) Observe the stacking fault in a wedge crystal when moderately thick crystals are considered.

or

(b) Observe the fault in a thick crystal where the contrast of the outermost fringes is independent of crystal thickness.

5:3 EXPLANATION OF RESULTS IN TERMS OF THE IMPORTANT BLOCH WAVE INTERACTIONS

Physical insight into the contrast producing mechanism can be gained by analyzing the resulting image in terms of the important Bloch wave interactions. Hashimoto et.al. [15] and Hirsch et.al. [71] considered an extremely thick crystal containing a stacking fault and analyzed the resulting image in terms of inter- and intrabranch scattering of Bloch waves 1 and 2 (see section 2:6 of Chapter 2). Their analysis explained the reasons for obtaining extremely poor contrast near the centre of the fault and relatively high contrast for edge fringes. Such an analysis, however, is qualitative in nature and is only relevant to faults lying in extremely thick crystals. In order to explain the thickness dependence of the contrast of central fringes obtained in moderately thick crystal (sections 5:2.1(a), (c)), it is therefore important to carry out a more

detailed analysis of image contrast. This analysis for moderately thick crystals of thickness n and (n+½) extinction distances is given in sections 5:3.1(a), (b). The next point to be considered is the explanation of the deleterious effects of the (111) set of systematic reflections on the contrast of fringes near the centre of a fault in a thick crystal. The results of this multibeam analysis are given in section 5:3.2. Finally in section 5:3.3 the effects of systematic reflections on the contrast of edge fringes are discussed.

5:3.1 MECHANISMS RESPONSIBLE FOR CENTRAL FRINGE CONTRAST IN MODERATELY THICK CRYSTALS

The analysis presented in this section is pertinent to the central fringes in the bright field image of a stacking fault lying in a moderately thick crystal. A dark field analysis is not presented since it was found to be quite similar to that of the bright field except for the differences noted, in section 5:2.1(c) regarding the values of crystal thickness at which singlets and doublets in the central fringe pattern occur.

The analysis of image contrast performed involved following interactions of Bloch waves 1 and 2 down through a faulted crystal for fault depths near the

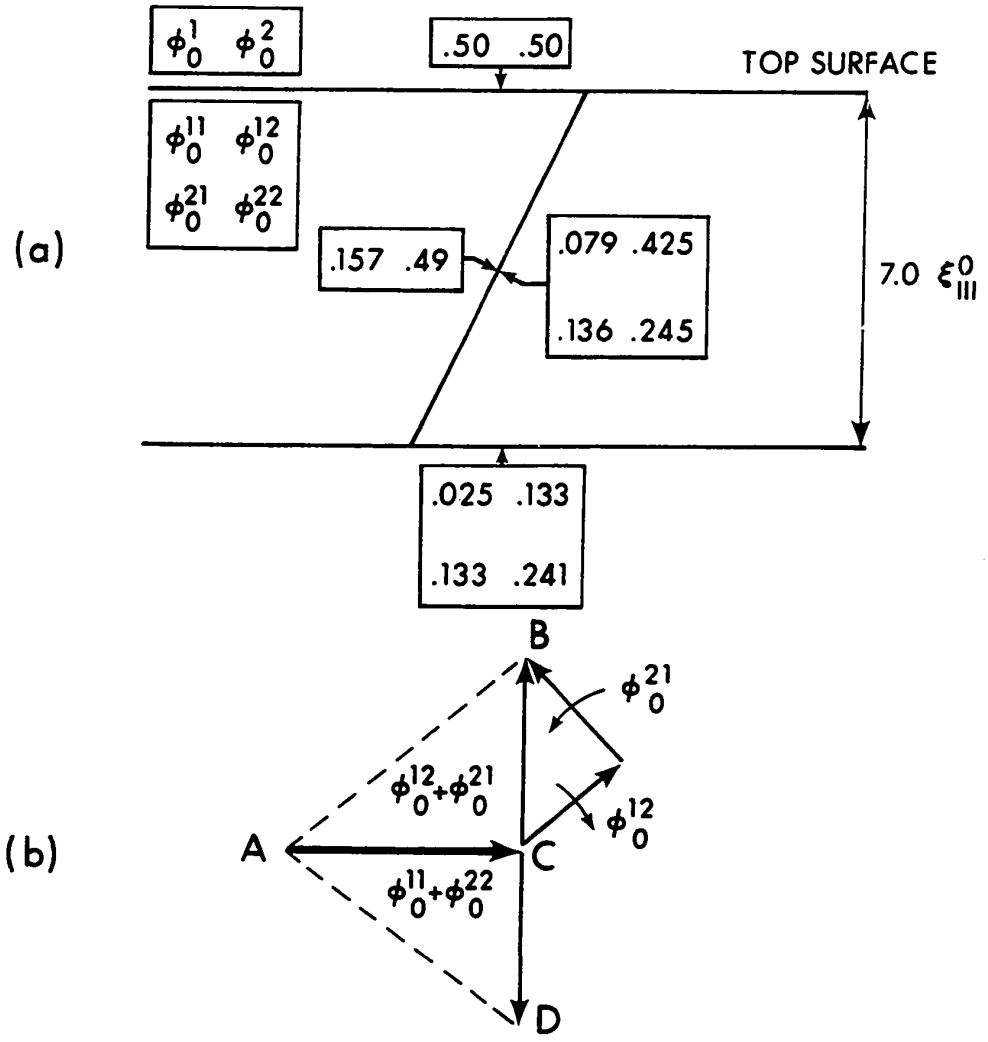

Fig. 19 Two beam analysis of the contrast of central fringes for an $\alpha=-2\pi/3$ stacking fault in fcc cobalt crystal of thickness equal to seven extinction distances. The calculations were carried out at 150 kV with $\Delta\theta_{111}=0$.

a) Magnitudes of ϕ_o^i and ϕ_o^{ij} relevant to a fault at the middle of the crystal.

b) Phase amplitude diagram showing the relation between the contribution of interbranch and intrabranch scattering to the amplitude of the directly transmitted beam.

middle of the crystal. This was done for the bright field image by calculating at the top surface and just above the fault the values of ϕ_o^1, ϕ_o^2, which are the contributions of Bloch waves 1 and 2 to the amplitude of the directly transmitted beam (see equation 4.1). The next step was to calculate the values of ϕ_o^{11}, ϕ_o^{22} and ϕ_o^{12}, ϕ_o^{21}, the contributions of intra- and interbranch scattering of the two Bloch waves considered to the amplitude of the directly transmitted beam (see equation 4.7). These contributions are calculated just below the fault and at the bottom surface of the crystal. All these calculations were performed by assuming the (111) reflection in fcc cobalt to satisfy the exact Bragg condition, at 150 kV.

5:3.1(a) Mechanism Responsible for Contrast in Crystals of Thickness n ξ_{111}^o

The manner in which central fringe contrast arises in crystals of thickness equal to n extinction distances can be seen when Fig.19 is considered. The results given in Fig. 19a were obtained by assuming a crystal of thickness 7.0 ξ_{111}^o containing an $\alpha = -2\pi/3$ stacking fault. The first point to note from Fig. 19a is that in contrast to the analysis given previously by Hirsch et.al. [71] and Hashimoto et.al. [15], the magnitudes of interbranch

contributions ϕ_o^{12}, ϕ_o^{21} to the directly transmitted beam amplitude at the bottom surface of the crystal are approximately equal. The physical reason for obtaining this result can be explained in the following manner. Since $q^1 >> q^2$, the contribution of Bloch wave 1 (ϕ_o^1) to the directly transmitted beam amplitude just above the fault is considerably smaller than that of Bloch wave 2 (ϕ_o^2). As these two Bloch waves encounter the fault intrabranch scattering of Bloch wave 1 giving rise to ϕ_o^{11}, and interbranch scattering from 1, resulting in ϕ_o^{21}, will be weak, while ϕ_o^{22} and ϕ_o^{12} will be strong. However, since ϕ_o^{12} is characterized by the absorption coefficient q^1, it will weaken considerably before reaching the bottom surface of the crystal whereas ϕ_o^{21} will not. Thus at the bottom surface of the crystal the two interbranch contributions ϕ_o^{12}, ϕ_o^{21} will be approximately equal.

In order to explain the nature of the resulting fringe contrast, the magnitudes as well as the phase angles of the different contributions have to be considered. This is done in the phase-amplitude diagram of Fig. 19b. From this figure it is seen,as noted in section 4:3, that the resultant contribution of intrabranch scattering to the amplitude of the directly transmitted beam does not vary with depth of fault in the crystal, while the resultant of interbranch

scattering does. As the depth of fault changes the vectors representing the interbranch contributions ϕ_o^{12}, ϕ_o^{21} rotate in the manner indicated so that the resultant interbranch contribution is always at right angles to that of intrabranch scattering. The vector representing the resultant interbranch contribution varies in magnitude from a maximum CB to zero to a maximum again CD in one half of the extinction distance. The resulting fringes will therefore be doublets since the total amplitude varies from a maximum AB to a minimum AC to a maximum again AD when stacking fault depth changes by one half of the extinction distance. Fig. 19b shows also that the relative magnitudes of the resultant of inter- and intrabranch scattering determines the difference between maximum amplitude (AB) and minimum amplitude (AC) and therefore determines the contrast. The reason for the relatively poor contrast observed in moderately thick crystals can be seen from table 1 which gives the magnitudes of AB (i.e. $|\phi_o^{11}| + |\phi_o^{22}|$) and AC (i.e. $|\phi_o^{12}| + |\phi_o^{21}|$) for crystals of different thicknesses in the range 4 to 10 ξ_{111}^o.

Table 1

n ξ^o_{111}	$\lvert\phi^{12}_o\rvert + \lvert\phi^{21}_o\rvert$	$\lvert\phi^{11}_o\rvert + \lvert\phi^{22}_o\rvert$
4	0.44	0.31
7	0.26	0.26
10	0.16	0.24

5:3.1(b) MECHANISM RESPONSIBLE FOR CENTRAL FRINGE CONTRAST IN CRYSTALS OF THICKNESS (n+½) ξ^o_{111}

In order to understand the mechanism responsible for central fringe contrast in crystals of thickness (n+½) extinction distances we consider the results of an analysis performed for a crystal of thickness 7½ ξ^o_{111}. From Fig. 20a it can be seen that the magnitudes of the different inter- and intrabranch contributions remain essentially the same as that presented in Fig. 19a for a crystal 7.0 extinction distances thick. However, Fig. 20b shows that the phase relationships are quite different. When crystal is (n+½) ξ^o_{111} the resultant interbranch term is always parallel (or antiparallel) to that resulting from intrabranch scattering. When the stacking fault depth varies, the total amplitude will thus change from a maximum AD (see Fig.

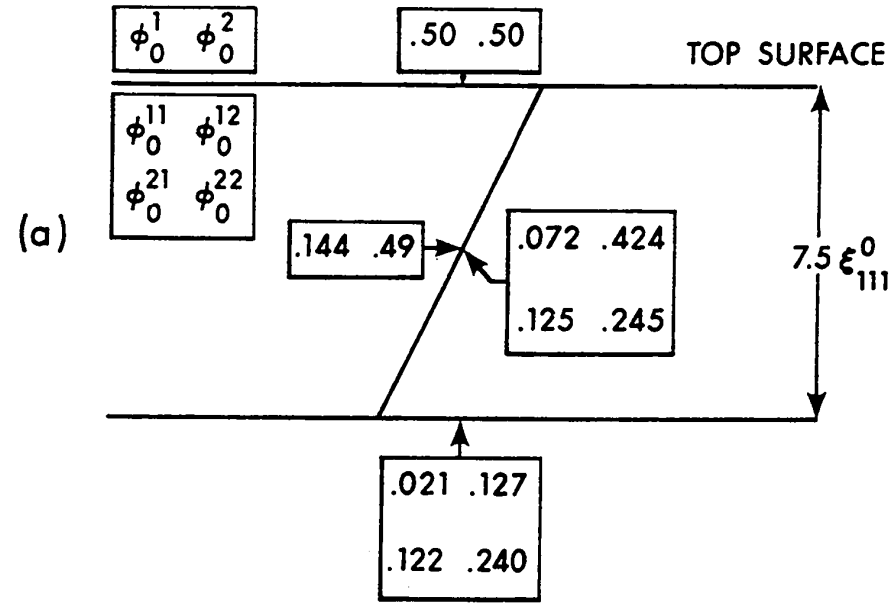

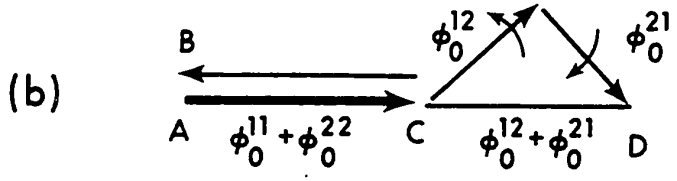

Fig. 20 Two beam analysis similar to that given in Fig. 19 but for a crystal of thickness 7.5 extinction distances.

20b) to a minimum AB in one half of the extinction distance. Fringes will therefore be singlets and the difference between maximum and minimum total amplitude, and therefore the contrast is considerably greater than that obtained in the case of a crystal of thickness $n\ \xi^{o}_{111}$.

5:3.2 MULTIBEAM EFFECTS ON THE CENTRAL FRINGE PATTERN

A multibeam analysis of the contrast of central fringes for a fault lying in a moderately thick crystal is not presented since it was found that the effects due to higher order Bloch waves were quite small and did not change the mechanisms discussed in sections 5:3.1(a), (b) which involved Bloch waves 1 and 2 only. However, when a thick crystal was considered effects due to Bloch waves 3, 4 were found to be important. This is discussed in the next section.

5:3.2(a) MULTIBEAM EFFECTS ON THE CENTRAL FRINGE PATTERN FOR A FAULT IN A THICK CRYSTAL

Although in the multibeam analysis of image contrast in thick crystals eleven systematic reflections, including $(\bar{5}\bar{5}\bar{5})$ ... (555) were taken into account, it was found that only interactions between Bloch waves 1, 2, 3, and 4 had to be considered. The contributions of

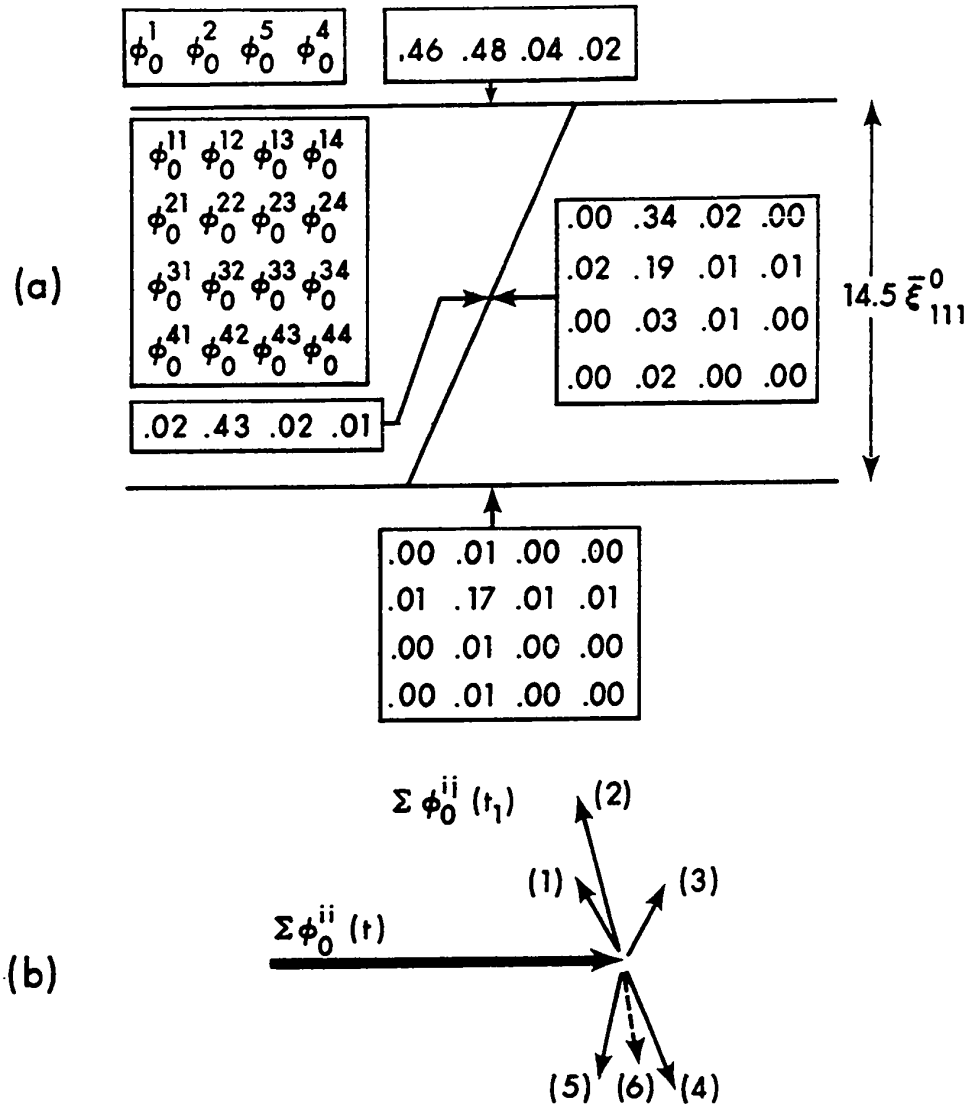

Fig. 21 Multibeam analysis of central fringe contrast for an $\alpha = -2\pi/3$ stacking fault in a crystal thickness $14.5\ \bar{\xi}^o_{111}$.

a) Magnitude of ϕ_o^i, ϕ_o^{ij} for a fault depth at the middle of the crystal.

b) Phase amplitude diagram showing the rotation of the resultant of interbranch scattering (vectors 1 to 6) around that of intrabranch scattering as the stacking fault depth changes from t/2 to $\frac{1}{2}(t + \bar{\xi}^o_{111})$.

higher order Bloch waves were quite small and were therefore ignored. The manner in which systematic reflections were found to affect fringe contrast for a stacking fault lying near the middle of a thick crystal can be seen from the results in Fig. 21. Fig. 21a gives the contributions of Bloch waves 1 to 4 to the amplitude of the directly transmitted beam in a faulted crystal of thickness 14.5 $\bar{\xi}^{o}_{111}$. From this figure it can be seen that at the bottom surface of the crystal the main contribution to the amplitude of the directly transmitted beam is from the intrabranch component ϕ^{22}_{o}. At first sight it might be concluded that all the other interbranch contributions can be neglected since they are small and hence will have no effect cn image contrast. However these conclusions cannot be correct since if all the interbranch contributions to the amplitude of the directly transmitted beam remain in phase their total magnitude would be about 1/3 of the contribution from intrabranch scattering ϕ^{22}_{o}. If this was so then fringes of higher contrast than observed would result on the basis of the mechanisms discussed in sections 5:3.1(a) and (b). It is therefore quite important to consider the phase relationships between the different interbranch contributions to the amplitude of the directly transmitted beam. These are illustrated in the phase-amplitude diagram in Fig. 21b

for fault depths near the centre of the fault. From this figure it can be seen that,unlike the situation discussed in section 5:3.1(b) of the two beam theory, the resultant of the interbranch contributions to the total amplitude is neither parallel nor antiparallel to the resultant intrabranch contribution. This point can be explained from equations 4.5 and 4.7. The individual interbranch components arising from the scattering transitions $(b^1 \rightleftharpoons b^2)$, $(b^2 \rightleftharpoons b^3)$, and $(b^2 \rightleftharpoons b^4)$ depend upon the phase terms exp $2\pi i(\gamma^1 - \gamma^2)t_1$, exp $2\pi i(\gamma^2 - \gamma^3)t_1$ and exp $2\pi i(\gamma^2 - \gamma^4)t_1$ respectively. Consequently as t_1 changes, the vectors representing those contributions will rotate through unequal phase angles, resulting in a complex change in the magnitude as well as phase angle of their resultant vector shown in Fig. 21b. The total directly transmitted beam amplitude will therefore depend on t_1 in a complex manner, which explains the reason for the presence of a central fringe pattern exhibiting complex periodicity. Since the two beam phase relationship given in section 5:3.1(b) is a requirement for optimum fringe contrast to be obtained, these results indicate that the effects of systematic reflections tend to reduce contrast of the central fringe pattern.

5:3.3 EFFECTS OF MULTIPLE REFLECTIONS ON THE CONTRAST OF STACKING FAULT FRINGES NEAR TO THE SURFACES OF THE CRYSTAL

The results in sections 5:2.1(b) and 5:3.2(a) have shown that in thick crystal systematic reflections have a deletarious effect on the contrast of stacking fault fringes for fault depths near the middle of the crystal. However, as noted in section 5:2.2, comparison of two and multibeam theoretical fault profiles with experiment has shown that the character of edge fringes is not affected by the presence of systematic reflections. This result can be understood by comparing the magnitudes of the inter- and intrabranch contributions of the important Bloch waves excited in the two and multibeam theories. These are given in Table 2 for two crystal thicknesses, 7.0 and 14.0 extinction distances. In each case, the stacking fault depth considered corresponds to the bottom surface of the crystal. The two beam results in Table 2 show that in both moderately thick and thick crystals good contrast should result, since the two important contributions to the total amplitude of directly transmitted beam ϕ_o^{12} (due to the transition $b^2 \rightarrow b^1$) and ϕ_o^{22} (due to intrabranch scattering of b^2) are of nearly equal magnitudes. It can also be seen from the results of

multibeam calculations that contributions due to Bloch waves 3 and 4 are considerably smaller than the two important contributions ϕ_o^{12}, ϕ_o^{22}. This indicates that the two beam approximation gives an adequate description of contrast of edge fringes. It should be noted that similar results to those discussed above were obtained when fault depths near the top surface of the crystal were considered although in this case image contrast arises from ϕ_o^{22} and ϕ_o^{21}.

Table 2

Crystal thickness in units of extinction distance	ϕ_o^{11} ϕ_o^{12} ϕ_o^{21} ϕ_o^{22}	ϕ_o^{11} ϕ_o^{12} ϕ_o^{13} ϕ_o^{14} ϕ_o^{21} ϕ_o^{22} ϕ_o^{23} ϕ_o^{24} ϕ_o^{31} ϕ_o^{32} ϕ_o^{33} ϕ_o^{34} ϕ_o^{41} ϕ_o^{42} ϕ_o^{43} ϕ_o^{44}
7.0	.025 .415 .043 .241	.00 .32 .02 .00 .01 .20 .01 .00 .00 .03 .01 .00 .00 .02 .00 .00
14.0	.002 .399 .004 .231	.00 .31 .00 .00 .00 .18 .00 .00 .00 .02 .00 .00 .00 .00 .00 .00

5:4 DISCUSSION

In section 5:3.2(a) it was shown that the (111) set of systematic reflections in fcc cobalt has a deleterious effect on the contrast of fringes at the centre of the fault. This fact suggests that if a systematic set can be chosen for which effects of multiple reflections are minimal, good contrast should be obtained in much thicker crystals than would otherwise be possible. In order to test this hypothesis two and multibeam calculations of stacking fault contrast were performed assuming that only the (220) set of systematic reflections was excited and that the (220) reflection was in the exact Bragg condition. The two and multibeam profiles obtained from these calculations were very similar to those shown in Fig. 15 and are therefore not reproduced. The results showed that fringes at the centre of a fault will exhibit relatively high contrast in crystals of thickness up to about 10.5 extinction distances. Since the (220) extinction distance is approximately 500 A° this indicates that good contrast should be obtained in crystals of about 5000 A° in thickness. For the (111) set of systematic reflections it was found that good contrast in crystals of thickness equal to $(n+\frac{1}{2})$ extinction distances did not persist beyond about 8.5 extinction distances. Since the (111) extinction

distance is about 250 A°, this result indicates that with the (111) set of systematic relfections excited, good contrast would not be obtained in crystals greater than around 2000 A°. These results are of particular interest in view of the work of Sheinin and Botros [42, 108] (see also section 6:5), that increased contrast in thick crystals results in better effective penetration. The above comparison of the contrast obtained when different systematic sets are excited therefore indicates that in choosing the conditions for obtaining optimum penetration, particular attention should be paid to the systematic row excited.

The last point to be discussed in this chapter is in regards to the dependence of the contrast of the outermost fringes in a stacking fault image on crystal thickness. The results given in section 5:2.2 indicated that for moderately thick crystals the visibility of the outermost fringes depended on whether the crystal thickness was n or $(n+\frac{1}{2})$ extinction distances while on the other hand, for thick crystals the visibility of those fringes became independent of crystal thickness. These results suggest that if the character of the outermost fringes is to be identified correctly for a fault lying in a moderately thick crystal, observations must be carried out by using a crystal of varying thickness. This point is of particular importance in view of the

work of Art, Gevers, and Amelinckx [109] who showed that identification of a fault as being intrinsic or extrinsic involves determination of the top and bottom surfaces of the crystal as well as the sign of the phase factor α. These two parameters are readily obtained if the character of the outermost fringes in both bright and dark field images can be correctly recognized.

5:5 SUMMARY AND CONCLUSIONS

The results of the present investigation have shown that stacking faults in moderately thick crystals of cobalt (thickness range from five to nine extinction distances) exhibit contrast of a two beam character when the (111) set of systematic reflections is excited. This contrast is characterized by the fact that fringes at the centre of faults in crystals n and $(n+\frac{1}{2})$ extinction distances thick exhibit a marked contrast difference. This result was explained in terms of inter- and intrabranch scattering of Bloch waves 1 and 2. It was found that crystal thickness, through the phase term $\exp 2\pi i\gamma^2 t_1$, acts like a phase factor which determines the phase relationship between the inter- and intrabranch components of the amplitudes of the diffracted beam. This relationship is critical in determining

contrast. In thicker crystals the effects of systematic reflections become important and central fringes exhibit weak contrast regardless of crystal thickness. The fringes at the edges of the fault, on the other hand, remain two beam in character for all values of crystal thickness investigated.

These results illustrate the following points: first that the (111) set of systematic reflections has a deleterious effect on the contrast of fringes in images of stacking faults in fcc cobalt. This is in contrast to results reported elsewhere [34] on the effects of systematic reflections on stacking fault contrast in gold. The second point to note from these results is that crystal thickness and defect depth are important factors in determining whether or not effects of the systematic reflections play an important role in determining image contrast. These factors are in addition to others such as accelerating voltage and crystal orientation which are to be discussed in Chapters 6, 7 and 8.

Finally it has been shown that the deleterious effects of systematic reflections on fringe contrast can be avoided if the (220) systematic set only is excited thus giving rise to strong contrast in much thicker crystals than would otherwise be possible.

CHAPTER 6

EFFECTS OF TILTING ON THE NATURE OF STACKING FAULT IMAGES OBTAINED AT LOW ACCELERATING VOLTAGE

6:1 INTRODUCTION

The recent work of Sheinin [42] has shown that significant changes take place in the character of thickness fringes observed in dark field images of wedge crystals when the crystal is tilted away from the orientation corresponding to $S_g = 0$ (g is the lowest order reflection in a systematic set). These changes were shown to be due to the differences in the Bloch wave excitations which occur as the crystal is tilted. Thus for example thickness fringe contrast was found to be considerably enhanced when the reflection 3g was close to the Bragg condition. This enhanced contrast occurred due to the strong channeling of Bloch waves 2 and 4 which are equally excited at this orientation. These results suggest that significant changes might also occur for stacking fault contrast if the crystal is tilted away from the orientation corresponding to $S_g = 0$. The work to be presented in this chapter was undertaken with a view to exploring the nature of these changes.

In investigations of fault contrast as function of S_g, it is desirable that observations be carried out

for different types of faults over a range of crystal thicknesses. This was done, as described in Chapter 5, by using wedge crystals of cobalt. Bright and dark field observations were carried out for values of $\Delta\theta_g$ in the range -1.0 θ_g up to about 2.2 θ_g. These results are presented in section 6:2. In the following section, 6:3, the experimental results are compared to computer calculations of image contrast based on the dynamical theory. Next a discussion of the results in terms of the scattering mechanisms responsible for producing image contrast is given in section 6:5. The last point to be considered in this chapter (see section 6:6) is an examination of the implications of the results obtained in maximizing stacking fault contrast in thick crystals (referred to as stacking fault penetration).

6:2 EXPERIMENTAL RESULTS

Observations of bright and dark field images of stacking faults have been carried out near the symmetry orientation and at values of $\Delta\theta_g$ for which the reflections g, 2g, and 3g were close to the Bragg condition. The change in image contrast which occurred as the specimen was tilted to each of these orientations is illustrated by the densitometer traces in Fig. 22. These results were obtained when the (111) set of systematic reflections in fcc cobalt was excited and at

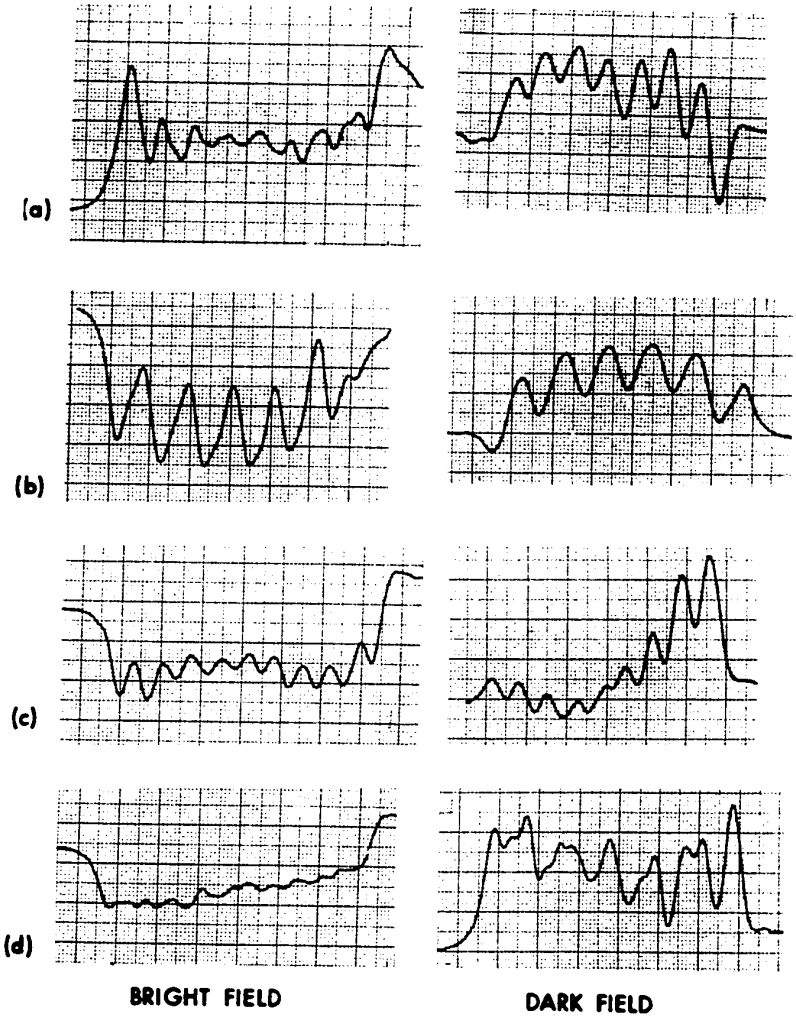

Fig. 22 Densitometer traces obtained from bright and dark micrographs of an $\alpha = -2\pi/3$ fault in fcc cobalt. The (111) set of systematic reflections was excited at 150 kV and the crystal thickness at which the traces were obtained was 1500 A°. The trace in a) was obtained just inside the symmetry position while b), c), and d) were obtained when the reflections g, 2g, 3g respectively were close to their Bragg condition.

an accelerating voltage of 150 kV. The crystal thickness at which these profiles were recorded was 6.0 extinction distances (referred to the extinction distance at $\Delta\theta_g$ = 0.0). It is important however to mention that similar results were obtained when other crystal thicknesses were explored.

It can be seen from Fig. 22b that optimum contrast in the bright field is obtained when the reflection g was close to the Bragg condition. Fig. 22a shows that as the specimen was tilted toward the symmetry position the bright field contrast became weaker, although fringes could still be resolved at this orientation. For increasing positive values for $\Delta\theta_g$, the fringe contrast in the bright field became progressively weaker as is illustrated by the microdensitometer traces in Fig. 22c, d. Fig. 22d, for example, shows that when the crystal was tilted so that the reflection 3g was close to its Bragg condition, contrast in the bright field has decreased to the extent that stacking fault fringes can barely be detected. It should be noted that for all stacking faults observed in both fcc and hcp cobalt, the variation of contrast in the bright field with angle of tilt of the crystal was similar to that shown in Fig. 22. In comparing various sets of results with those illustrated in Fig. 22, however, differences in how rapidly the fringe contrast disappeared with increasing values of

$\Delta\theta_g$ were noted. Thus for example, in the case of the (200) systematic set of reflections in fcc cobalt, fringes could no longer be detected when the reflection (600) was near the Bragg condition, although some residual contrast indicating the presence of the fault still remained. For the (112) systematic set in hcp cobalt, on the other hand, even this residual contrast was absent with the result that, at this orientation, the presence of the stacking fault could not be detected in the bright field image.

The dark field results which are shown in Fig. 22 indicate that the variation of contrast with $\Delta\theta_g$ is considerably different from that obtained in the bright field. Fig. 22b shows that, as in the bright field, good contrast is obtained when the reflection g is close to the Bragg condition. As the specimen is tilted away from this orientation, however, contrast in the dark field does not decrease in the same way as is the case in the bright field. This is illustrated by comparing the bright and dark field profiles given in Fig. 22d obtained when the reflection 3g was close to the Bragg condition. As can be seen, excellent contrast is obtained in the dark field whereas, as previously noted, stacking fault fringes at this orientation can barely be detected in the bright field. This wide difference between the contrast

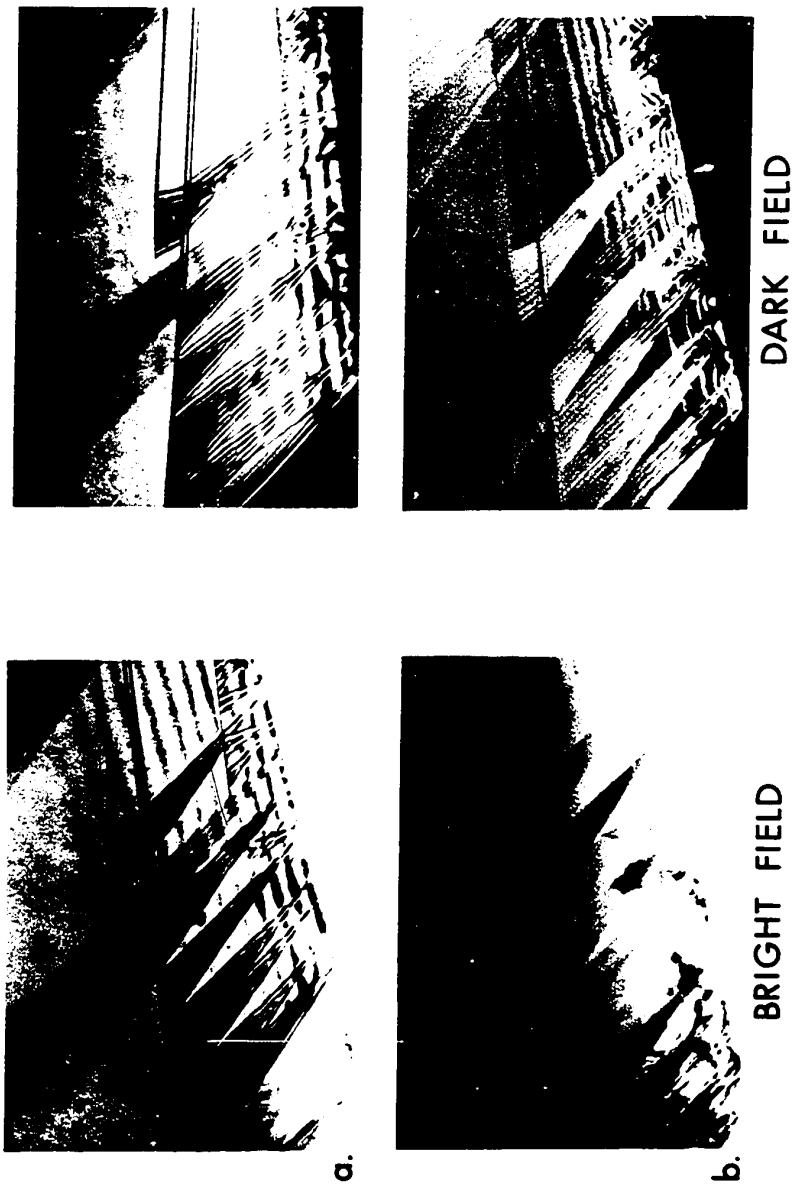

Fig. 23 Micrographs from which microdensitometer traces like those given in Fig. 22 b, d were obtained.

in bright and dark field images of stacking faults which occurs as the specimen is tilted away from the reflection g in the Bragg condition is graphically illustrated by the micrographs given in Fig. 23. It should be noted that for all stacking faults observed in both fcc and hcp cobalt, this wide difference in contrast between dark and bright field was found.

6:3 COMPARISON BETWEEN THEORY AND EXPERIMENT

In order to determine whether or not the differences found between bright and dark field images of stacking faults can be accounted for by the dynamical theory, calculations of contrast were performed for diffferent values of $\Delta\theta_g$ in the range -1.0 θ_g up to 2.2 θ_g. Both the two and multibeam theories were employed in these calculations and different systematic sets of reflections were considered. In the multibeam calculations twelve systematic reflections including the reflections 7g, ..., -4g were considered and the calculations were performed for an accelerating voltage of 150 kV. From these calculations it was found that good agreement with experimental results can only be obtained by employing the multibeam theory. The multibeam results corresponding to the experimental profiles of Fig. 22 are presented in Fig. 24. This figure shows,

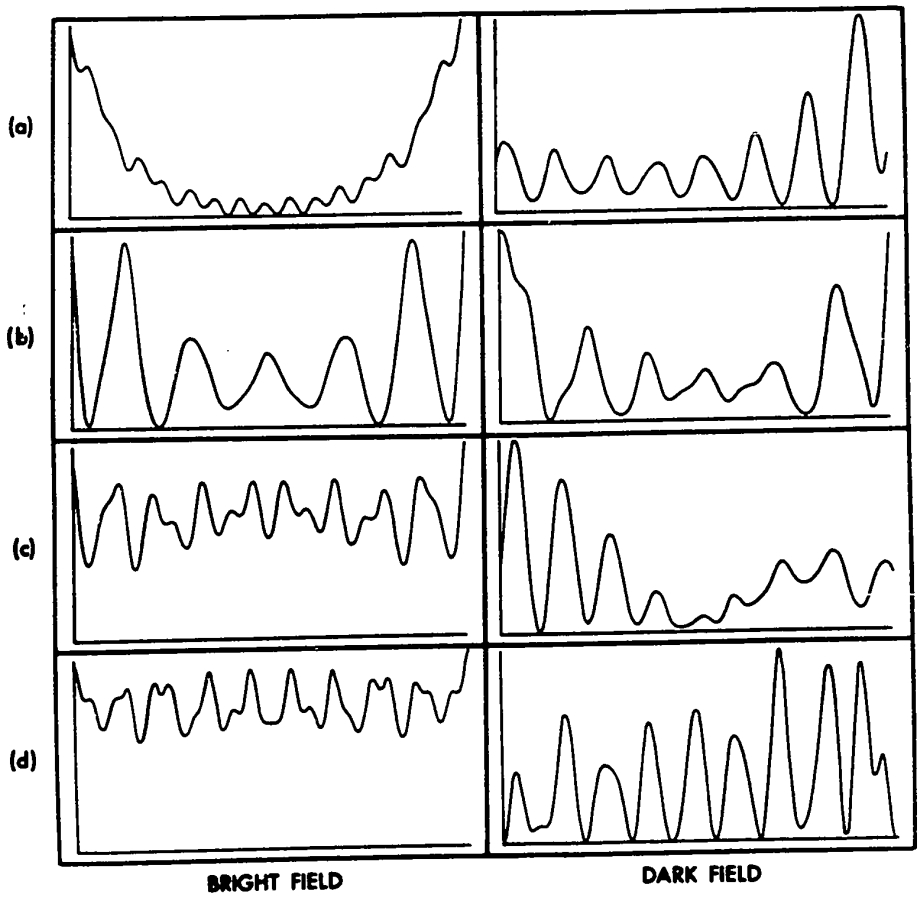

Fig. 24 Theoretical multibeam intensity profiles for an $\alpha = -2\pi/3$ stacking fault in fcc cobalt crystal of thickness 1500 A°. a) to d) are calculated for the same diffraction conditions used in obtaining the experimental traces in Fig. 22.

in good agreement with experimental results in Fig. 22, that there is a marked decrease in bright field contrast as the crystal is tilted from the Bragg condition of the reflection g, while under the same circumstances good contrast is retained in the dark field image. It should be mentioned, however, that when the multibeam calculations were repeated for other values of crystal thickness, similar results to those shown in Fig. 24 were obtained.

6:4 EXPLANATION OF THE DIFFERENCES BETWEEN BRIGHT AND DARK FIELD IMAGES

Insight into the physical reasons for the differences in behaviour between bright and dark field images of stacking faults can be gained by analyzing each image in terms of the relevant Bloch wave interactions. This analysis was carried out in a manner analogous to that mentioned in Chapter 5 by following the Bloch wave interactions from the top to the bottom surfaces of the crystal. This was done by calculating the values of pertinent Bloch wave contributions ϕ_g^i at the top surface and just above the fault as well as the values of ϕ_g^{ij}'s just below the fault and at the bottom surface of the crystal. The results given in sections 6:4.1, 6:4.2 were obtained by assuming in the calculation that the (111)

set of systematic reflections in fcc cobalt was excited at 150 kV, with the value of $\Delta\theta_g = 2.2\ \theta_{111}$. In these results only interactions between Bloch waves 1, 2, and 4 are included since all the other Bloch wave interactions were small and could be neglected. The reason for ignoring an analysis which employs the two beam theory, as noted in section 6:3, was that better agreement between theory and experiment was obtained by including effects of systematic reflections in the calculation.

6:4.1 ANALYSIS OF BRIGHT FIELD IMAGE AT LARGE DEVIATIONS

The reason for the poor contrast exhibited by bright field stacking fault image at large deviations can be seen by considering Fig. 25. This figure gives the important Bloch wave contributions to the amplitude of the directly transmitted beam for an $\alpha = -2\pi/3$ fault lying at the middle of the crystal. It can be seen from the figure that at the top surface of the crystal Bloch wave 4 is strongly excited and that other Bloch waves are of negligible importance. Thus it is mainly Bloch wave 4 which will be incident on the fault. The only scattering which can occur as this Bloch wave encounters the stacking fault will be due to the scattering of Bloch wave 4 into itself (i.e., an intrabranch transition).

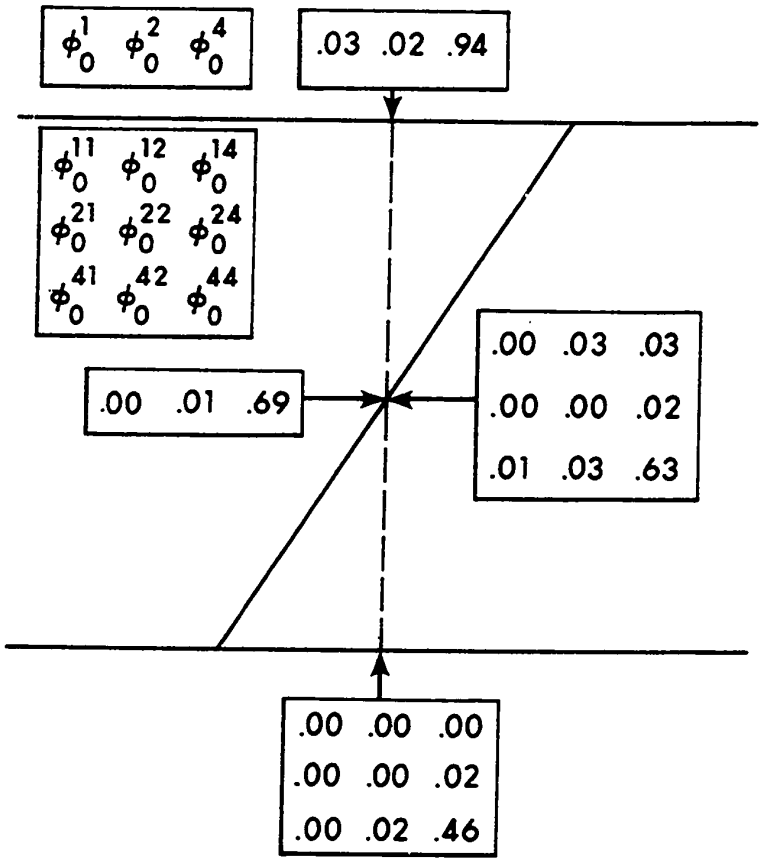

Fig. 25 The values of ϕ_o^i and ϕ_o^{ij} for an $\alpha = -2\pi/3$ stacking fault in an fcc cobalt crystal of thickness 1500 A°. It was assumed that the (111) set of systematic reflections was excited at 150 kV with $\Delta\theta_{111} = 2.2\ \theta_{111}$.

That this is so can be seen from Fig. 25 by comparing the magnitude of ϕ_o^{44} to the other inter- or intrabranch contributions. At the bottom surface of the crystal the only contribution to the directly transmitted beam amplitude will therefore be due to ϕ_o^{44}. Since the value of intrabranch scattering is independent of the fault depth t_1 (see equation 4.7) the total amplitude of the directly transmitted beam will remain essentially constant at the bottom surface and thus poor contrast results.

6:4.2 ANALYSIS OF DARK FIELD IMAGE AT $\Delta\theta_{111} = 2.2\ \theta_{111}$ FOR DEVIATIONS OUTSIDE THE REFLECTION 3g IN THE BRAGG CONDITION

At crystal orientations corresponding to the reflection 3g outside the Bragg condition, dark field images of stacking faults were found, as noted in section 6:2, to exhibit fringes of high contrast. An additional feature of the stacking fault image at this orientation is its relative insensitivity to small variations in crystal thickness. This feature can be seen by comparing the dark field micrographs given in Fig. 23. In the analysis of image contrast to be presented in this section an attempt will be made to explain the above results.

In order to illustrate the reason for the good contrast obtained at $\Delta\theta_{111} = 2.2\ \theta_{111}$ Bloch wave interactions are followed down through the crystal for a fault depth near the middle of the crystal. These Bloch wave interactions can be seen by considering Fig. 26. As can be seen from this figure the three Bloch waves 1, 2, and 4 give important contributions to the amplitude of the diffracted beam at the top surface of the crystal. However since $q^1 >> q^2 \sim q^4$, the contribution of Bloch wave 1 will decrease in comparison to that of Bloch waves 2 and 4 just above the fault. As these Bloch waves encounter the stacking fault the interbranch transitions $b^2 \rightarrow b^1$, $b^4 \rightarrow b^1$ give rise to ϕ_g^{12} and ϕ_g^{14} respectively, while the transition $b^4 \rightleftharpoons b^2$ results in the components ϕ_g^{24} and ϕ_g^{42}. On the other hand, the only important intrabranch transitions are those of Bloch waves 2 and 4 which give rise to the components ϕ_g^{22} and ϕ_g^{44} respectively. The relative magnitudes of the different inter- and intrabranch contributions to the amplitude of the diffracted beam will change before reaching the bottom surface of the crystal due to differences in absorption coefficients. This can be seen from Fig. 26 by noting that the magnitudes of ϕ_g^{12} and ϕ_g^{14} are relatively small at the bottom surface of the crystal. It can also be seen from Fig. 26 that, to

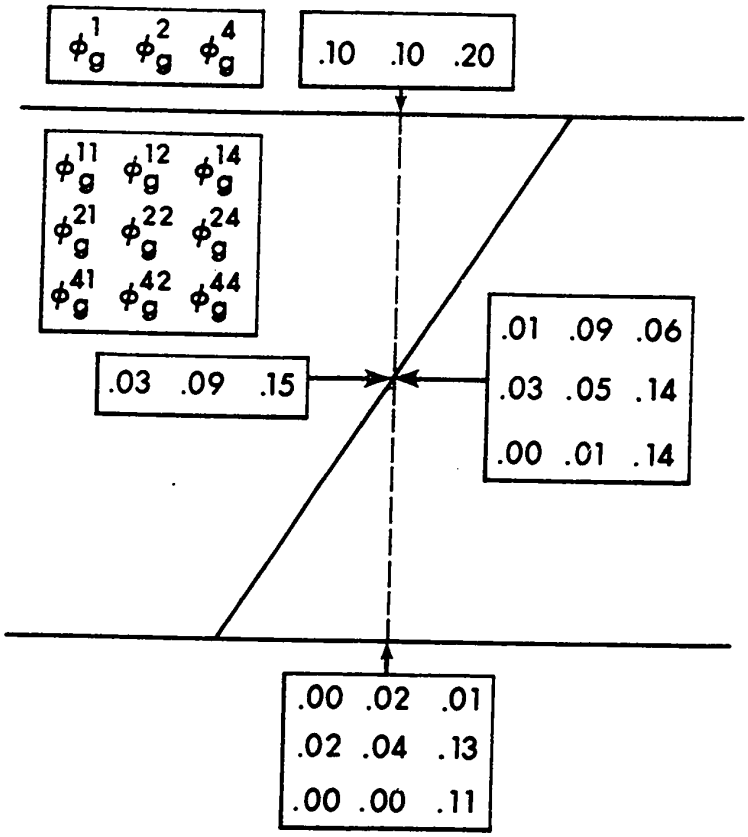

Fig. 26 The values of ϕ_g^i and ϕ_g^{ij} for an $\alpha = -2\pi/3$ stacking fault in an fcc cobalt crystal of thickness 1500 A°. It was assumed that the (111) set of systematic reflections was excited at 150 kV, with $\Delta\theta_{111} = 2.2\ \theta_{111}$.

a good approximation, the main contribution to the total diffracted beam amplitude is due to ϕ_g^{44} and ϕ_g^{24}. In fact the main reason for obtaining good contrast can be explained in terms of these two components. The explanation for this lies in the fact that the magnitudes of these two components are approximately equal. Thus when stacking fault depth changes, the vector representing ϕ_g^{24} in a phase amplitude diagram will rotate around the vector ϕ_g^{44} which is stationary since it is an intrabranch contribution. A complete rotation of ϕ_g^{24} can be seen to occur as the depth of fault changes by $1/\gamma^2 - \gamma^4$, the effective extinction distance. As a result the total amplitude will change from a maximum ($\sim|\phi_g^{24}| + |\phi_g^{44}|$) to a minimum ($\sim|\phi_g^{24}| - |\phi_g^{44}|$) to a maximum again. The resulting fringes will be singlets which exhibit high contrast, due to the large differences between maximum and minimum amplitudes. The differences in detail between stacking fault fringes shown in Fig. 24d, which exhibit some degree of complexity, and the above arguments can be accounted for by considering the other small contributions ϕ_g^{12}, ϕ_g^{14}, ϕ_g^{21}, ϕ_g^{22} which have been neglected in the above discussion.

It is next of interest to gain some understanding of the reasons why image contrast is relatively insensitive to small variations of crystal thickness. The way

in which contrast analyses were carried out for this case was to increase crystal thickness by regular increments and to repeat, in each case, calculations similar to those presented in Fig. 26. The results of these calculations have shown that for variations of crystal thickness in the range of an effective extinction distance, the magnitudes of the inter- and intrabranch contributions given in Fig. 26 remained essentially unchanged. The only differences which occurred were in the values of phase angles of the different inter- and intrabranch contributions to the diffracted beam amplitude. These results therefore show that at a new crystal thickness image contrast again essentially arises from the rotation of ϕ_g^{24} around ϕ_g^{44} in a phase amplitude diagram. Image contrast will therefore remain high and independent of the value of crystal thickness.

6:5 CONDITIONS FOR OBTAINING OPTIMUM PENETRATION FOR STACKING FAULTS

The effective penetration obtained in electron microscopy of thin crystals is defined as the maximum crystal thickness in which electron microscope observations of lattice defects can be made. Up to the present, investigations of penetration [15,46] have been concerned

primarily with the diffraction conditions for which maximum diffracted beam intensity is obtained. This intensity information, in the case of perfect crystals, is normally presented in a form of rocking curves which are plots of diffracted beam intensity at the bottom surface of a crystal of constant thickness as function of $\Delta\theta_g$. The diffraction conditions for maximum penetration, as deduced from these rocking curves, are the values of $\Delta\theta_g$ for which maximum intensity is diffracted through the crystal. At low accelerating voltages rocking curves normally show that maximum in directly transmitted and diffracted beam intensities occurs when the values of $\Delta\theta_g$ are close to zero. The work of Sheinin [42] on the other hand, has shown that these values of $\Delta\theta_g$ do not necessarily give the maximum thickness of crystal in which thickness fringes can be observed. His results raised the possibility that effective penetration obtained in observations of lattice defects might also be different from that indicated on the basis of rocking curve considerations alone. In order to explore this possibility in the stacking fault case, it was decided to examine the diffraction conditions which give rise to good fault penetration in more detail. This point is of considerable interest to the electron microscopist who is concerned with observing

defects in thick crystals where their properties and interactions can be more easily related to what happens in bulk material.

The effective stacking fault penetration has been determined experimentally by examining stacking faults in wedge crystals of cobalt. Observations were carried out at an accelerating voltage of 150 kV and over a wide range of $\Delta\theta_g$. In these experiments only uniform wedges containing stacking faults were considered, the reason being that under these conditions relative values of crystal thickness can easily be determined from measurements of the appropriate distances from the edge of the specimen. For a fault lying in a crystal wedge which is oriented to a given value of $\Delta\theta_g$, several micrographs were recorded with progressively increasing exposure time. Observations of penetration were only carried out when it was found that increasing exposure time did not change the visibility of the fault in thicker parts of the wedge.

The bright and dark field results of fault penetration obtained when the (111) set of systematic reflections was excited in fcc cobalt are illustrated in Fig. 27. Figs. 27a, c show that when the crystal is tilted from a value of $\Delta\theta_{111}{\sim}0$ to $\Delta\theta_{111}{\sim}2\theta_{111}$, a marked decrease in fault penetration in the bright field occurs. This can be seen by comparing the maximum crystal thicknesses in

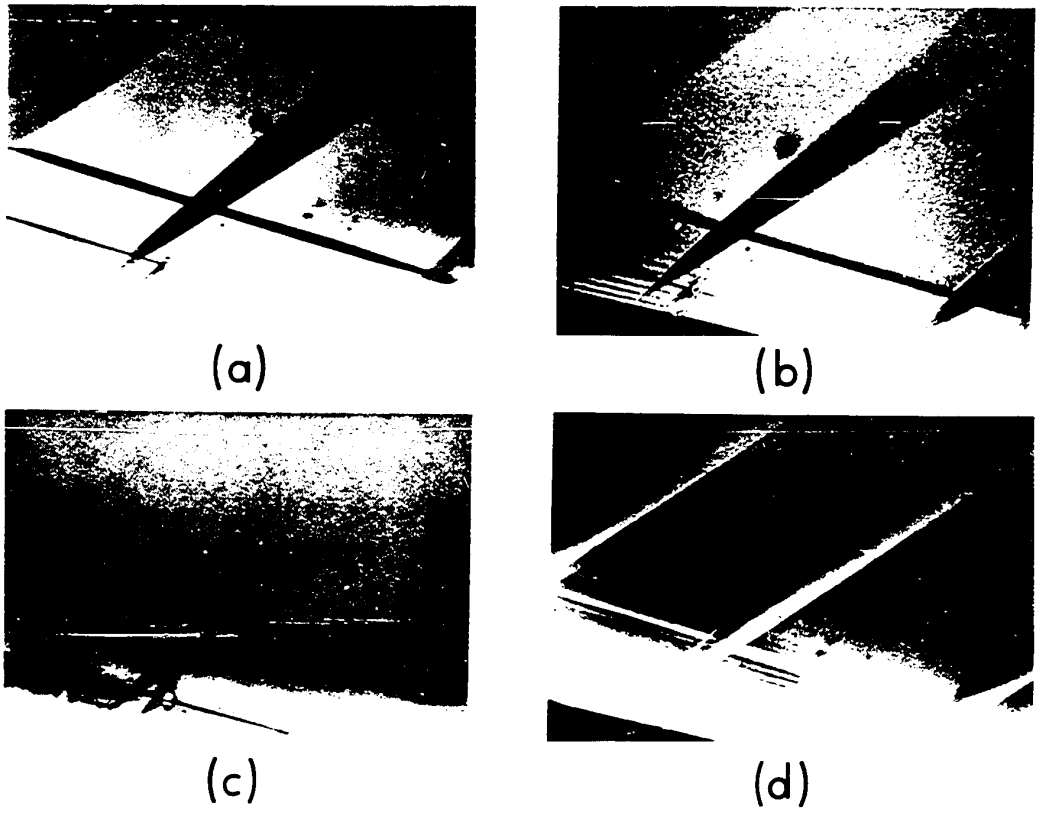

Fig. 27 Micrographs of stacking faults in a wedge crystal of fcc cobalt imaged at 150 kV. a) is a bright field image at $\Delta\theta_{111} \sim 0$, and b) is the corresponding dark field image; c) is the bright field image for $\Delta\theta_{111} \sim 2\ \theta_{111}$, and d) is the corresponding dark field image.

Figs. 27a,c for which good stacking fault image is observed. It is interesting to note that these bright field results are consistent with inferences which can be made from the bright field rocking curve given in Fig. 28a. This figure shows that directly transmitted intensity decreases when the crystal is tilted from $\Delta\theta_{111} \sim 0$ to $\Delta\theta_{111} \sim 2\ \theta_{111}$. The results of stacking fault penetration in the dark field for the same range of angles of tilt were found to be quite different. This can be seen by comparing the dark field micrographs given in Figs. 27b, d. From these micrographs it is clear that the maximum value of crystal thickness in which the stacking fault can be observed is roughly the same for $\Delta\theta_{111} \sim 0$ and $\Delta\theta_{111} \sim 2\ \theta_{111}$. Therefore fault penetration at both these orientations is almost the same. These dark field results are, however, not consistent with the information obtained from the dark field rocking curve shown in Fig. 28b which indicates a marked drop in diffracted beam intensity when the crystal is tilted away from the Bragg condition of the (111) reflection. It is important to mention that similar results to those presented above were obtained when other systematic sets of reflections were explored.

The difference in effective stacking fault penetration shown in Figs. 27c and d can be understood if

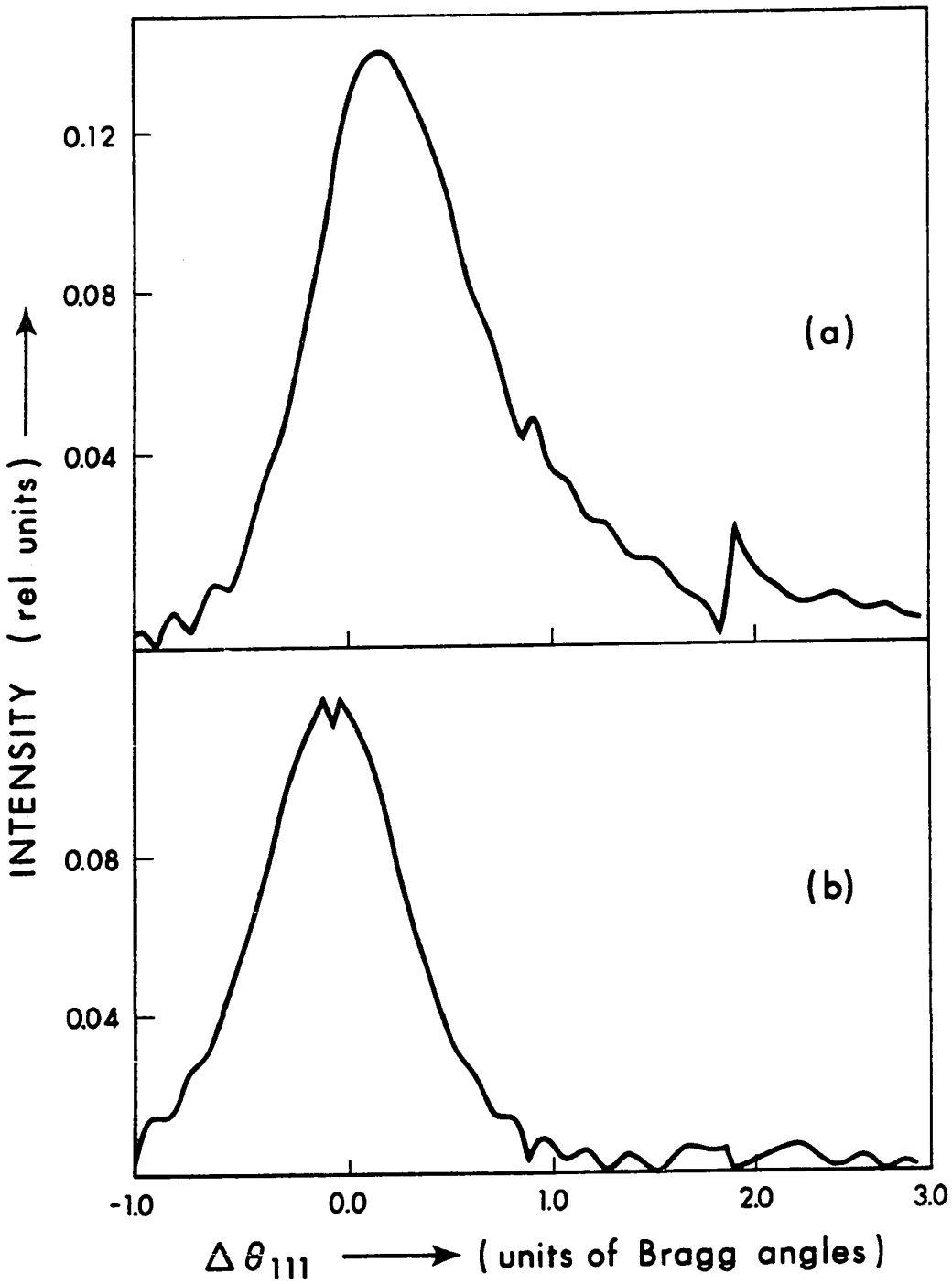

Fig. 28 Bright and dark field rocking curves for an fcc cobalt crystal of thickness 5000 A°. The (111) set of systematic reflections was assumed excited at 150 kV.

image contrast in the two cases is compared. As mentioned in section 6:2 of this chapter, only weak fringe contrast was detected when $\Delta\theta_{111} \sim 2\,\theta_{111}$ and the bright field image was considered, whereas under the same conditions the dark field image exhibited excellent contrast. It may therefore be concluded that investigations of the diffraction conditions for obtaining maximum fault penetration should not be based on intensity considerations alone, but should also take into account the effects associated with image contrast.

6:6 DISCUSSION

The results presented in this chapter indicate that the effects of systematic reflections on stacking fault images change appreciably as a result of crystal tilting. These effects were also found to be different depending on whether the stacking fault is imaged in the bright or dark field. This point is evidenced, as noted in section 6:2, by the similarity of bright and dark field image contrast when a low order reflection g was close to its Bragg condition and the wide differences in bright and dark field contrast obtained at orientations corresponding to the reflection 3g close to its Bragg condition.

The physical reasons for obtaining these results are associated with the changes which occur in Bloch wave

excitations as the crystal is tilted. Near the Bragg condition of a low order reflection Bloch waves 1 and 2 have nearly equal excitation amplitudes ($C_o^1 \sim C_o^2$), and since the Fourier coefficients $C_g^1 \sim C_g^2$ are also nearly equal, these Bloch waves will give equal contribution to both directly transmitted and diffracted beam amplitudes. Consequently bright and dark field contrast is similar. On the other hand, when the reflection 3g is close to its Bragg condition, only one Bloch wave (Bloch wave 4) has a high value of excitation amplitude C_o^4. This Bloch wave will be the only one which gives contribution to directly transmitted beam amplitude. Poor bright field contrast results according to the mechanism discussed in section 6:4.1. In the dark field $C_g^1 \sim C_g^2 >> C_g^4$, and thus at the top surface of the crystal three Bloch waves, namly 1, 2, and 4 will have important contributions $\phi_g^1 \sim \phi_g^2 \sim \phi_g^4$. Strong contrast results in the dark field image according to the scattering mechanism discussed in section 6:5.2.

The difference in contrast between bright and dark field images of stacking faults is of interest from a practical view point. Because of the limited range of orientations for which good contrast can be obtained in the bright field, observations of stacking faults must

be normally made for values of $\Delta\theta_g$ close to zero. This often presents a practical difficulty in that many specimens are bent to a certain extent so that, as the specimen is traversed in the microscope, it must be continuously re-oriented or the presence of the defect may remain undetected. The results of the present investigation indicate, however, that those observations would be more easily performed in the dark field since good stacking fault contrast is maintained over a considerably wider range of orientation.

6:7 SUMMARY AND CONCLUSIONS

The behaviour of stacking fault contrast as the crystal was tilted showed a marked difference between bright and dark field images. Near the Bragg orientation of a low order reflection good contrast was obtained both in the bright and dark field images of stacking faults. As the crystal was tilted to orientations where the reflection 3g was close to its Bragg conditions, very weak contrast was observed in the bright field while excellent contrast was retained in the dark field. An explanation of these differences between bright and dark field contrast has been given in terms of the scattering mechanisms of the important Bloch waves which give rise to contrast in each image.

Finally, it has been shown that the maximum value of crystal thickness in which good stacking fault image is observed in the bright field decreases sharply as the crystal is tilted away from the Bragg orientation of a low order reflection. A similar decrease did not occur when the dark field image was considered.

These results illustrate the following points: First, crystal orientation is an important factor which determines the effects of systematic reflections on stacking fault image. Image contrast can be increased or decreased as a result of tilting away from strong beam diffraction conditions depending whether the image considered is bright or dark field. Secondly, the ability to observe stacking faults in thick crystals does not depend on image intensity alone, as was considered to be the case in previous work [15,46], but is also influenced by effects associated with image contrast.

CHAPTER 7

ON THE NATURE OF STACKING FAULT IMAGES OBTAINED UNDER WEAK BEAM DIFFRACTION CONDITIONS

7:1 INTRODUCTION

There is considerable current interest in the applications of the weak beam technique of transmission electron microscopy in the study of lattice defects in crystalline matter (see for example Cockayne et.al. [43] for studies of dislocation partials and Haüssermann [110] for studies of defect clusters). However, little attention has been given to the stacking fault images obtained under these diffraction conditions. The work presented in this chapter was carried out with a view to exploring the nature of diffraction contrast from stacking faults imaged under weak beam diffraction conditions. The nature of the image obtained is discussed in sections 7:4 and 7:5, and the mechanisms responsible for producing image contrast are discussed in section 7:6.

7:2 WEAK BEAM DIFFRACTION CONDITIONS

For a particular row of systematic reflections, Cockayne [111] has defined weak beam diffraction conditions in terms of the dimensionless parameter $|w|=|\xi_g^o s_g|$.

Two conditions are required, namely

(a) $|s_g| \geq 10^{-2}$

and (b) $|w| \geq 5$.

For the case of the (111) set of systematic reflections in fcc cobalt, excited at 150 kV, these conditions correspond to values of $\Delta\theta_{111} \geq 3.2\ \theta_{111}$, i.e. setting the crystal at an orientation between the (444) and (555) reflections in the Bragg condition.

7:3 EXPERIMENTAL PROCEDURE

The method used to study different stacking fault images at values of $\Delta\theta_g$ corresponding to weak beam diffraction conditions was similar to that described in Chapter 6. Wedge crystals were used in order that stacking fault contrast could be observed over a range of crystal thicknesses. For the case of the (111) systematic set in fcc cobalt, the specimens were tilted to values of $\Delta\theta_{111}$ in the range $3.2\ \theta_{111}$ to $3.8\ \theta_{111}$. Observations were carried out at 150 kV and images were recorded after appropriately tilting the illumination in order to obtain high resolution dark field micrographs.

7:4 EXPERIMENTAL RESULTS

The images obtained by the procedure outlined above showed that at certain values of crystal thickness stacking fault images exhibit very strong fringe contrast while at other values of crystal thickness very weak contrast is observed. This marked difference in image contrast is illustrated in Fig. 29. It can be seen from this figure that the variation of stacking fault contrast with crystal thickness is periodic in nature with changes from strong to weak to strong contrast occurring when the crystal thickness changes by an amount equal to $\bar{\xi}^{\Delta}_{111}$, the effective extinction distance at the value of $\Delta\theta_{111}$ concerned.

Several other interesting contrast features can be seen from the stacking fault image in Fig. 29. The first of these is that the fringes are singlets rather than doublets (i.e. the fringe spacing is $\bar{\xi}^{\Delta}_{111}$ rather than $\frac{1}{2}\,\bar{\xi}^{\Delta}_{111}$). This can be determined from the fact that a change of one in the number of stacking fault fringes occurs when the crystal thickness changes by one effective extinction distance. This was also verified by the observation that the image of a stacking fault in a crystal of thickness equal to $n\bar{\xi}^{\Delta}_{111}$ contains n fringes. The next point of interest that can be seen from Fig. 29 is that fringe contrast does not appear to depend on the

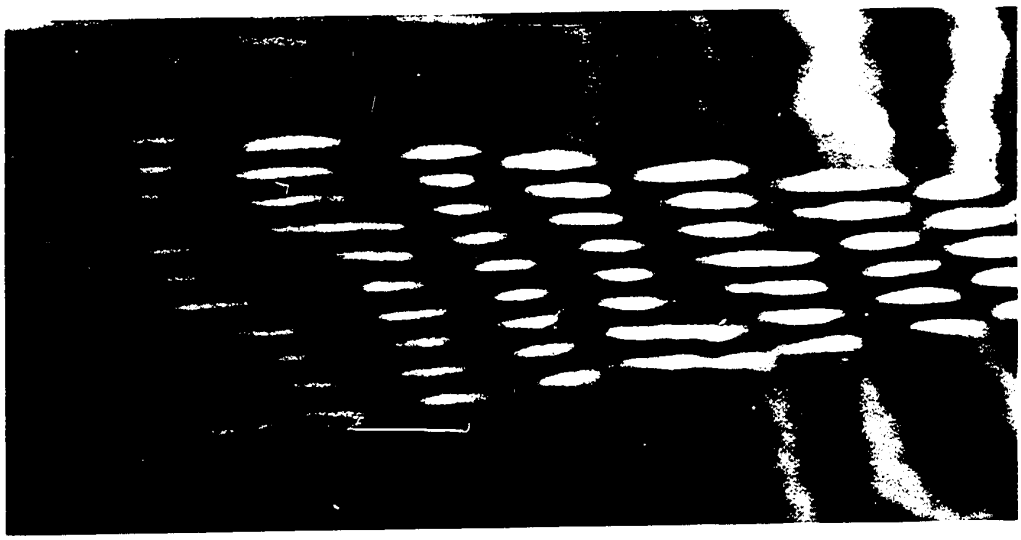

Fig. 29 Dark field micrograph for an $\alpha = 2\pi/3$ stacking fault image at 150 kV under weak beam diffraction conditions ($\Delta\theta_{111} = 3.2\ \theta_{111}$).

depth of the fault in the crystal. This is evidenced by the fact that no change in the visibility of the fringes across the fault can be observed. Finally Fig. 29 shows that the dark field images are symmetrical with respect to the centre of the fault. It should be noted that all the characteristics of stacking fault contrast described above were observed in both thin and relatively thick crystals and were found to persist up to the maximum value of crystal thickness investigated of about $15\bar{\xi}^{\Delta}_{111}$.

7:5 COMPARISON OF EXPERIMENTAL RESULTS WITH MULTIBEAM DYNAMICAL THEORY

Many beam theoretical calculations of stacking fault contrast were performed by including the fifteen systematic reflections $(\bar{5}\bar{5}\bar{5})...(999)$. The acclerating voltage was taken to be 150 kV. Fig. 30 shows the (111) dark field profiles for an $\alpha = 2\pi/3$ fault obtained for crystal thicknesses of 10, 10.5 and $11\bar{\xi}^{\Delta}_{111}$ respectively and a value of $\Delta\theta_{111} = 3.2\ \theta_{111}$. It can be seen from these results that a periodic variation in contrast from strong to weak to strong again occurs when the crystal thickness changes by one extinction distance. It can also be seen from the profiles in Figs. 30 a,c

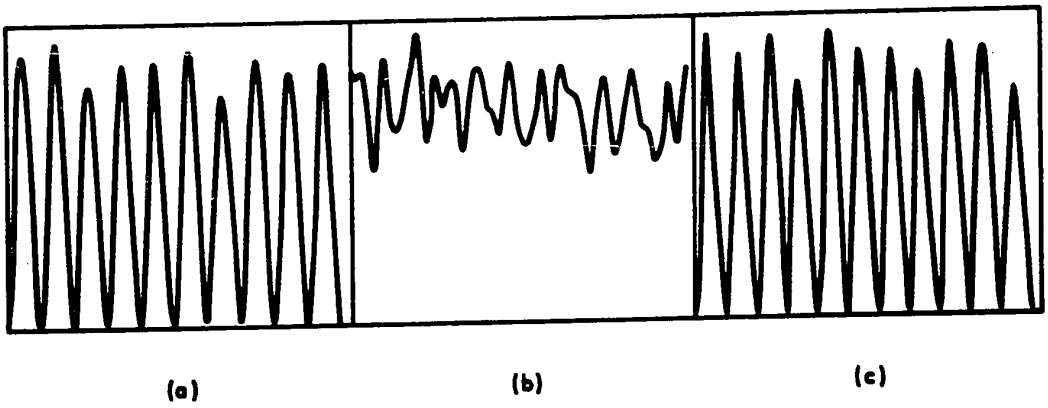

Fig. 30 Theoretical dark field profiles corresponding to the stacking fault in Fig. 29 at crystal thicknesses a) 10.0, b) 10.5, and c) 11.0 $\bar{\xi}^{\Delta}_{111}$.

that the images are symmetrical with respect to the centre of the fault and that no modulation in fringe contrast occurs with position of the fault in the crystal. Finally the fringe spacing was found to be equal to the effective extinction distance thus verifying that the fringes are in fact singlets and not doublets.

The theoretical results discussed above are in good agreement with the experimental contrast features described in section 7:4 and illustrated in Fig. 29. It should be noted that similar agreement was obtained for the range of crystal thicknesses up to $15\bar{\xi}^{\Delta}_{111}$, the maximum for which experimental results were obtained. Theoretical calculations indicated, however, that the characteristics of image contrast described above should persist to crystal thicknesses of twice this value (~3000 A°).

A final question arises as to whether or not the stacking fault contrast illustrated in Fig. 30 changes in character at values of $\Delta\theta_{111}$ greater than those for which experimental results were obtained. It was not possible to look into this question experimentally because the image intensity became too low to permit good micrographs to be presented. Theoretical calculations indicated, however, that all the contrast features mentioned remain essentially unchanged except that the

residual contrast shown in Fig. 30b became progressively weaker as $\Delta\theta_{111}$ increases, provided that none of the high order systematic reflections is too close to its Bragg condition.

7:6 ANALYSIS OF WEAK BEAM STACKING FAULT CONTRAST IN TERMS OF BLOCH WAVE INTERACTIONS

The method of approach in analysing image contrast is similar to that discussed in Chapters 5 and 6, and involves following the Bloch wave interactions from the top to the bottom surface of the faulted crystal. These interactions are followed in the usual way by calculating the contributions of the various Bloch waves to the diffracted beam amplitude at different positions in the crystal. The results of calculations carried out in the range of $\Delta\theta_{111}$ from 3.2 θ_{111} to 3.8 θ_{111} were all similar. These results are illustrated in Fig. 31 which shows the magnitudes of ϕ_g^i's and ϕ_g^{ij}'s obtained at $\Delta\theta_{111}$= 3.2 θ_{111}. Only interactions between Bloch waves 3 and 5 are given since all other Bloch wave interactions were quite small and could therefore be neglected.

It can be seen from Fig. 31 that at the top surface of the crystal, Bloch waves 3 and 5 are of approximately equal importance. The contributions of these Bloch waves to the diffracted beam amplitude

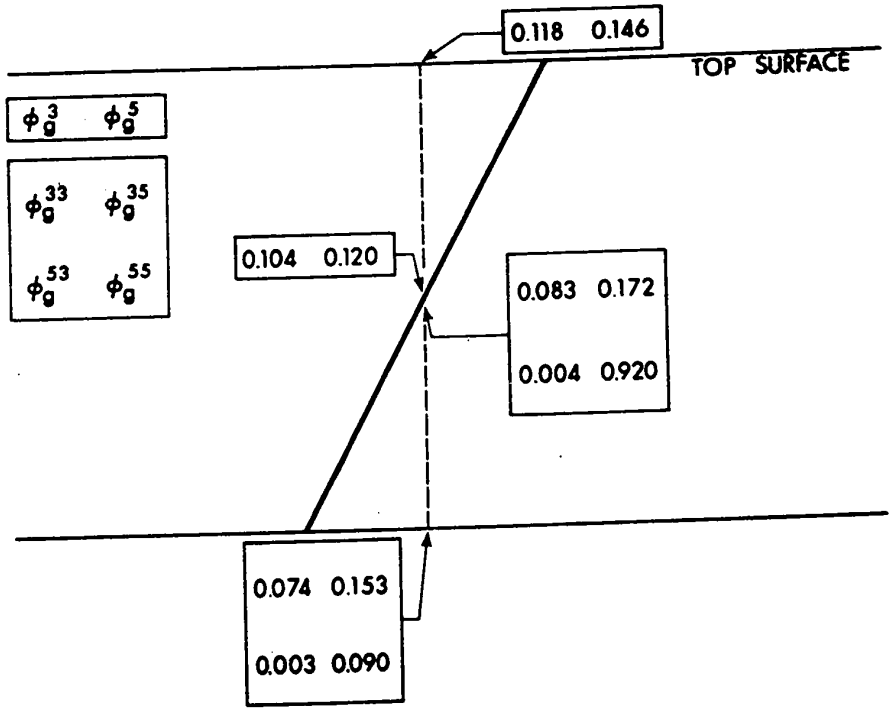

Fig. 31 The magnitudes of ϕ_g^i and ϕ_g^{ij} for an $\alpha = 2\pi/3$ fault at $\Delta\theta_{111} = 3.2\,\theta_{111}$. The accelerating voltage was taken to be 150 kV.

just above the fault will, to a good approximation, be equal and independent of the fault depth, since the absorption coefficients of both Bloch waves are nearly the same. As Bloch waves 3 and 5 encounter the fault, interbranch and intrabranch scattering occurs. It might at first be thought that interbranch transition from Bloch waves 3 to 5 (resulting in ϕ_g^{53}) and from 5 to 3 (resulting in ϕ_g^{35}) would be equally likely. The results in Fig. 31 show, however, that $\phi_g^{53} << \phi_g^{35}$, i.e. interbranch transitions from Bloch waves 3 to 5 are for all intents and purposes forbidden. The reason for this can be seen from equations 4.5 and 4.7, and the fact that $|C_o^3| << |C_c^5|$ and $|C_g^5| << |C_g^3|$. It can also be seen from Fig. 31 that just below the fault and at the bottom surface of the crystal the following relationships exist berween the interbranch and intrabranch components:

$$|\phi_g^{55}| \approx |\phi_g^{33}| \approx \frac{1}{2}|\phi_g^{35}| \quad .$$

In order to understand the thickness dependence of image contrast it is necessary to consider not only the magnitudes but also the phase relationships between the various ϕ_g^{ij}'s at the bottom surface of the crystal. These relationships can best be illustrated by phase amplitude diagrams such as the one in Fig. 32a which

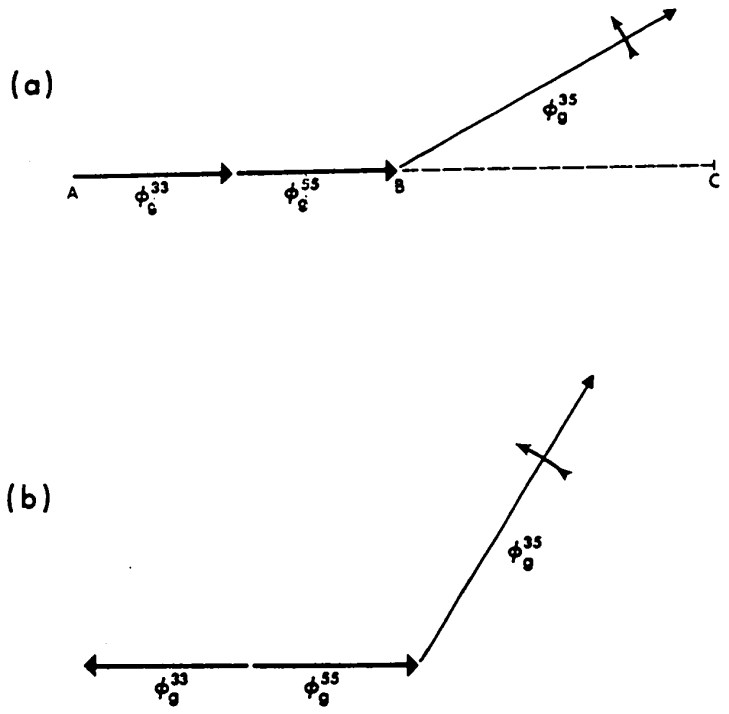

Fig. 32 Phase amplitude diagram showing the relationship between the contributions of interbranch and intrabranch scattering to the diffracted beam amplitude for an $\alpha = 2\pi/3$ stacking fault. The crystal thicknesses considered are:

a) $n\bar{\xi}^{\Delta}_{111}$, and

b) $(n+\frac{1}{2})\ \bar{\xi}^{\Delta}_{111}$.

shows the results obtained for a crystal thickness of $n\bar{\xi}^{\Delta}_{111}$, where n is an integer. The manner in which contrast arises can be understood by noting that, for a crystal of given thickness, contrast in images of stacking faults results from a change in fault depth t_1. Equations 4.5 and 4.7 show that the intrabranch components of the diffracted beam amplitude, ϕ_g^{ii}, are independent of t_1. The interbranch components ϕ_g^{ij}, on the other hand, will change with fault depth t_1 according to the term $\exp 2\pi i(\gamma^j - \gamma^i)t_1$. Thus as t_1 changes ϕ_g^{35} will rotate as indicated in Fig. 32a, making 1 complete cycle when t_1 changes by the effective extinction distance, $1/(\gamma^3-\gamma^5)$. Thus the diffracted beam amplitude varies from a maximum AC to zero to a maximum again when the stacking fault depth changes by one effective extinction distance. Singlets of strong contrast will therefore be obtained, in agreement with the experimental results in Fig. 29 and the theoretical profiles in Figs. 30a,c.

The phase amplitude diagram corresponding to a crystal thickness of about $(n+\frac{1}{2})\bar{\xi}^{\Delta}_{111}$ is shown in Fig. 32b. It can be seen that ϕ_g^{33} and ϕ_g^{55} are antiparallel, and there is therefore no intrabranch contribution to the diffracted beam amplitude. The total diffracted beam amplitude is therefore constant and equal to ϕ_g^{35},

with the result that no image contrast should be obtained. The fact that the theoretical profiles in Fig. 30b exhibit weak contrast is due to the small contribution of Bloch wave 1 to the diffracted beam amplitude which has been neglected.

Finally, it should be mentioned that calculations were carried out for values of $\Delta\theta_{111}$ in the ranges 4.2 θ_{111} to 4.8 θ_{111} and 5.2 θ_{111} to 5.8 θ_{111}. These calculations showed that the scattering mechanisms which give rise to contrast are essentially the same as those described above except that the Bloch waves involved were 4, 6 and 5, 7 respectively. In addition the contribution of Bloch wave 1 became smaller with increasing $\Delta\theta_{111}$ resulting in a further increase in the already weak contrast exhibited in Fig. 30b.

7:7 DEPENDENCE OF WEAK BEAM STACKING FAULT IMAGE ON ACCELERATING VOLTAGE

Observations of weak beam images of lattice defects are normally made at low accelerating voltages [110 to 113]. It is of interest, however, to explore the advantages, if any, of increasing electron energy. In order to investigate this point, weak beam stacking fault contrast was calculated at different accelerating voltages. All the values of $\Delta\theta_g$ used were high enough

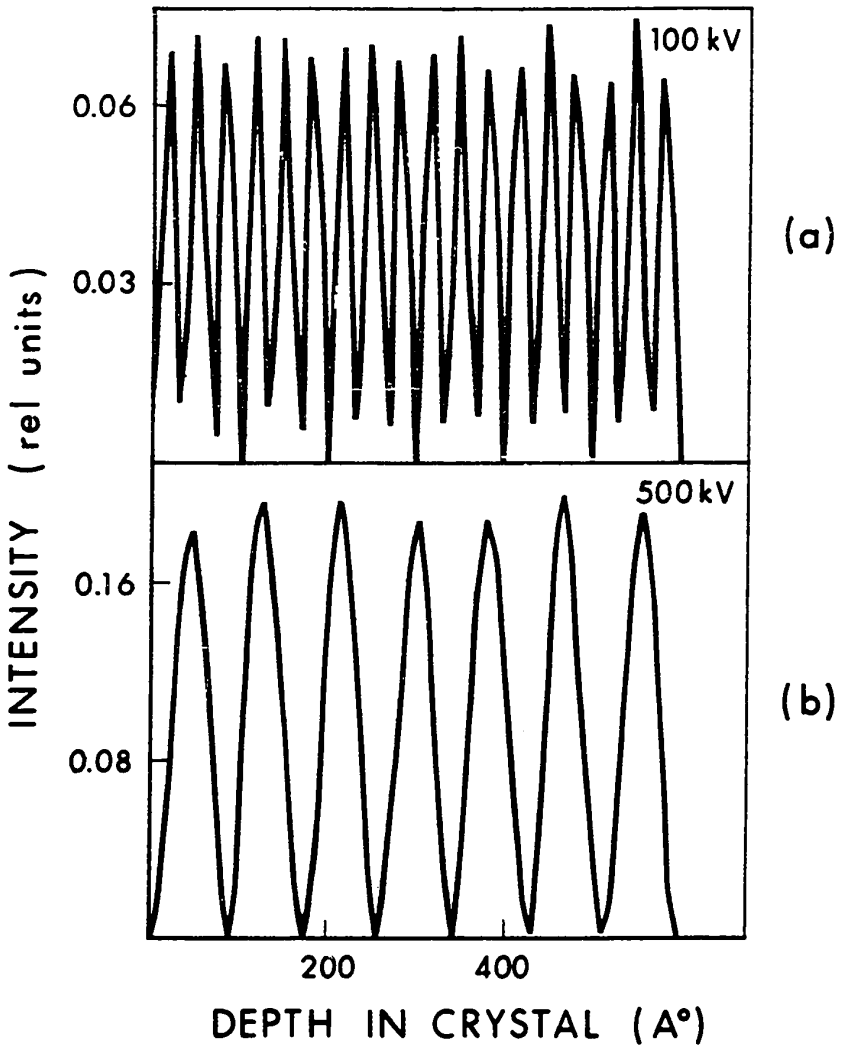

Fig. 33 Theoretical dark field profiles for an $\alpha = 2\pi/3$ stacking fault in fcc cobalt crystal calculated under weak beam diffraction conditions ($\Delta\theta_{111} = 6.2\ \theta_{111}$) for different accelerating voltages.

to insure that weak beam diffraction conditions at all electron energies were obtained. For the case of the (111) set of systematic reflections and in the range 100-500 kV, the values of $\Delta\theta_{111}$ used were greater than 6.2 θ_{111}, which corresponded to setting the crystal at an orientation outside the reflection (777) being in the Bragg condition. The results of these calculations indicated the following points:

(1) The nature of the image at all accelerating voltages was found to be quite similar to that described in section 7:4 for 150 kV.

(2) As accelerating voltage increased the effective extinction distance $\bar{\xi}_g^{\Delta} = 1/(\gamma^i - \gamma^{i+2})$ also increased. Thus for a crystal of given thickness the number of stacking fault fringes would decrease as the accelerating voltage is raised. (Compare the number of fringes in Figs. 33 a,b).

(3) At higher accelerating voltages the overall image intensity increased (compare Figs. 33 a,b). This would have the practical advantage of allowing weak beam images to be more conveniently observed at higher accelerating voltages.

7:8 SUMMARY, DISCUSSION AND CONCLUSIONS

The results presented in this chapter show that weak beam images of stacking faults arise due to the

interaction of two Bloch waves, i and j, where $j = i+2$ and $i \geq 3$. These Bloch waves are characterized by the fact that they have nearly equal absorption coefficients and that, above the fault, they make equally important contributions to the diffracted beam amplitude ($C_o^i C_g^i \approx C_o^j C_g^j$). Further it was found that $C_o^i << C_o^j$ and $C_g^j << C_g^i$ resulting in one of the possible interbranch transitions being essentially forbidden. The interbranch transitions which did occur resulted from the scattering of the Bloch wave with the highest value of excitation amplitude (C_o^j) to the one with the highest value of the Fourier coefficient (C_g^i). Similar interbranch transitions were reported by Cockayne [111] in his analysis of weak beam dislocation contrast.

It has also been shown that crystal thickness is an important factor in determining contrast in stacking fault images obtained under weak beam conditions. This was evidenced by the fact that when the crystal thickness was n extinction distances, strong fringe contrast was obtained. For crystal thicknesses of about $(n+\frac{1}{2})$ extinction distances, on the other hand, image contrast was found to be very weak. This result was found to be a consequence of the fact that the phase relationship between the two intrabranch components of the diffracted beam amplitude is a critical

factor in determining the nature of the contrast obtained. This phase relationship is determined by the value of the crystal thickness.

The fact that image contrast changes so dramatically with crystal thickness has important implications if stacking faults are to be observed under weak beam conditions. If the crystal thickness is $(n+\frac{1}{2})\bar{\xi}_g^{\Delta}$, then stacking faults will exhibit poor contrast and may therefore remain undetected. One possible error of interpretation which might arise under these circumstances is that of attributing a phase angle $\alpha = 2\pi\vec{g}.\vec{R} = 0$ to the fault. This difficulty can be avoided if the extinction distance can be changed to obtain the condition that crystal thickness is equal to $n\bar{\xi}_g^{\Delta}$. This can be achieved by simply tilting the crystal.

CHAPTER 8

ON MAXIMIZING STACKING FAULT CONTRAST IN THICK CRYSTALS AT HIGH ACCELERATING VOLTAGES

8:1 INTRODUCTION

Probably the greatest advantage of high voltage electron microscopes is that they enable the study of thicker specimens than is possible by using conventional low voltage instruments. In order to utilize this advantage fully it is important to choose the diffraction conditions which enable observations to be carried out in crystals which are as thick as possible. The results given in section 6:5 of Chapter 6 indicated that the maximum thickness of crystal in which observations can be carried out depends on both image intensity and image contrast.

At low accelerating voltages image intensity is maximized by choosing the strong beam diffraction conditions i.e. orienting the crystal so that a low order reflection is close to its exact Bragg condition. It has been found however [45,46] that in the vicinity of 1000 kV, maximum transmission normally occurs at the symmetry position of a low order systematic set. Thus there will be a low voltage range where strong beam images are

obtained near $\Delta\theta_g = 0$, and a high voltage range where those images are obtained at $\Delta\theta_g = -1.0\ \theta_g$.

The first question which arises is how would contrast in thick crystals, imaged under strong beam diffraction conditions, change as a result of increasing electron energy in the low voltage range. The work presented in section 8:2 of this chapter examines this question for both thickness fringe contrast and stacking fault contrast.

The next question is what contrast should be obtained in thick crystals when strong beam diffraction conditions in the high voltage range are used. The recent work of Humphreys et.al. [46] has shown that the reason for the high transmission obtained at the symmetry position, where Bloch waves 1 and 3 are strongly excited, is due to the channeling properties of Bloch wave 3. However, since Bloch waves 1 and 3 have widely different absorption coefficients, it would be expected that the nature of image contrast obtained at at these diffraction conditions would be characteristic of anomalous absorption. The effects of anomalous absorption when two Bloch waves of widely different absorption coefficients are excited was shown in Chapter 5 to give rise to a decrease in the visibility of the central fringe pattern corresponding to a stacking

fault in a thick crystal. On the other hand the results of Chapters 6 and 7 indicated that tilting the crystal away from orientations where effects of anomalous absorption are pronounced can result in significant contrast improvements. Thus the possibility arises that similar effects can occur by tilting the crystal away from the symmetry position at 1000 kV. The work presented in section 8:3 of this chapter explores these possibilities for the case of thickness fringe and stacking fault contrast.

8:2 DEPENDENCE OF IMAGE CONTRAST IN THICK CRYSTALS ON ACCELERATING VOLTAGE WHEN A LOW ORDER REFLECTION SATISFIES THE EXACT BRAGG CONDITION

Thickness fringe contrast obtained under strong beam diffraction conditions can be strongly influenced by the presence of systematic reflections(see section 5:1). However, in the case of cobalt this effect only occurs in thick crystals. This was evidenced by the fact that in thin parts of the crystal thickness fringes were two beam in character while in thick crystal thickness fringe contrast was multibeam in character (see section 5:1). The question which arises is in regard to the electron energy dependence of these contrast features. In order to examine this question, bright field profiles of thickness fringes were calculated at different

accelerating voltages. The range of accelerating voltages explored was from 50-500 kV. The calculations were carried out assuming the (111) set of systematic reflections to be excited in fcc cobalt with $\Delta\theta_{111} = 0$. The results are given in section 8:2.1. In section 8:2.2 the consequence of these results on stacking fault contrast in thick crystals are examined. Finally in section 8:2.3 an attempt is made to explain the results in terms of the changes which occur in the properties of the Bloch waves as electron energy is raised.

8:2.1 DEPENDENCE OF THICKNESS FRINGE CONTRAST AT $\Delta\theta_{111}=0$ ON ACCELERATING VOLTAGE

The manner in which the contrast of thickness fringes obtained in the bright field at $\Delta\theta_{111}=0$ changed with accelerating voltage can be seen by considering the multibeam profiles in Fig. 34. It can be seen from these profiles that the value of crystal thickness in which thickness fringes are two beam in character increases as the accelerating voltage is raised in the range 50-250 kV. That this is so can be seen by comparing Figs. 34 a,b and noting that at 50 kV the two beam fringes extend up to about 1000 A° while at 250 kV these fringes extend to about 2300 A°. The results in

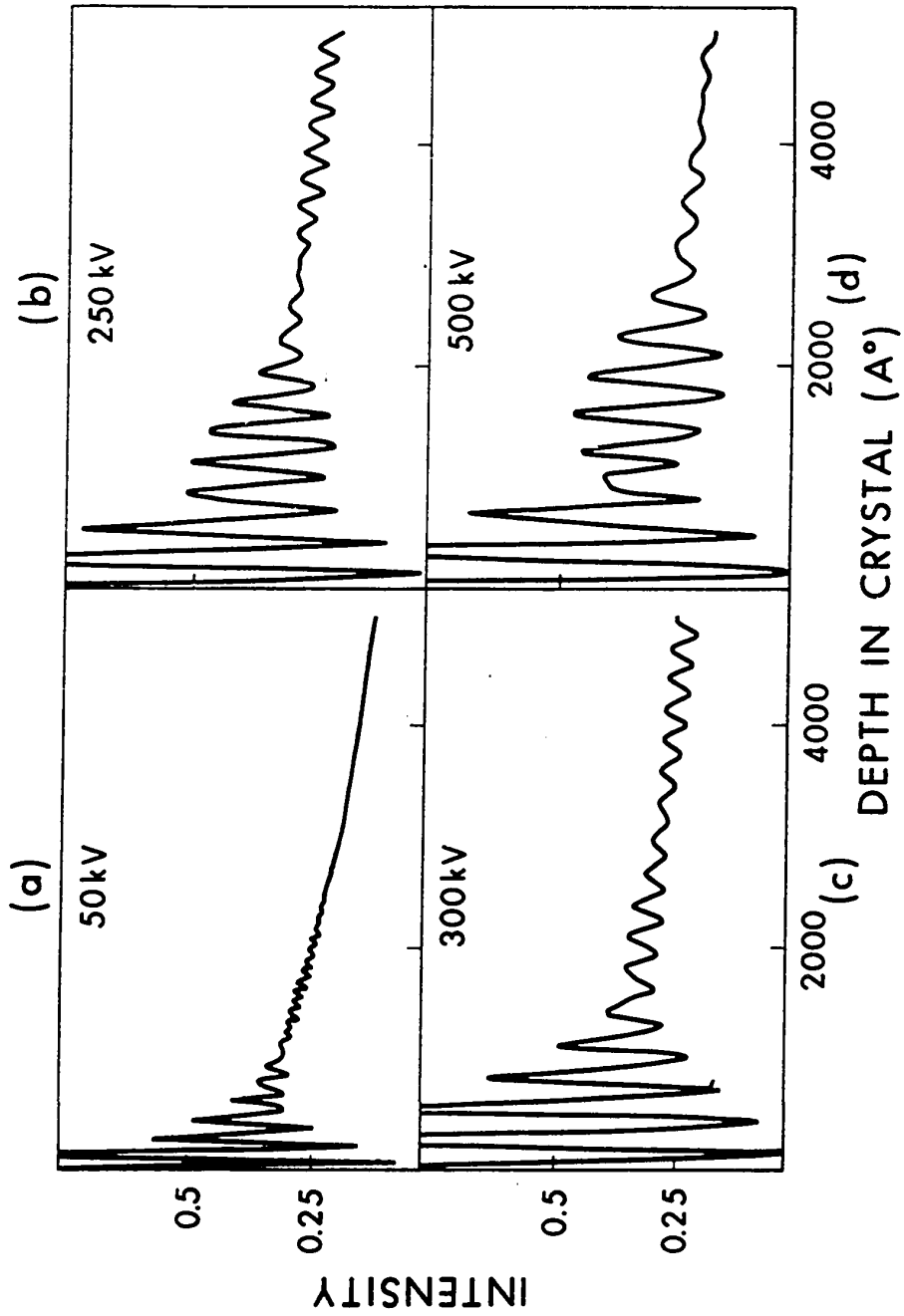

Fig. 34 Multibeam field thickness fringe profiles calculated for an fcc cobalt crystal at different accelerating voltages. The (111) set of systematic reflections was assumed excited and the 111 reflection was taken to be in the exact Bragg condition.

Figs. 34 c,d show, however, that at accelerating voltages higher than about 300 kV thickness fringes, even in thin parts of the crystal, exhibit the complex behaviour characteristic of multibeam effects.

The above results indicate therefore that in the range of about 50-250 kV raising electron energy results in an extension of the range of crystal thickness in which the two beam theory can be employed. These results are contrary to what was initially expected, namely that effects of systematic reflections increase by raising the accelerating voltage.

8:2.2 IMPLICATIONS OF RESULTS IN MAXIMIZING STACKING FAULT CONTRAST IN THICK CRYSTALS

The results presented in Chapter 5 indicated that at 150 kV the presence of systematic reflections has a deletarious effect on the contrast of stacking fault fringes obtained near the centre of a fault lying in a thick crystal. On the other hand, the results of the previous section indicate that increasing the electron energy from 50 to 250 kV, for the (111) systematic set in fcc cobalt, results in almost doubling the value of crystal thickness in which thickness fringe contrast can be described to be two beam in character. These results raise the possibility that stacking fault contrast

can be similarly enhanced in thicker crystals by increasing the accelerating voltage. In order to explore this possibility further, the dependence of stacking fault contrast in the bright field on crystal thickness was calculated at crystal thicknesses of n and (n+½) extinction distances at different accelerating voltages. These calculations were carried out in a similar manner to that described in Chapter 5. The results of these calculations showed that the differences between two and multibeam profiles decreased in thicker crystals as the electron energy was raised from 50 to 250 kV. These theoretical calculations indicate therefore that it is possible to decrease the deleterious effects of systematic reflections on the contrast of central fringes in a stacking fault image by raising the accelerating voltage in the range 50-250 kV.

It is important to mention that when an accelerating voltage higher than about 300 kV was considered in the calculation, stacking fault profiles obtained on the basis of two and multibeam theories were quite different. The multibeam dynamical theory predicted that the stacking fault image would be characterized by fringes which are complex in nature regardless of the value of crystal thickness considered.

8:2.3 EXPLANATION OF RESULTS

Insight into the physical reasons for obtaining the results described in the last two sections can be gained by examining the changes which occur in the values of the relevant Bloch wave parameters as accelerating voltage is raised. In Fig. 35a the contributions, ϕ_o^i, of Bloch waves 1 to 4 to the amplitude of directly transmitted beam at the top surface of the crystal are plotted as function of accelerating voltage. In these calculations the (111) set of systematic reflections in fcc cobalt was assumed excited with a value of $\Delta\theta_{111} = 0$. It can be seen from this figure that as electron energy is raised, the excitation of Bloch waves 1 and 2 decreases while that of Bloch waves 3 and 4 increases. If only these results were considered, the importance of higher order Bloch waves would be increased as accelerating voltage increases and consequently systematic reflections would have stronger effects at higher electron energies. It is important, however, to note that the situation will be quite different when the effects associated with changes in Bloch wave absorption coefficient are considered. It can be seen from Fig. 35b that in the range of accelerating voltages 50-250 kV, the value of the absorption coefficient of Bloch wave 1 decreases very rapidly compared to those of Bloch

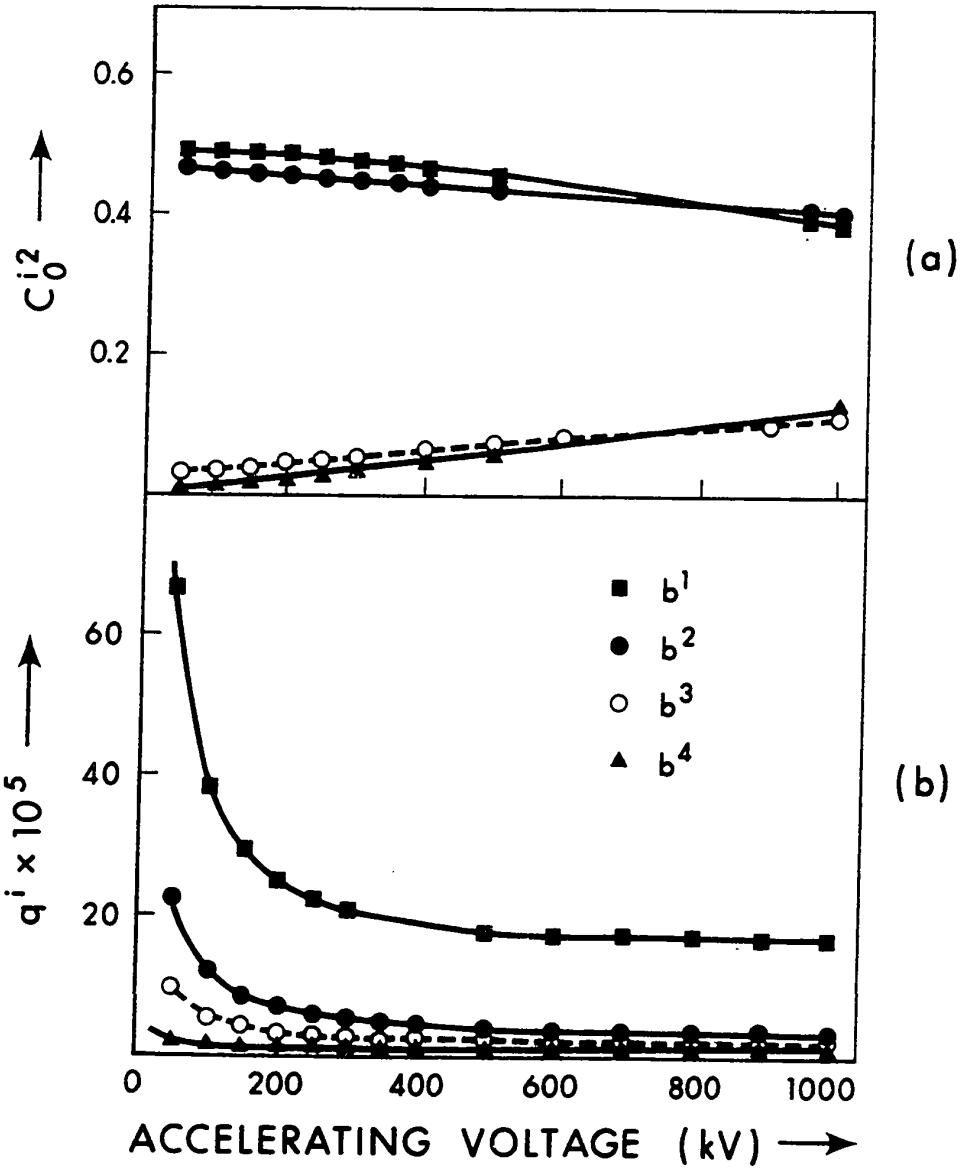

Fig. 35 a) The variation with accelerating voltage of the Bloch wave contributions to the amplitude of the directly transmitted beam at the top surface of the crystal.
b) The variation of Bloch wave absorption coefficients as a function of accelerating voltage.
In each case only Bloch waves 1 to 4 are considered and the crystal orientation assumed correspond to $\Delta\theta_{111} = 0$.

waves 2,3, and 4. Consequently the difference $(q^1 - q^2)$ of the two most important Bloch waves will decrease as the accelerating voltage is raised.

The results obtained in section 8:2.2 which indicated that two beam stacking fault contrast was obtained in thicker crystals by going from 50 kV to 250 kV can now be understood as follows. If electron energy is low (say 50 kV) then Bloch wave 1 has a very high value of absorption coefficient, and consequently its contribution ϕ_o^1 to the directly transmitted beam amplitude just above a fault near the middle of a thick crystal will be much less than ϕ_o^2 of Bloch wave 2. Very weak central fringe contrast results according to the mechanism discussed in section 5:3.2(a) of Chapter 5. On the other hand, as a higher accelerating voltage is employed, say 250 kV, the absorption coefficient of Bloch wave 1 decreases appreciably. The contribution ϕ_o^1 of Bloch wave 1 just above a fault lying near the middle of a thick crystal will not be small as the case discussed above. Image contrast in this case will to a good approximation arise from the interaction between the main Bloch waves 1 and 2. According to the mechanisms discussed in sections 5:3.1(a), (b) of Chapter 5, two beam contrast will therefore result. Central fringes will therefore be singlets of high contrast when crystal

thickness is (n+½) extinction distances, and doublets of lower contrast when crystal is n extinction distances thick.

At accelerating voltages above about 300 kV, Fig. 35b shows that the changes in Bloch wave absorption coefficients are small. Under the same conditions the excitation of Bloch waves 1 and 2 decreases while that of 3 and 4 increases. Raising the accelerating voltage in this energy range will therefore result in increasing the effects of multiple reflections, and image contrast becomes complex.

The analysis presented in this section shows that in deducing the changes in the role that systematic reflections have on stacking fault contrast as the accelerating voltage is raised it is important to take into account the changes in Bloch wave absorption coefficients and not only the changes in Bloch wave excitations.

8:3 ON THE DIFFRACTION CONDITIONS WHICH MAXIMIZE IMAGE CONTRAST IN THICK CRYSTALS AT 1000 kV

At 1000 kV, maximum electron transmission normally [45,46] occurs at the symmetry position of a low order systematic set. However, as noted in section 8:1, image contrast expected at this orientation would be characteristic of anomalous absorption. In order to

explore the diffraction conditions which maximize image contrast in thick crystals at 1000 kV, calculations of thickness fringe and stacking fault contrast were carried out at orientations in the range from the symmetry position $\Delta\theta_g = -1.0\ \theta_g$ up to the reflection g in the Bragg orientation $\Delta\theta_g = 0$. These results are presented in section 8:3.1. In section 8:3.2 an explanation of these results is given in terms of the scattering mechanisms which are responsible for producing image contrast.

8:3.1 RESULTS OF STACKING FAULT CONTRAST AND EXTINCTION CONTOURS AT HIGH ACCELERATING VOLTAGES

All the theoretical calculations presented in this section were performed for an fcc cobalt crystal. The (111) systematic set of reflections was considered and the reflections $\bar{5}\bar{5}\bar{5}$ ----- 555 were taken into account. Bright field images only were considered and the orientations investigated correspond to values of the deviation parameter in the range from $\Delta\theta_{111} = -1.0\ \theta_{111}$ to $\Delta\theta_{111} = 0.0$.

It is first of interest to consider the changes in thickness fringe contrast which occur as the crystal is tilted away from the symmetry position. The results in Figs. 36 a,b which show the intensity profiles

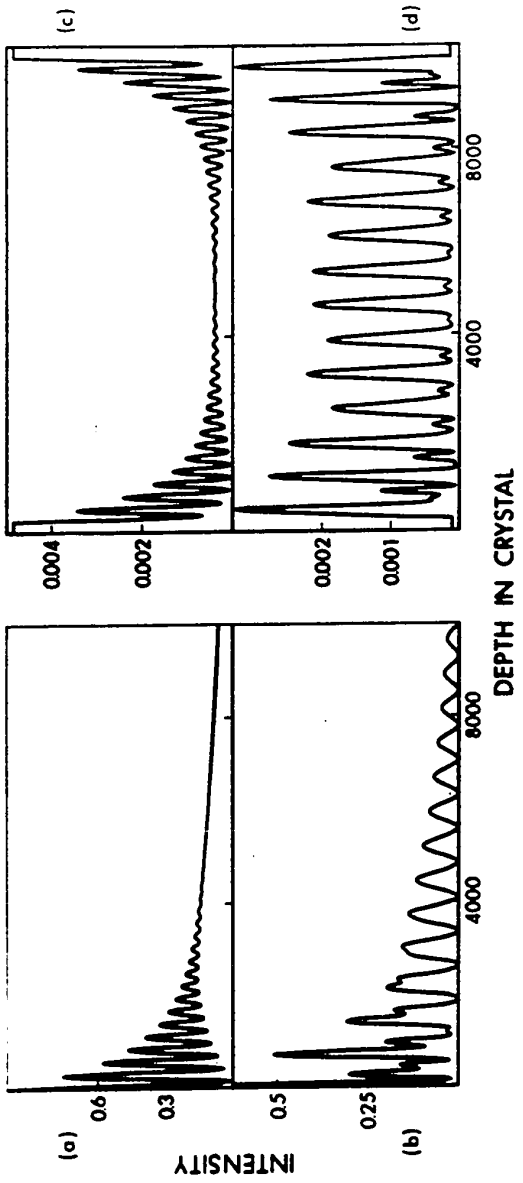

Fig. 36 Theoretical bright field intensity profiles for an fcc cobalt crystal at 1000 kV with the (111) set of systematic reflections excited. a) and b) extinction contour profiles obtained for values of $\Delta\theta_{111}$ equal to -1.0 θ_{111} and -0.2 θ_{111} respectively. c) and d) profiles for an $\alpha = -2\pi/3$ fault in a 1000 A° thick crystal at the same values of $\Delta\theta_{111}$.

obtained at values of $\Delta\theta_{111} = -1.0\ \theta_{111}$ and $-0.2\ \theta_{111}$, illustrate this change. It can be seen from Fig. 36a that at the symmetry position, thickness fringes in thick parts of the crystal exhibit poor contrast. On the other hand, the results in Fig. 36b show that when the crystal is tilted away from the symmetry position, thickness fringes in thick parts of the crystal exhibit very good contrast. These results can be understood by calculating the values of ϕ_o^i at the top surface of the crystal in the range of orientations considered. These results, shown in table 3, indicate that at the symmetry position thickness fringes result from the interaction of Bloch waves 1 and 3. Since these two Bloch waves have widely differing absorption coefficients, the thickness fringes would be expected to exhibit the poor contrast characteristic of anomalous absorption. At $\Delta\theta_{111} = -0.2\ \theta_{111}$, on the other hand, the important Bloch waves are 1, 2 and 3. Since $q^1 \gg q^2 \sim q^3$, thickness fringes in thick crystals result from the interaction of two Bloch waves of approximately the same absorption coefficient. The thickness fringes would therefore be expected to exhibit the good contrast characteristic of normal absorption.

It is next of interest to ask what stacking fault contrast is to be expected at these orientations. In order to answer this question, calculations of stacking

fault profiles have been carried out for an $\alpha = -2\pi/3$ fault in an fcc cobalt crystal of thickness equal to 1μ. The profile obtained at the symmetry orientation is shown in Fig. 36c and, as can be seen, the fringes near the centre of the fault exhibit weak contrast. This behaviour is characteristic of the two beam anomalous absorption profiles obtained at low accelerating voltages [14,15]. The profile at $\Delta\theta_{111} = -0.2$ θ_{111} is shown in Fig. 36d and, as can be seen, these fringes exhibit strong contrast in a crystal of the same thickness. It can also be noted from Fig. 36d that, except close to either surface of the crystal, the fringe spacing is equal to the effective extinction distance, $1/(\gamma^2 - \gamma^3)$ or about 900 A°.

Table 3

$\Delta\theta$	i= 1	i = 2	i = 3	i = 4
-1.0	0.49	0.00	0.51	0.00
-0.8	0.48	0.05	0.47	0.00
-0.6	0.47	0.14	0.39	0.00
-0.4	0.45	0.23	0.32	0.00
-0.2	0.43	0.31	0.27	0.00
0.0	0.39	0.38	0.11	0.11

8:3.2 ANALYSIS OF STACKING FAULT PROFILES IN TERMS OF INTERBRANCH AND INTRABRANCH SCATTERING

The results obtained in section 8:3.1 show that marked changes in the nature of stacking fault fringes near the centre of a fault occur when the crystal is tilted away from the symmetry position. The purpose of this section is to explain these results in terms of the scattering mechanisms which give rise to image contrast. These mechanisms can best be illustrated by following the Bloch wave interactions from the top to the bottom surface of the crystal. In order to follow these interactions at the two orientations of interest, calculations have been carried out of the values of ϕ_o^i at the top surface of the crystal and just above the fault and of values of ϕ_o^{ij} just below the fault and at the bottom surface of the crystal. The results which are shown in Fig. 37 only include interactions between Bloch waves 1, 2 and 3 since all other Bloch wave interactions were small and could be neglected.

The reason for the poor contrast exhibited by fringes near the centre of a fault in a crystal at the symmetry position can readily be seen by following the Bloch wave interactions in Fig. 37a. At the top surface of the crystal only Bloch waves 1 and 3 are important. Since $q^1 >> q^3$, Bloch wave 1 will be

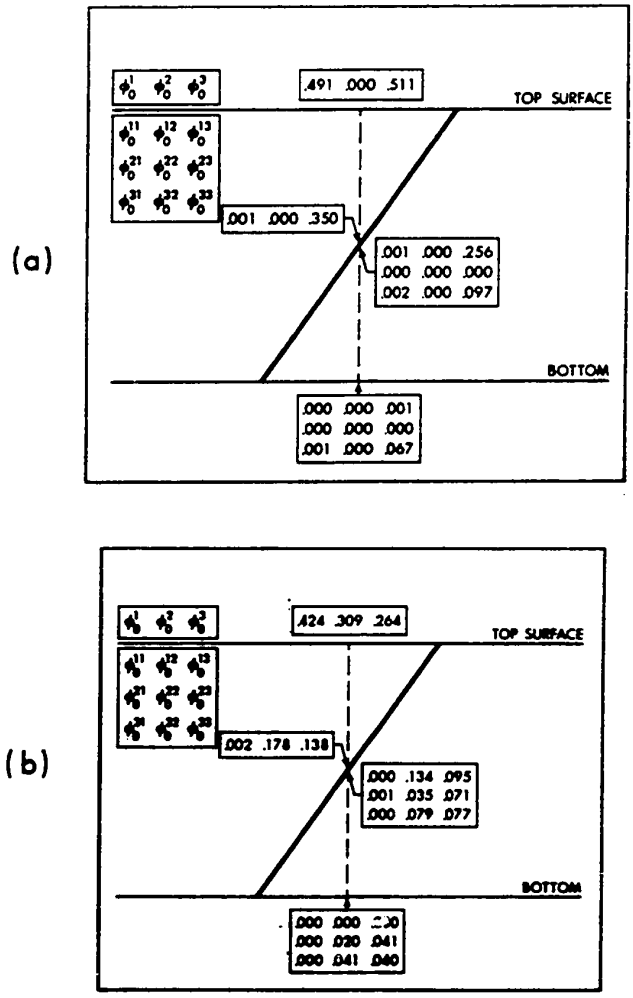

Fig. 37 The magnitudes of ϕ_o^i and ϕ_o^{ij} for an $\alpha = -2\pi/3$ stacking fault in an fcc cobalt at 1000 kV. It was assumed that the (111) set of systematic reflections was excited. a) and b) at values of $\Delta\theta_{111}$ equal to -1.0 θ_{111} and -0.2 θ_{111} respectively.

relatively weak in comparison with Bloch wave 3 just above the fault. As a result, the only significant interbranch scattering which can occur when the Bloch waves encounter the fault is from Bloch wave 3 to Bloch wave 1 (ϕ_o^{13}). Since q^1 is relatively high, this interbranch component of Bloch wave 1 will decrease rapidly with increasing distance from the fault with the result that it is negligible at the bottom surface of the crystal. The fringe contrast is therefore weak since a strong interbranch component is required in order to obtain good contrast.

The Bloch wave interactions which occur when the crystal is oriented so that $\Delta\theta_{11\bar{1}} = -0.2\theta_{111}$ can be seen from the values of ϕ_o^i and ϕ_o^{ij} in Fig. 37b. At the top surface of the crystal the three important Bloch waves excited are 1, 2 and 3. Since q^1 is relatively high, Bloch wave 1 will be weak in comparison with Bloch waves 2 and 3 just above the fault. As a result intrabranch scattering of Bloch wave 1 (ϕ_o^{11}) and interbranch scattering from Bloch wave 1 to Bloch waves 2 and 3 (ϕ_o^{21} and ϕ_o^{31}) will be weak while all the other interbranch and intrabranch components will be relatively high. Because of the high absorption coefficient of Bloch wave 1, the interbranch components ϕ_o^{12} and ϕ_o^{13} will weaken considerably before reaching the bottom surface of the crystal

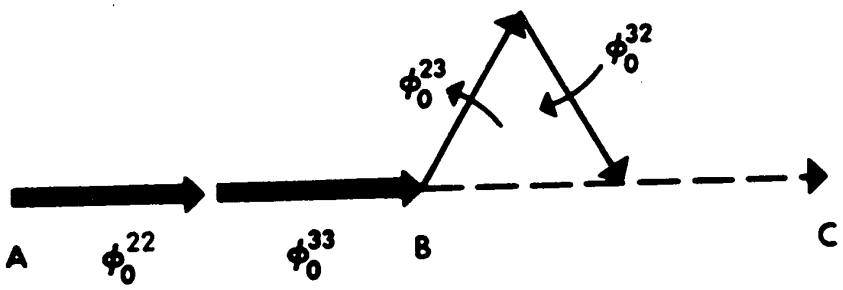

Fig. 38 Phase amplitude diagram showing the relation between the contributions of interbranch and intrabranch scattering to the amplitude of the directly transmitted beam for an $\alpha = -2\pi/3$ stacking fault at the centre of a 1000 A° thick crystal. The accelerating voltage was taken to be 1000 kV and $\Delta\theta_{111} = -0.2\ \theta_{111}$.

leaving only ϕ_o^{22}, ϕ_o^{33}, ϕ_o^{23} and ϕ_o^{32} with appreciable values. The reason that strong contrast is obtained follows directly from the fact that both Bloch waves 2 and 3 have strong interbranch components (ϕ_o^{23} and ϕ_o^{32}). In order to understand why fringe spacing is equal to the effective extinction distance $1/(\gamma^2 - \gamma^3)$, the phase relationships between the interbranch and intrabranch components must be considered. A schematic representation of these phase relationships is shown in Fig. 38. This diagram can be understood by recalling that the interbranch component ϕ_o^{ij} will vary with the fault depth t_1 according to the term $\exp 2\pi i(\gamma^j - \gamma^i)t_1$ (see equations 4.5 and 4.7). Thus at a value of t_1 equal to n extinction distances the two interbranch components ϕ_o^{23} and ϕ_o^{32} are in the same direction, giving a resultant amplitude equal to AC. As t_1 increases the vectors representing ϕ_o^{23} and ϕ_o^{32} rotate in the directions indicated with the result that when $t_1 = (n+\frac{1}{2})$ extinction distances the resultant amplitude is zero. When t_1 is equal to (n+1) extinction distances the resultant amplitude is a maximum again and equal to AC. Thus it can be seen that the amplitude of the directly transmitted beam varies from a maximum to a minimum to a maximum again if the stacking fault depth changes by one extinction distance.

It might be noted that the differences in detail between the fringe profile given by the above qualitative arguments and the fringes in Fig. 36d can be understood by carrying out a more detailed analysis.

8:4 DISCUSSION

Rocking Curves and Contrast

One of the primary objectives of the electron microscopist in carrying out observations of lattice defects is to choose diffraction conditions which give him high intensity, good contrast images. The crystal orientation which gives maximum transmitted intensity in the perfect crystal can be determined from rocking curves. These data, however, do not provide information on such questions as what diffraction conditions must be chosen in order to obtain optimum contrast or how contrast changes with crystal orientation and accelerating voltage. As has been noted the maximum bright field intensity at low accelerating voltages occurs when the low order reflection of a systematic set is in the Bragg condition. The results presented in Chapter 6 have shown that in the case of bright field images of stacking faults, a decrease in contrast occurs when the crystal is tilted away from this position. Thus at low accelerating voltages the diffraction

conditions for obtaining maximum bright field intensity and optimum contrast are the same [114]. The results presented in section 8:3 indicate that the situation at high accelerating voltages is quite different. The rocking curves obtained by Humphreys et.al. [46] at high accelerating voltages indicate that the bright field intensity in the perfect crystal decreases as the crystal is tilted away from the symmetry position (note, for example, the difference in background intensities in Figs. 36 c,d). Under the same circumstances, however, contrast in bright field images of stacking faults in thick crystals increases markedly. It is also important to note that although the intensity transmitted through the perfect crystal decreases appreciably as the crystal is tilted away from the symmetry position, intensity in the stacking fault image does not (compare, for example, the intensities at which fringe maxima occur in Figs. 36 c,d). These results therefore suggest that at high accelerating voltages the symmetry position may not be the best orientation to carry out observations of stacking faults in thick crystals.

8:5 SUMMARY AND CONCLUSIONS

The results obtained in this chapter have shown that:

(1) The effects of anomalous absorption on (111) strong beam images in fcc cobalt decrease as accelerating voltage is raised in the range 50-250 kV.

(2) As a consequence of this, the effect of systematic reflections in thick crystals, which is to reduce contrast, can be decreased. Thus raising the accelerating voltage in the range 50-250 kV can be beneficial in obtaining high image contrast in thick crystals.

(3) At high accelerating voltages,effects of anomalous absorption are most pronounced at the symmetry orientation with the result that stacking fault fringes near the centre of a fault lying in a thick crystal exhibit weak contrast. It has been shown that by tilting the crystal slightly away from the symmetry position strong contrast can be generated in images of thick crystals.

CHAPTER 9

GENERAL DISCUSSION AND CONCLUSIONS

9:1 BEAMS AND BLOCH WAVES

The first point to note in this section is the importance of describing electron images in terms of Bloch wave interactions. Most calculations of image contrast, based on the dynamical theory, are classified according to the number of beams taken into account, (see for example Humphreys et.al. [34] and Serneels and Gevers [98]). Thus, for example, a stacking fault profile would be referred to in the literature as being two beam or multibeam. The results presented in this thesis indicate that when discussing the nature of image contrast in terms of the dynamical theory, a more basic description is given in terms of the number of important Bloch waves excited and their characteristics. An example which serves to illustrate this point is the similarity between the familiar two beam stacking fault profiles obtained at low accelerating voltages for a thick crystal oriented so that a low order reflection is in the exact Bragg condition, and the multibeam profiles obtained at high accelerating voltages with the crystal oriented at the exact symmetry position (see section 8:3 of Chapter 8). The reason for

this similarity lies in the fact that in both cases the contrast arises from the interaction of two Bloch waves of widely different absorption coefficients. At low accelerating voltages these are Bloch waves 1 and 2 while at high accelerating voltages at the symmetry orientation Bloch waves 1 and 3 are important.

9:2 FACTORS DETERMINING THE APPLICABILITY OF THE TWO BEAM DYNAMICAL THEORY

The results presented in Chapters 5 to 8 of this thesis indicated that the applicability of the two beam theory in describing stacking fault contrast is determined by a number of interconnected factors. In this section a discussion of these factors is given.

1) Crystal thickness and defect depth

Crystal thickness and defect depth have not generally been assumed to be factors which determine the applicability of the two beam theory. The results in Chapter 5 have shown,however,that under certain circumstances both these factors can be important in deducing whether or not effects of systematic reflections are important. For example it was found, for the case of the (111) set of systematic reflections in fcc cobalt, that strong beam images of stacking faults in

thin or moderately thick crystals were two beam in character. For thick crystals however fringes near the centre of the fault were markedly affected by the presence of systematic reflections while edge fringes remained two beam in character. These results indicate that caution should be exercised in interpreting strong beam contrast of defects lying near the middle of thick crystals by using the two beam dynamical theory.

2) The order of the systematic set chosen

The results presented in Chapter 5 have also shown that by choosing a high order systematic set it was possible to reduce the deletarious effects of multiple reflections on strong beam contrast obtained from thick crystals. Thus the range of applicability of the two beam theory in describing strong beam images can be extended to thicker crystals by exciting a high order systematic set of reflections.

3) Material considered

Under strong beam diffraction conditions, thickness fringe and stacking fault contrast was found to be two beam in character when a moderately thick crystal of cobalt was considered (see Chapter 5). The calculations of Humphreys et.al. [34] indicated, on the other hand, that under similar diffraction conditions, stacking faults in gold are strongly influenced by the

presence of systematic reflections, even in relatively thin crystals. It is clear therefore that the atomic number of the material is an important factor in determining the strength of multibeam interactions. For low order systematic sets the two beam approach must therefore be restricted to thin and moderately thick crystals in materials of low and intermediate atomic number. For heavy elements however, it would be expected that the two beam theory would not be applicable except in extremely thin crystals.

4) Accelerating voltage

It has been commonly assumed [28,29] in the past that the applicability of the two beam theory decreases as the electron energy is raised. The results in section 8:2 have shown however that the two beam theory is applicable over a wider range of crystal thicknesses, provided that the accelerating voltage was raised in a certain range. These results indicate therefore that the assumptions made in the past with regard to the relationship between accelerating voltage and effects of systematic reflections does not hold unless the accelerating voltage exceeds a certain limit. For example for the case of the (111) set of systematic reflections in fcc cobalt this limit was found to be approximately 250 kV.

5) Crystal orientation

The crystal orientation for which the two beam theory has commonly been considered to be applicable corresponds to setting the crystal so that a low order reflection is sufficiently close to its Bragg condition. It would therefore be expected that when the crystal is tilted away from this orientation, the two beam theory becomes less applicable in predicting image contrast. Examples of this have been seen from the results of the present work in Chapters 6 and 7. For example dark field stacking fault contrast exhibited a marked departure from the two beam behaviour when the crystal was tilted near the Bragg orientation of the reflection 3g (see section 6:2).

9:3 STACKING FAULT CONTRAST IN TERMS OF BLOCH WAVE INTERACTIONS

The past several years have seen the development of a number of new techniques for studying lattice defects in transmission electron microscopy. The electron microscopist is confronted with the problem of choosing from these widely diverse techniques, the ones which will best suit his purposes. He first must decide,for example,what accelerating voltage to use.

He must also choose from such imaging techniques as the weak beam method [111,112,115], the use of critical voltage microscopy [116], or the conventional technique of imaging under strong beam diffraction conditions [15,117,118]. If he is interested in increased penetration he may want to use Bloch wave channeling to obtain increased intensity [45,46] or enhanced contrast in thick crystals [108,114].

In order to be able to choose from this wide range of possibilities, it is clearly desirable that the electron microscopist be guided by a basic understanding of the factors which influence diffraction contrast. Some understanding of these factors can be obtained by direct calculation of intensity profiles for different sets of conditions. However, a general understanding of image contrast can only be gained if such calculations are complimented by an investigation of the scattering mechanisms which give rise to image contrast. Investigations of this kind have been carried out in Chapters 5 to 8 of this thesis. The method used to gain an understanding of the scattering mechanisms responsible for image contrast was based on following the interaction between the important Bloch waves down through the faulted crystal. From these analyses it was observed that the general character of image contrast

obtained can be deduced from a knowledge of the number and characteristics of the Bloch waves excited at the top surface of the crystal. Examples of this behaviour are discussed in the next few sections.

9:3.1 ONE IMPORTANT BLOCH WAVE

When one Bloch wave only has an important contribution to the amplitude of the diffracted beam at the top surface of the crystal, very weak stacking fault contrast is expected. The reason for this, as noted in the analysis of section 6:4.1, is the absence of significant interbranch scattering which is essential in producing contrast.

The conditions under which one Bloch wave is important at the top surface of the crystal are:

(i) In the bright field at low accelerating voltages when $\Delta\theta_g > 1.0\ \theta_g$, provided that none of the high order reflections in the systematic set chosen satisfies their exact Bragg conditions.

9:3.2 TWO IMPORTANT BLOCH WAVES OF NEARLY EQUAL ABSORPTION COEFFICIENTS

The mechanism which gives rise to image contrast when two Bloch waves of equal absorption coefficients are important at the top surface of the crystal is quite similar to that discussed in section 8:3.2 for the central fringe pattern obtained at high accelating voltages when $\Delta\theta_g \sim -0.2\ \theta_g$. The stacking fault image for any fault depth will be characterized by nearly sinusoidal fringes exhibiting high contrast. Similar to the case discussed in section 7:6 for weak beam diffraction condition, stacking fault contrast would be expected to depend on crystal thickness variations within the effective extinction distance. However, since the absorption coefficients are nearly equal it would be also expected that there will be no variation in image contrast between thin and thick crystal. Good stacking fault penetration would therefore be expected.

Two Bloch waves of equal absorption coefficients can be excited at the top surface of the crystal under the following conditions:

(i) In the bright field when the reflections 2g, 3g, 4g, ... etc. are in the exact Bragg condition at low accelerating voltages.

(ii) In the dark field when weak beam diffraction conditions are chosen.

9:3.3 TWO IMPORTANT BLOCH WAVES OF WIDELY DIFFERING ABSORPTION COEFFICIENTS

The mechanisms producing contrast when the two important Bloch waves have widely different absorption coefficients have been discussed in detail in section 5:3. Fringe contrast was found to depend upon: a) crystal thickness, and b) defect depth.

For a moderately thick crystal central fringes are either doublets or singlets depending on the crystal thickness. When the thickness of the crystal is such that the resultants of inter- and intrabranch scattering are in phase, central fringes are singlets of high contrast (section 5:3.1(b)). When these resultants are at right angles a doublet structure occurs which exhibits weaker contrast (section 5:3.1(a)).

For an extremely thick crystal, central fringes have poor contrast irrespective of crystal thickness. The reason is that the interbranch contribution to the diffracted beam amplitude is much less than that of intrabranch contribution.

Edge fringes for any crystal thickness exhibit a singlet structure of high contrast. The reason, as noted in section 5:3.3, is that these fringes arise from inter- and intrabranch components which have nearly equal magnitudes.

Two Bloch waves of widely different absorption can be excited at the top surface of the crystal under the following conditions:

(i) At low accelerating voltages when the lowest order reflection in a systematic set is at the exact Bragg condition.

(ii) At high accelerating voltages near the symmetry position of a low order systematic set.

9:3.4 THREE IMPORTANT BLOCH WAVES: ONE IS HEAVILY ABSORBED

Analysis of image contrast when three Bloch waves are important, one of which is heavily absorbed, has been carried out in sections 6:4.2 and 8:3.2. For a thick crystal it was found that image contrast depends primarily upon defect depth. Fringes near the centre of the fault exhibit high contrast since they arise from the interaction of two Bloch waves of nearly equal absorption coefficients. On the other hand, near either of the crystal surfaces all the three Bloch waves have important contributions to the diffracted beam amplitude and a complex fringe pattern results.

The situations encountered in the present work where three Bloch waves are excited at the top surface of the crystal, one of which is heavily absorbed were:

(i) At low accelerating voltages in the dark field at orientations near the reflection 3g being in the Bragg condition.

(ii) At high accelerating voltages in the bright field when $\Delta\theta_g \sim -0.2\ \theta_g$, i.e. at orientations just inside the reflection g being in the Bragg condition.

9:4 SUGGESTIONS FOR FURTHER WORK

Stacking fault contrast has been analyzed in the present work by following the interactions between the important Bloch waves down through the faulted crystal. This method of analysis was seen to offer an understanding of the nature of image contrast in the presence of systematic reflections. The results given in section 9:3 have indicated that it should be possible to deduce the resulting image contrast if the number and the characteristics of the Bloch waves excited at the top surface of the crystal are known. In order to further explore this possibility more detailed analyses of stacking fault contrast under a wide variety of conditions are required. Such studies would be valuable in providing the electron microscopist with the diffraction conditions to be chosen in order to obtain optimum defect contrast.

Another important class of diffraction conditions which has not received much attention in the past is the case when non-systematic reflections are excited. Studying the nature of stacking fault contrast in the presence of non-systematics is a logical continuation of the work presented in this thesis. The objectives of this kind of study would be to answer important questions such as what mechanisms give rise to stacking fault contrast in the presence of non-systematic reflections, and what would be the advantages of exciting those reflections in imaging lattice defects.

The next point which is of considerable interest is the applicability of the column approximation of electron microscopy in calculating intensity profiles from sloping stacking faults. Whelan and Hirsch [12] suggested that if the two beam theory is employed to calculate stacking fault profiles it would be a good approximation to employ the column approximation provided that the angle of inclination of the fault does not exceed about 80° (see section 2:5.2). The results presented in this thesis have shown that for the fault inclinations used good agreement between experiment and the multibeam theory was obtained. However, the stacking faults investigated in the present work were in the majority of cases not steeply inclined to the surfaces of the crystal

(inclination angles were estimated to be in the range 45° - 60°). It would therefore be quite interesting to explore in future work the nature of contrast of more steeply inclined stacking faults and investigate whether or not image contrast can be accounted for by using the multibeam dynamical theory which employs the column approximation.

REFERENCES

[1] Heidenreich R.D., J. Appl. Phys. 20, 993 (1949).

[2] Hirsch P.B., Howie A., and Whelan M.J., Phil. Trans. A252, 499 (1960).

[3] Von Borries B., Ruska E., Naturwiss. 28, 366 (1940).

[4] Hillier J., Baker R.F., Phys. Rev. 61, 722 (1942).

[5] Heidenreich R.D., Phys. Rev. 62, 291 (1942).

[6] Boersch H., Zeit. f. Physik 121, 746 (1943).

[7] Kinder E., Naturwiss. 31, 149 (1943).

[8] Heidenreich R.D. and Sturkey L., J. Appl. Phys. 16, 97 (1945).

[9] Bethe H.A., Ann. Phys. LPZ, 87, 55 (1928).

[10] Frank F.C., Proc. Phys. Soc. (London) 62A, 202 (1949).

[11] Bollmann, W., Phys. Rev. 103, 1588 (1956).

[12] Whelan M.J., Hirsch P.B., Phil. Mag. 2, 1303 (1957).

[13] Whelan M.J., Hirsch P.B., Phil. Mag. 2, 1121 (1957).

[14] Hashimoto H., Howie A. and Whelan M.J., Phil. Mag. 5, 967 (1960).

[15] Hashimoto H., Howie A. and Whelan M.J., Proc. Roy. Soc. A269, 80 (1962).

[16] Drum C.M., Whelan M.J., Phil. Mag. 11, 205 (1965).

[17] Van Landuyt J., Gevers R. and Amelinckx S., phys. stat. sol. 7, 519 (1964).

[18] Amelinckx S., Modern diffraction and imaging techniques in material science (1970), Holland Publ. (Amsterdam-London).

[19] Gevers R., phys. stat. sol. 3, 1672 (1963).

[20] Gevers R., Art A. and Amelinckx S., phys. stat. sol. 3, 1563 (1963).

[21] Booker G.R., Ph.D. Thesis (1960), Cambridge University (unpublished).

[22] Booker G.R., Hazzeledine P.M., Phil. Mag. 15, 523 (1967).

[23] Head A.K., Aust. J. Phys. 20, 557 (1967).

[24] Humble P., Aust. J. Phys. 21, 325 (1968).

[25] Humble P., phys. stat. sol. 30, 183 (1968).

[26] Morton A.J., Clarebrough L.M., Aust. J. Phys. 22, 393 (1969).

[27] Sheinin S.S., 6th International Congress for Electron Microscopy 55 (1966), Kyoto.

[28] Goringe M.J., Howie A. and Whelan M.J., Phil. Mag. 14, 217 (1966).

[29] Howie A., Phil. Mag. 14, 223 (1966).

[30] Fukuhara A., J. Phys. Soc. of Japan 21, 2645 (1966).

[31] Goodman P., Lehmfuhl G., Acta Cryst. 22, 14 (1967).

[32] Hoerni J.A., Phys. Rev. 102, 1534 (1956).

[33] Fujimoto F., J. Phys. Soc. of Japan 15, 1022 (1960).

[34] Humphreys C.J., Howie A. and Booker G.R., Phil Mag. 15, 507 (1967).

[35] Gevers R., Van Landuyt J. and Amelinckx S., phys. stat. sol. 21, 393 (1967).

[36] Howie A., Whelan M.J., Proc. Roy. Soc. A267, 206 (1962).

[37] Silcock J.M., Tunstall W.J., Phil. Mag. 10, 361 (1964).

[38] Booker G.R., Tunstall, Phil. Mag. 13, 71 (1966).

[39] Wilson M.M., Radiation effects 1, 207 (1969).

[40] Rühle M., Wilkins M. and Essmann U., phys. stat. sol. 11, 819 (1965).

[41] Ashby M.F., Brown L.M., Phil. Mag. 8, 1083, 1649 (1963).

[42] Sheinin S.S., phys. stat. sol. 38, 675 (1970).

[43] Cockayne D.J.H., Ray I.F.L. and Whelan M.J., Phil. Mag. 20, 1265 (1969).

[44] Thomas G., Phil. Mag. 17, 1097 (1968).

[45] Humphreys C.J., Lally J.S., J. Appl. Phys. 41, 232 (1970).

[46] Humphreys C.J., Thomas L.E., Lally J.S. and Fisher R.M., Phil. Mag. 23, 87 (1971).

[47] Humphreys C.J., Proceedings of the 25th Anniversary Meeting of EMAG (Institute of Physics), 12 (1971).

[48] Humphreys C.J., Phil. Mag. 25, 1459 (1972).

[49] Dupouy G., Perrier F. and Durrieu L., J. Microscopic 9, 575 (1970).

[50] Berry M.V., J. Phys. C 4, 697 (1971).

[51] Mcgillavry C.H., Physica 7, 329 (1940).

[52] Kato N., J. Phys. Soc. Japan 7, 397 (1952).

[53] Sturkey L., Acta Cryst. 10, 858 (1957).

[54] Fujimoto F., J. Phys. Soc. Japan 14, 1558 (1959).

[55] Niehrs H., Z. Naturf. 14a, 504 (1959).

[56] Niehrs H., Z. Phys. 156, 446 (1959).

[57] Niehrs H., Proc. IVth Int. E.M. Conf. 1, 295 (1960) (Springer-Berlin).

[58] Fisher P.M., Jap. Jour. App. Phys. 7, 191 (1968).

[59] Howie A., Whelan M.J., Proc. Roy. Soc. A263, 217 (1961).

[60] Yoshioka H., J. Phys. Soc. Japan 12, 618 (1957).

[61] Yoshioka H. and Kianuma, J. Phys. Soc. Japan 17, 134 (1962).

[62] Whelan M.J., J. Appl. Phys. 36, 2099, 2103 (1965).

[63] Humphreys C.J., Hirsch P.B., Phil. Mag. 18, 115 (1968).

[64] Steeds J.W., Valdré U., Proc. Eur. Conference on Electron Microscopy, Rome, Vol. 1, p.43 (1968).

[65] Howie A., Valdré U., Proc. Third Eur. Conference on Electron Microscopy 1, Prague, 377 (1964).

[66] Pines D., Elementary excitation in solids (Benjamin, N.Y., 1963).

[67] Howie A., Proc. Roy. Soc. A271, 268 (1963).

[68] Kamiya Y., Uyeda R., J. Phys. Soc. Japan 16, 1361 (1961).

[69] Humphreys C.J., Whelan M.J., Phil. Mag. 20, 164 (1969).

[70] Howie A., Basinski Z.S., Phil. Mag. 17, 1039 (1968).

[71] Hirsch P.B., Howie A., Nicholson R.B., Pashley D.W. and Whelan M.J., Electron microscopy of thin crystals, Butterworth, London (1965).

[72] Fujiwara K., J. Phys. Soc. Japan 16, 2226 (1961).

[73] Fujiwara K., J. Phys. Soc. Japan 17, 118 (1962).

[74] Howie A., see discussion of paper by Fujiwara (1962).

[75] Hashimoto H., J. Appl. Phys. 35, 277 (1964).

[76] Dupouy G., Perrier F., Uyeda R., Ayroles R. and Mazel A., J. Microscopie 4, 429 (1965).

[77] Heidenreich S., Fundamentals of transmission electron microscopy (1964) (Interscience Publ.)

[78] Parthasarathy , Acta Cryst. 13, 802 (1960).

[79] Troiano A.R., Tokich J.L., Trans. Amer. Min (Metal) Engrso. 175, 728 (1948).

[80] Edwards O.S., Lipson H., J. Inst. Met. 69, 177 (1943).

[81] Troiano A.R., Tokich J.L., Metal Technol., April (1948), T.P. 2348.

[82] Botros K.Z., M. Sc. Thesis, University of Cairo (1965) (Unpublished).

[83] Ericksson T., Acta Met. 14, 853 (1966).

[84] Köster E.H., Thölen A.R. and Howie A., Phil. Mag. 10, 1093 (1964).

[85] Sheinin S.S., Rev. Sci. Instr. 37, 232 (1966).

[86] Grundy P.J., Phil. Mag. 12, 335 (1965).

[87] Grundy P.J., Tebble R.S., J. Appl. Phys. 35, 923 (1964).

[88] Ibers J.A., Acta Cryst. 11, 232 (1960).

[89] Vanshtein B.K., Ibers J.A., Kristallografia 3, 416 (1958).

[90] Ibers J.A., Vanshtein B.K., Kristallografia 4, 641 (1959).

[91] Smith G.H., Burge R.E., Acta Cryst. 15, 182 (1962).

[92] Doyle P.A., Turner P.S., Acta Cryst. A28, 390 (1968).

[93] Ralston A., Wilf H.S., Mathematical methods for digital computers, Ch. 7 (1962), John Wiley and Sons (N.Y.).

[94] Martin R.S., Reinsch C. and Wilkinson J.H., Numer. Math. 11(3), 181 (1968).

[95] Subroutine eigen is listed in the IBM scientific subroutine package.

[96] Humphreys C.J., Fisher R.M., Acta Cryst. A27, 42 (1971).

[97] Metherell A.J.F., Fisher R.M., phys. stat. sol. 32, 551 (1969).

[98] Serneels R., Gevers R., phys. stat. sol. 33, 703 (1969).

[99] Metherell A.J.F., Whelan M.J., Phil. Mag. 15, 735 (1967).

[100] Metherell A.J.F., Phil. Mag. 15, 763 (1969).

[101] Spring M.S., Steeds J.W., phys. stat. sol. 37, 303 (1970).

[102] Sheinin S.S., Botros K.Z. and Cann C.D., phys. stat. sol. (a)3, 537 (1970).

[103] Sheinin S.S., phys. stat. sol. 21, 247 (1967).

[104] Sheinin S.S., Cann C.D., phys. stat. sol. 28, 187 (1968).

[105] Cann C.D., Sheinin S.S., phys. stat. sol. 30, 791 (1968).

[106] Metherell A.J.F., Fisher R.M., phys. stat. sol. 32, 217 (1969).

[107] Botros K.Z., Sheinin S.S., Proc. 30th Ann. EMSA Meeting, 638 (1972).

[108] Sheinin S.S., Botros K.Z., J. Appl. Phys. 42, 1231 (1972).

[109] Art A., Gevers R., Amelinckx S., phys. stat. sol. 3, 697 (1963).

[110] Haussermann F., Proc. 7th Int. Conference Electron Microscopy, Grenoble, 2, 225 (1970).

[111] Cockayne D.J.H., Z. Naturforsch 27a, 452 (1972).

[112] Stobbs W.M., Sworn C.H., Phil. Mag. 24, 1365 (1971).

[113] Cockayne D.J.H., Jenkins M.L., Ray I.L.F., Phil. Mag. 24, 1383 (1971).

[114] Sheinin S.S., Botros K.Z., phys. stat. sol. (a)12, 549 (1972).

[115] Sheinin S.S., Botros K.Z., phys. stat. sol. (a)13, 585 (1972).

[116] Lally J.S., Humphreys C.J., Metherell A.J.F. and Fisher R.M., Phil. Mag. 25, 321 (1972).

[117] Sheinin S.S., Botros K.Z., phys. stat. sol. (a)8, 449 (1971).

[118] Sheinin S.S., Botros K.Z., phys. stat. sol. (a)3, 271 (1970).

END OF REEL

ARC-30